12-2016

Optimal Design of Process Parameters During Laser Direct Metal Deposition of Multi-Material Parts

Jingyuan Yan
Clemson University, jingyuy@g.clemson.edu

Recommended Citation

Yan, Jingyuan, "Optimal Design of Process Parameters During Laser Direct Metal Deposition of Multi-Material Parts" (2016). *All Dissertations*. 1813.
https://tigerprints.clemson.edu/all_dissertations/1813

OPTIMAL DESIGN OF PROCESS PARAMETERS DURING LASER DIRECT METAL DEPOSITION OF MULTI-MATERIAL PARTS

A Dissertation
Presented to
the Graduate School of
Clemson University

In Partial Fulfillment
of the Requirements for the Degree
Doctor of Philosophy
Mechanical Engineering

---

by
Jingyuan Yan
December 2016

Accepted by:
Dr. Georges Fadel, Committee Chair
Dr. Ilenia Battiato, Committee Co-Chair
Dr. Fadi Abu-Farha
Dr. Hongseok Choi
Dr. Xin Zhao

ABSTRACT

During the past few years, the need for multi-material parts or heterogeneous objects (HOs) has surfaced with the rapid growth of laser technology, material science and additive manufacturing techniques. Direct Metal Deposition (DMD) process, a metal based additive manufacturing technique, can locally deposit dissimilar metal powders to produce HOs as needed. While some theoretical and experimental studies have been conducted to investigate the DMD process, there are still some challenges such as the process parameters design, optimization, and adjustment during the fabrication of HOs that have not been well elucidated. This dissertation aims at developing the manufacturing science needed to design a laser additive manufacturing system capable of mixing two or more dissimilar powders to manufacture heterogeneous meta-materials objects. This research would enable moving beyond rapid "prototyping" into the realm of functional heterogeneous metal based additive manufacturing (HMAM).

Therefore, the objective of this research is to develop the science needed to support the design and manufacture of HOs, placing materials where needed, when needed, in the proportions specified by the design, and combining them in-situ to achieve significant performance enhancements. The dissertation starts by showing the whole picture of the design process, then identify where the challenges and improvement opportunities rest. The whole DMD system design includes the geometrical design of the powder delivering nozzles, the optimal design of the process parameters when depositing dissimilar materials, and the control or planning of the process parameters during the DMD fabrication of HOs. The Laser Engineered Net Shaping (LENS^{TM}) system developed at Sandia and commercialized by Optomec$^{®}$ Inc. is referred to and used to implement the research.

An Artificial Neural Network (ANN) based method is proposed using FEM (Finite Element Method) as simulation tool to find the optimal geometry of the injection nozzles in order to maximize the process efficiency. Then, a mathematical model-based design method is proposed combining a multi-objective optimization algorithm to optimize the process parameters including the injection angles, injection velocities, and injection nozzle diameters for the two materials, as well as the laser power and the scanning speed. Finally, a comprehensive study investigating the relationship between the desired part's composition and the process parameters is conducted to fabricate a part with precise composition compared to the heterogeneous components design information.

This dissertation provides a better understanding of the physical process in the DMD manufacturing of HOs. This work would help design the whole DMD system, and make it a more efficient, more precise and more flexible process.

DEDICATION

This dissertation is dedicated to my family for their love and support.

ACKNOWLEDGEMENTS

I wish to express my sincere thanks to my advisor, Professor Georges Fadel, for his careful guidance, excellent suggestions and constructive criticism. His help and encouragement are deeply appreciated.

I wish to also express my sincerely thanks to my co-advisor, Dr. Ilenia Battiato. Her guidance on fluid mechanics, modeling and simulation is really helpful to the fulfillment of my dissertation.

I would like to express my wholehearted gratitude to my other committee members, Dr. Xin Zhao, Dr. Hongseok Choi, and Dr. Fadi Abu-Farha for their constructive review of this work and their suggestions. Their advice greatly helped to improve this dissertation.

I would like to thank Dr. Richard Miller for his valuable suggestions on my research problem, and my friends and group members who helped and supported me during the past four years at Clemson: Changxue Xu, Qing Mao, Meng Xu, Ivan Mata, Anthony Garland, Nafiseh Masoudi, Mo Chen, Felipe Fernández, James Gibert, and Paolo Guarneri. Special thanks also go to my friends Yilong Zhou and Xiaoqing Cao who helped me on COMSOL learning, Wei Li who help me on laser related knowledge, Shuaishuai Liu who helped me on finite element analysis, and Longsheng Jiang and Sheng Fu who helped me on understanding process control. Without their help and

suggestions on my research study, the completion of this dissertation would be impossible.

I hereby take the opportunity to express my thanks to all the Clemson CEDAR group members in Department of Mechanical Engineering. It has been my great pleasure to work with them and to learn from each other. Their suggestions on my research work is very valuable. Their contributions to the team unity, activity organization, and developing a perfect learning and living environment is highly appreciated. I would like to thank all my other friends as well for providing companionship and laughter. Without them, I would have never been able to accomplish my work smoothly.

Last but far from least, I am grateful to all my family members for encouraging me and providing me a great learning environment. Particularly, I will be always indebted to my mother, Yanqiu Liu, and my father, Dexun Yan, for their love and unwavering support throughout my educational journey.

TABLE OF CONTENTS

Page

TITLE PAGE i

ABSTRACT ii

DEDICATION iv

ACKNOWLEDGEMENTS v

LIST OF TABLES x

LIST OF FIGURES xi

CHAPTER ONE INTRODUCTION 1

- 1.1 MOTIVATION AND BACKGROUND 1
- 1.2 METAL BASED MANUFACTURING OF HETEROGENEOUS MATERIALS 3
- 1.3 DMD PROCESS… 5
- 1.4 RESEARCH OBJECTIVES 9

CHAPTER TWO CURRENT RESEARCH STATE AND LITERATURE REVIEW 13

- 2.1 PROCESS MODELING OVERVIEW 13
  - 2.1.1 Powder Flow 13
  - 2.1.2 Laser Powder Interaction 20
  - 2.1.3 Laser Heating of Substrate 23
  - 2.1.4 Free Surface Evolution 26
- 2.2 DESIGN OF INJECTION NOZZLE 32
- 2.3 FGM PARTS FABRICATION BY DMD 37
  - 2.3.1 Deposition Materials 37
  - 2.3.2 Challenges in Quality of Parts 39
  - 2.3.3 Modeling the DMD of Multi-Material 41
- 2.4 SCOPE OF THE PRESENT STUDY 43

CHAPTER THREE DESIGN OF INJECTION NOZZLE IN DMD MANUFACTURING OF THIN-WALLED STRUCTURES 46

3.1 Introduction… 46
3.2 Modeling the Particle-Laden Gas Flow 48
  3.2.1 Modeling the Gas Turbulent Flow 52
  3.2.2 Modeling the Particle Dynamics 55
3.3 Design Procedure and Results 57
3.4 Discussion and Data Analysis 67
3.5 Conclusions and Future Work 75

CHAPTER FOUR A MATHEMATICAL MODEL-BASED OPTIMIZATION METHOD FOR DMD OF MULTI-MATERIALS 77

4.1 Introduction… 77
4.2 Model Formulation 79
  4.2.1 Particle Heating 81
  4.2.2 Material Mixing by Melt Pool Convection 84
  4.2.3 Laser Attenuation 88
  4.2.4 Substrate Heating 93
4.3 Optimization Methodology 96
4.4 Results and Discussion 104
4.5 Conclusions and Future Work 110

CHAPTER FIVE PROCESS PARAMETERS PLANNING DURING DMD OF FGM PARTS 113

5.1 Introduction… 113
5.2 2D Thin-Walled Structure Fabrication 116
  5.2.1 Model Based Design Methodology 116
  5.2.2 Case Studies 124
5.3 3D FGM Part Fabrication 143
  5.3.1 Model Based Design Methodology 144
  5.3.2 Case Study 158
5.4 Conclusions and Future Work 184

CHAPTER SIX CONCLUSIONS AND FUTURE WORK 186

6.1 CONCLUSIONS...... 186
  6.1.1 Design of Injection Nozzle 186
  6.1.2 Optimization of the Process Parameters in DMD of Multi-Materials 187
  6.1.3 Process Parameters Planning in DMD of FGM Parts 188
6.2 FUTURE WORK... 190
  6.2.1 Design of Injection Nozzle 190
  6.2.2 Optimization of the Process Parameters in DMD of Multi-Materials 191
  6.2.3 Process Parameters Planning during DMD of FGM Parts 191

REFERENCES 194

LIST OF TABLES

Table Page

3.1 Value ranges of design variables and their discrete values for testing. 58

3.2 Error of testing results for the neural network. 63

3.3 The injection nozzle shape designs..67

3.4 Summary for the parameters preference of the two objectives and the final designs...74

4.1 Critical process parameters and/or their possible ranges......................................97

4.2 Physical and thermal properties of Inconel 718 and Ti-6Al-4V...........................98

5.1 Physical and thermal properties of Inconel 718 and Ti-6Al-4V 124

5.2 Individual properties of Fe and Ni 161

5.3 Preset process parameters 163

5.4 Testing values of the critical process parameters..164

LIST OF FIGURES

Figure Page

1.1 Heterogeneous flywheel: a) representation, and b) cross sectional view of a fabricated heterogeneous flywheel made of 320 Stainless Steel and Copper Coated Nickel [Morvan2001]. 2

1.2 Schematic of the DMD process using two dissimilar materials (photo courtesy Optomec® Inc.) 7

1.3 The interactions among laser, powder, and the substrate 8

2.1 Typical calculation domain and boundary conditions for powder flow model, according to [Morville2012a] [Zekovic2007] 16

2.2 Powder distribution profile obtain by both simulation and experiment in the literature [Zekovic2007] [Wen2009] [Zhu2011] [Morville2012a] 18

2.3 Power concentration distribution in different regions [Tabernero2010] 18

2.4 Phenomena occur during deposition [Ibarra-Medina2011] 20

2.5 A numerical solution of laser heating on moving substrate [Shuja2010] 26

2.6 Free surface evolution simulation results based on (a) static model [Morville2012b], and (b) dynamic model [Cao2007] 30

2.7 Two different powder injection approach: (a) powder premixing [Shin2003], and (b) powder in situ mixing [Yakovlev2005] 33

2.8 Typical designs of injection nozzles (photo courtesy Reis lasertec and Fraunhofer ILT) 35

2.9 Typical internal geometry designs of injection nozzles 36

List of Figures (Continued)

Figure Page

2.10 The solid form of the LRF SS316/Rene88DT FGM [Lin2005] 39

2.11 Typical microstructure of LFRed K465 deposition: (a) morphology of LFRed deposition and (b) cracking characteristics in HAZ [Li2016] 41

3.1 A thin-walled structure built by DMD process with a 0.7 mm wall thickness (part manufactured at Optomec® Inc., Albuquerque, NM)............................... 51

3.2 Contact length between powder jet and substrate for different angles. The contact length is the shortest when the nozzle is perpendicular to the substrate 51

3.3 3D calculation domain for powder flow model with boundary conditions (B.C.) and mesh…..... 54

3.4 Simulation result for laser substrate heating at t = 1 s. Figure displays half of the solution domain due to symmetry (the symmetry plane is shown in the figure)... 57

3.5 Simulation results for a) gas flow without powder (cross-sectional view), and b) powder flow at 0.05 s 59

3.6 The expected values and the predicted values for the neural network validation: a) prediction of total number of particles on the substrate, and b) classification of particle catchment efficiency.. 64

3.7 Prediction results for all the rest 18360 designs: a) function output 1, b) function output 2 (taking sample numbers from 5000 to 10000 for a closer view), and c) the *M* values.. 65

3.8 Neural network prediction for powder catchment efficiency 71

List of Figures (Continued)

Figure Page

3.9 The sample data points showing the relationship between the slope angle and the powder catchment efficiency in percentage 72

4.1 The schematic of the modifiable coaxial DMD process 80

4.2 A typical simulation result for the clad formation and melt pool convection 88

4.3 The cross-sectional view of the working space 89

4.4 Illustration of the intersection line between the laser beam and the powder jet ... 92

4.5 Schematic for the substrate heating model 94

4.6 Illustration of a particle's longest traveling distance in laser beam 101

4.7 Graphical optimization flow chart in modeFRONTIER® 103

4.8 Scatter of the designed two objective functions 104

4.9 Design histories of the 8 design variables (pictures share the same legend as Fig. 4.9 (a))........ 106

5.1 Schematic of the DMD fabrication of a functionally graded part 114

5.2 Schematic illustration for 2D thin-walled part discretization and the dilution effect on mixing 118

5.3 Equating of the powder shadowing effect 122

5.4 Design process flowchart for 2D FGM part fabrication 123

5.5 FGM part with 1D composition variation... 125

List of Figures (Continued)

Figure Page

5.6 Typical simulation result (half space due to symmetry) for laser substrate heating. The innermost isotherm line represent the melt pool 128

5.7 First trial: (a) the volumetric feed rate of Inconel 718, (b) the volumetric feed rate of Ti-6Al-4V, and (c) the dilution rates at each location 131

5.8 Second trial: (a) the volumetric feed rate of Inconel 718, (b) the volumetric feed rate of Ti-6Al-4V, and (c) the dilution rates at each location 132

5.9 Third trial: a) the volumetric feed rate of Inconel 718, (b) the volumetric feed rate of Ti-6Al-4V, and (c) the dilution rates at each location 133

5.10 Final results: (a) the volumetric feed rate of Inconel 718, (b) the volumetric feed rate of Ti-6Al-4V, and (c) the dilution rates at each location 134

5.11 Final results using an alternative mixture rule: (a) The volumetric feed rate of Inconel 718, (b) the volumetric feed rate of Ti-6Al-4V, and (c) the dilution rates at each location 135

5.12 The volumetric feed rate of (a) Ti-6Al-4V and (b) Inconel 718; (c) the dilution rate for each layer, and (d) the dilution rate plot using an alternative mixture rule.. 138

5.13 Illustration of the desired FGM part with 2D concentration variation 140

5.14 The volumetric feed rate of (a) Ti-6Al-4V and (b) Inconel 718; (c) the dilution rates for each location, and (d) the dilution rates plot using an alternative mixture rule 142

5.15 Schematic illustration for part discretization and the dilution/overlapping effect on mixing 145

5.16 Schematic of the cross section of adjacent tracks 145

List of Figures (Continued)

Figure Page

5.17 Conversion process of the powder shadowing effect 148

5.18 Illustration for overlapping ratio determination...151

5.19 Design flowchart for 3D FGM parts...158

5.20 The objective FGM part with 3D concentration variation..............................159

5.21 Phase diagram of Fe-Ni system [Silman2012] 164

5.22 (a) Example calculation result (C = 1, P = 800W, V = 30mm/s at t = 0.4 s) illustrating the temperature distribution on half calculation domain, and (b) the evolution of the maximum temperature 166

5.23 Typical ANN testing results for prediction: (a) expected and predicted laser scanning speed, (b) laser scanning speed prediction error, (c) expected and predicted laser power, and (d) laser power prediction error 167

5.24 Regression analysis for ANN performance 171

5.25 Variation of total error with number of epochs when using ANN to predict the (a) laser scanning speed, and (b) laser power 172

5.26 The operating parameters at the 20th layer, 15th track when setting the laser power as constant (calculation resolution 0.001): (a) the required powder concentration comparing with the desired concentration; and (b) the required laser scanning speed..177

5.27 The operating parameters at the 20th layer, 15th track when setting the laser power as constant: (a) the required powder concentration comparing with the desired concentration (resolution 0.005); (b) the required laser scanning speed (resolution 0.005); and (c) the required powder concentration comparing with the desired concentration (resolution 0.01) 178

List of Figures (Continued)

Figure Page

5.28 The operating parameters at the 20th layer, 15th track when setting the laser scanning speed as constant (calculation resolution 0.001): (a) the required powder concentration comparing with the desired concentration; (b) the required attenuated laser power; and (c) the required initial laser power........181

5.29 The required powder concentration comparing with the desired concentration for the 15th track, 10th element, bottom to top. (a) The laser power is set as constant, and (b) the scanning speed is set as constant 171

CHAPTER ONE

INTRODUCTION

1.1 Motivation and Background

A heterogeneous object (HO) or component refers to an object with spatially different material compositions or structures [Kou2007]. Based on the material distribution, heterogeneous objects can also be classified into two categories: HCs (Heterogeneous Continuous) and HDs (Heterogeneous Discrete) [Kumar1997] [Huang2000a]. HCs have a continuous material distribution function while HDs have a discrete material distribution function. This dissertation focuses on the manufacturing of Heterogeneous Continuous (HC) objects since discrete boundaries can lead to high stresses and failures in engineering applications.

An HO has many advantages and in many cases can realize appearance and/or functionality that homogeneous objects cannot achieve. As such, HOs play an important role in different fields of application, especially in the aerospace and manufacturing industries. Some examples of HO include energy absorbing heterogeneous beams to maximize the load carrying capacity [Punch1995], heterogeneous cutting tools to increase the tool's life and quality [Xing1998], heterogeneous flywheels (Figure 1) to store higher amount of kinetic energy within the same dimensional bounds while satisfying stress constraints [Huang2000b], heterogeneous injection molds that enable fast and uniform part cooling [Huang2001], graded thermoelectrics and dielectrics, and piezoelectrically graded materials applied to broadband ultrasonic transducers [Müller2003], and functionally graded implants to increase both mechanical functionality and biocompatibility [Watari2004].

(a) (b)

Fig. 1.1 Heterogeneous flywheel: a) representation, and b) cross sectional view of a fabricated heterogeneous flywheel made of 320 Stainless Steel and Copper Coated Nickel [Morvan2001].

The object with continuous spatial material variation is also known as Functionally Graded Material (FGM), so in other words, this dissertation focuses on the manufacturing of functionally graded alloys, i.e. materials are locally optimized and deposited to address some functionality. This is for situations when the desired characteristics of two or more materials are required in different areas within an object and only heterogeneous structures can satisfy such requirements. The materials within a part exhibit usually smooth transitions to avoid concentrated mechanical stresses at the boundaries. The manufacture of a free form and truly locally tailored FGM part is the challenge we propose to address. Although manufacturing of HCs is the objective of this dissertation, the methods proposed in the dissertation are also applicable in manufacturing HDs.

1.2 Metal Based Manufacturing of Heterogeneous Materials

Additive Manufacturing (AM) allows part construction by material addition. The three-dimensional metallic components fabrication was first reported by Breinan and Kear via laser cladding in 1978 and subsequently a patent was issued to Brown et al. in 1982 according to [Qi2006a]. The 3D printing processes have shown the ability to blend multiple materials (typically 2) into a single part [Garland2015]. This is presently accomplished by an operator feeding materials on demand, normally in fixed proportions. Other processes based on powder metallurgy (PM) lay different metal powders in layers and, for instance, compress them together using a die-punch [Nemat-Alla2011] or sinter them with a laser [Traini2008] to forms heterogeneous components. However, because these PM processes are in general not flexible enough to vary components proportions along a line or at a specific point, they work on a plane by plane approach. Prinz and his co-authors [Fessler1997] [Binnard1999] have produced HO and functionally graded material parts with a variety of metallic powders using a modified shape deposition manufacturing (SDM) process. The researchers have mixed the powders in the feeding tube before depositing the mixture and melting it with a laser. To our knowledge, the SDM process cannot change materials per design requirements and cannot be controlled and wasn't optimized yet. Other current metal based additive manufacturing techniques include the Laser Direct Metal Deposition (LDMD) or Direct Metal Deposition (DMD), Ultrasonic Consolidation (UC), Shape Deposition Manufacturing (SDM), Selective Laser Sintering (SLS), and Electron Beam Melting (EBM), to name a few. The popular metal processing Solid Freeform Fabrication (SFF) or AM technologies have been well summarized by Jiang and Qi [Jiang2002] [Qi2006a]. Most of the above mentioned processes could conceivably vary materials, typically layer by layer, but only DMD and the like processes have the added flexibility to vary the material component per line and per point. DMD is able to deposit locally different metal powders onto a substrate to manufacture HOs according to user's commands and requirements at the microscale [Morvan2001] [Ensz2002] [Fadel2002] [Yakovlev2005] [Hofmann2014a]. In addition, DMD can also fabricate complex structures such as meso-structures with thin walls [Shankar2015] [Fazelpour2014] [Fazelpour2016]. The DMD process is similar to welding, but uses powders instead of wire. In addition, DMD allows the building of parts by material addition while welding is used to join parts. Therefore, DMD has superior versatility in variability of material spatial distribution, material selection, and component geometry when compared with other FGM processing techniques [Kieback2003]. In addition, parts made by DMD also have unique advantages, such as fine microstructures, small heat affected zone (HAZ), and superior material properties [Mazumder1999] [Mazumder2000] due to the inherently fast solidification rates. The rapid heating and cooling rates associated with DMD process enable the extended solid solubility in metastable or non-equilibrium phases, offering the possibility of creating new materials with advanced properties [Qi2006a].

1.3 DMD Process

Many names have been used to describe the DMD process depending on applications and patents. For example, the DMD AM technology originated from laser cladding, which is a coating and repairing technology, depositing one layer on an existing object, and terms such as “laser cladding” [Shepeleva2000] [Sexton2002] or “laser coating” [Otterloo1997] [Ranalli1996] were used. Then, the technology was demonstrated to be promising in the additive manufacturing of metallic and alloy parts. The process was originally named as Laser Engineered Net Shaping (LENS) developed in Sandia National Laboratories, and the name DMD was developed at the University of

Michigan in Ann Arbor and the University of Missouri at Rolla. Other names are used such as Direct Light Fabrication (DLF) used in Los Alamos National Laboratory, Laser Consolidation (LC) at the Canada National Research Council. These names are well summarized in the literature [Zhou2009] [Toyserkani2005].

The DMD process is an interdisciplinary technology which utilizes laser technology, robotics, process control, powder metallurgy, and computer aided design and manufacturing (CAD/CAM). The schematic of the process is shown in Fig. 1.2. The DMD uses a continuous wave or pulsed laser [Sun2004] [Toyserkani2004] to induce a melt pool on a substrate, and metallic powders are delivered into the pool via injection nozzles. The building object information is stored in the CAD model, then the model is sliced into layers to drive the building process. Inert gas, typically argon, is used as the delivering gas to prevent oxidation or chemical reaction between the melt pool and the surrounding air during the fabrication process. The layer forms as a result of the melt pool solidification, and the workpiece is gradually built up on the substrate in a layer by layer fashion. The materials can be also transferred to the substrate by wire feeding, but it was demonstrated that material delivery by powder is more efficient and more flexible [Kim2000a] [Kim2000b] [Syed2006a] [Syed2006b]. The part circled by a dashed rectangle in Fig. 1.2 is also named as the deposition head, which consists of the laser and nozzles. By moving the deposition head (or moving the substrate), the melt pool cools down quickly and solidifies, adding a thin layer formed by the deposition of powder particles where needed. A great variety of materials can be deposited on a substrate using this technique to form a deposition layer with thickness/height ranging from 0.05 to 2 mm, and width as narrow as 0.4 mm [Toyserkani2005], a collection of them forming a part.

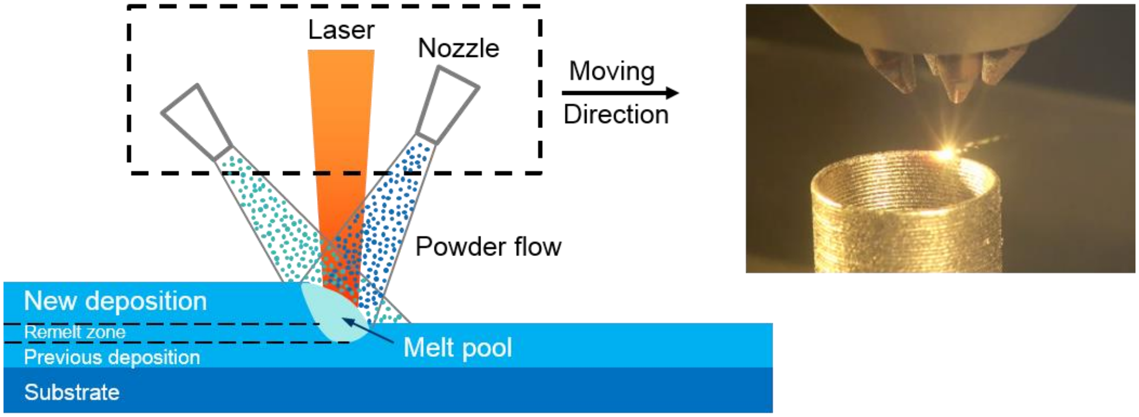

Fig. 1.2 Schematic of the DMD process using two dissimilar materials (photo courtesy Optomec® Inc.).

Numerous interactions exist in DMD, increasing the complexity of the process. The major interactions among laser, powder and substrate are shown in Fig. 1.3. The powder particles are heated by the laser beam during the flight. The particles that absorb laser energy are subject to phase changes from solid to liquid and/or gas. Simultaneously, the particle cloud has an attenuation effect or shadowing effect on the laser power, allowing a certain proportion of the laser energy to pass through. Then, the attenuated laser is reflected by the substrate, and only a portion of it is absorbed and used to heat the substrate, forming a melt pool. The melted and unmelted powder particles are deposited into the melt pool, adding mass to the substrate. Before the melt pool solidifies, the dissimilar powder particles are mixed inside the melt pool. The mixing effect is driven by the convection forces that exist in the melt pool.

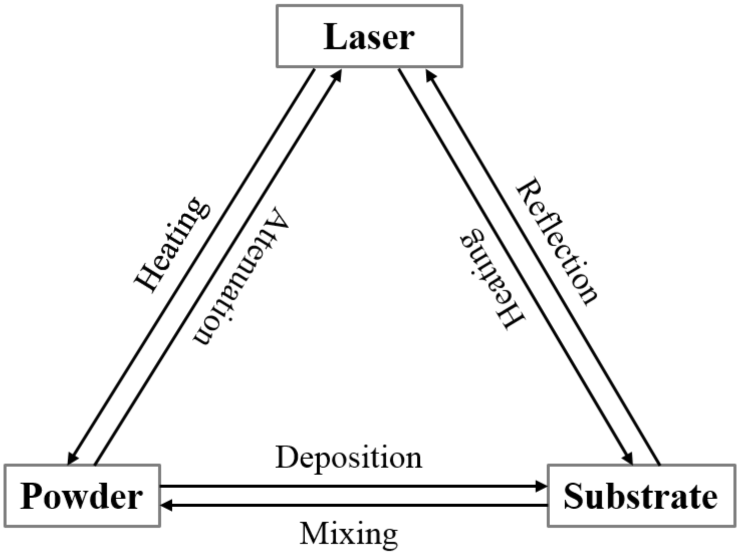

Fig 1.3 The interactions among laser, powder, and the substrate.

The DMD AM process offers a great number of advantages. The significant advantage is its ability to use materials (metals) that are desirable for end product production. The materials can also be deposited as needed, forming meta-materials or meta-structures. In addition, the fabricated parts are near net shape, but post-processing is required sometimes to obtain a better surface finish. Because of the fast heating and cooling process, the parts fabricated by DMD can also have good grain structures, which increases certain properties of parts.

1.4 Research Objectives

Despite all the benefits of DMD, this process is not yet widely used in industry, especially in AM applications. Several major issues remain unsolved that affect the quality of the final components: (1) due to the inherent characteristic, powder as building material, the mechanical strength of the fabricated part could be lower than that of a part fabricated by other processes such as forging or casting; (2) the fabricated parts usually have a rough surface, so post processing or polishing is required to obtain a better surface finish; (3) the variation of quality exists between layers or tracks or even within a deposition track, which is due to the high sensitivity of DMD to process parameters such as laser power, laser scanning speed, powder feed rate (affects surface evolution and laser attenuation); (4) the part must be cut from the sacrificial substrate; and (5) low composition accuracy when using dissimilar powders to fabricate FGM parts. Beside these major issues that affect the manufacturing quality, there are other issues such as the high equipment cost, limited powder utilization ratio, high energy/operational cost, and that the inclined angle of a wall is limited to a certain degree.

Therefore, it is the goal of this research to design the system process parameters, and to develop the science needed to produce unique, quality heterogeneous material components within a single structure directly from a CAD driven process.

The complexity of this process makes the interactions of the process parameters complicated. In order to understand the physical processes and the effects of process parameters in HOs fabrication, the objectives of this research include: (1) propose a design method that links the desired part’s composition to the manufacturing process parameters; (2) understand the powder particles flow and design the geometry of injection nozzles to be able to control the flight of particles and thus the usage of powders; (3) develop mathematical models to better understand the physics and constraints of the process; and (4) conduct off-line control and optimization of the process parameters in DMD of heterogeneous materials to find out the effects of different parameters on the process efficiency.

The organization of this dissertation is as follows:

In Chapter 1, the motivation and background of this work are introduced. The metal based additive manufacturing of heterogeneous objects is then reviewed, and the advantages of DMD are given, comparing them with other AM techniques. Then, an overview of the DMD process is presented as well as the basic physical phenomena in the process. Finally, the objectives of this dissertation are outlined.

In Chapter 2, the current research state is reviewed. The whole DMD process is broken down into consecutive physical processes. The review covers the modeling of the different physical processes in DMD firstly. The review then covers the design of injection nozzles. Next, the experimental and analytical studies on the DMD fabrication of FGM parts are reviewed. Finally, the scope of this dissertation is provided.

In Chapter 3, an injection nozzle design method is proposed based on 3D models. The design method is applied to the deposition of Ti-6Al-4V powder in building thin-walled structures, which is also applicable to solid parts. The design objective is to explore and find the designs of injection nozzle geometry that maximize the powder usage and minimize laser energy needs.

In Chapter 4, a pre-process computing is employed combined with a multi-objective optimization algorithm based on the modeling of DMD of multi-materials. The optimization method is then applied to the deposition of Inconel 718 and Ti-6Al-4V powders with prescribed powder feed rates. The multi-objective optimization considers that the laser energy consumption and the powder waste during the fabrication process should both be minimized.

In Chapter 5, a design method is proposed that links the process parameters to the desired part’s composition based on mathematical and numerical models. The proposed scheme is illustrated through case studies of both 2D (thin wall) and 3D structures. The materials used in the 2D case are Inconel 718 and Ti-6Al-4V, and the materials used in the 3D case are Fe and Ni.

In Chapter 6, conclusions and future work of this dissertation are summarized.

CHAPTER TWO

CURRENT RESEARCH STATE AND LITERATURE REVIEW

2.1 Process Modeling Overview

The DMD process can be studied by looking at the evolution of a single powder particle: from entering the injection nozzle to attaching to the substrate, becoming a part of the workpiece. A single particle experiences a series of physical processes after entering the nozzle: particle collision with nozzle inner wall and other particles (particle-solid interaction), particle flow in air (particle-gas interaction), particle heating by laser (particle-laser interaction), particle impingement into the melt pool (particle-liquid interaction), and liquid particle solidification (particle phase changes). The first three physical processes occur during the powder injection stage, while the last two occur in the powder deposition stage. The thermal and dynamic models of laser, powder and substrate can help to understand the process physics and better control the process efficiency and manufacturing quality. Therefore, in this section, the literature on modeling the different physical processes that exist in DMD is reviewed.

2.1.1 Powder Flow

In the DMD application for fabricating multi-material part, the parameters of multiple nozzles (typically four coaxial) for powder injection can be varied in respects of nozzles configuration, nozzle shape and injection angles. The parameters of dissimilar powders can also be different, such as the feed rate, injection speed, and material properties of powders. The modeling of powder flow is important to the whole process because it can directly affect the trajectories and phase changes of in-flight powder particles as well as the laser attenuation. In addition, knowing the powder particles' trajectories would help determine the usage of powder. The purpose of studying the powder flow is to investigate the powder particles distribution and temperature in the working space.

The dynamic behavior of powder flow has been investigated during the past couple of decades. Pinkerton developed a mathematical model for the powder concentration distribution [Pinkerton2004]. However, due to the complexity of the multiphase flow using coaxial nozzles, it is difficult to model the process analytically. In recent years, research concerning the powder flow has focused on the modeling of 3D multi-phase flow (the discrete particles phase in the continuous gas phase) using control-volume based computational fluid dynamics methods [Lin2000a] [Pan2006] [Zekovic2007] [Tabernero2010] [Ibarra-Medina2011] [Zhu2011] [Balu2012] [Morville2012a], and Wen et al. modeled this process in a cylindrical coordinate system using the same method [Wen2009]. In these publications, the particle collisions were not considered since the powder feed rate is low. The impact of nozzle dimension/angle, carrier/shielding gas flow rate, and particle properties, on the deposition efficiency were investigated, and these publications also demonstrate the importance of the nozzle-substrate distance as well as of the outer shielding gas in powder deposition/catchment efficiency [Pan2006] [Zekovic2007] [Balu2012]. Though laminar flow model has been adopted [Ibarra-Medina2011], a turbulent flow model is more realistic because of velocity fluctuation in all directions. Generally, the continuous phase is modeled using Reynolds-averaged-Navier-Stokes and the standard k-ε turbulence model. The Reynolds time-averaged equations for turbulent flow include conservation of mass, conservation of momentum, conservation of kinetic energy, and two transport equations regarding the kinetic energy and the dissipation of kinetic energy. The typical calculation domain and boundary conditions are shown in Fig. 2.1.

Conservation of mass:

$$\frac{\partial}{\partial x_j}\left(\rho u_j\right)=0 \tag{2.1}$$

Conservation of momentum:

$$\frac{\partial}{\partial x_j}\left(\rho u_i u_j\right)=-\frac{\partial p}{\partial x_i}+\frac{\partial \tau_{ij}}{\partial x_j}+\rho g_i \tag{2.2}$$

where $\tau_{ij}=\left[\left(\mu+\mu_t\right)\left(\frac{\partial u_i}{\partial x_j}+\frac{\partial u_j}{\partial x_i}\right)\right]-\frac{2}{3}\rho k\delta_{ij}$ and $\mu_t=\rho C_\mu \frac{k^2}{\varepsilon}$

Transport equation of kinetic energy:

$$\frac{\partial}{\partial x_i}(\rho u_i k) = \frac{\partial}{\partial x_i}\left[\left(\mu + \frac{\mu_t}{\sigma_k}\right)\frac{\partial k}{\partial x_i}\right] + p_k - \rho\varepsilon \tag{2.3}$$

Transport equation of dissipation of kinetic energy:

$$\frac{\partial}{\partial x_i}(\rho u_i k) = \frac{\partial}{\partial x_i}\left[\left(\mu + \frac{\mu_t}{\sigma_k}\right)\frac{\partial \varepsilon}{\partial x_i}\right] + C_{1\varepsilon}\frac{\varepsilon}{k}p_k - C_{2\varepsilon}\rho\frac{\varepsilon^2}{k} \tag{2.4}$$

where $p_k = \mu_t\left(\frac{\partial u_i}{\partial x_j} + \frac{\partial u_j}{\partial x_i}\right)\frac{\partial u_i}{\partial x_j}$

In the above equations, ρ is the density of the delivering gas, u is the gas velocity vector, p is the pressure, μ and μ_t denote the laminar and turbulent viscosities respectively, p_k is the volumetric production rate of turbulent kinetic energy by shear forces, k and ε are the turbulent kinetic energy and dissipation rate of turbulent kinetic energy, $C_{1\varepsilon}$ and $C_{2\varepsilon}$ are turbulent model constants.

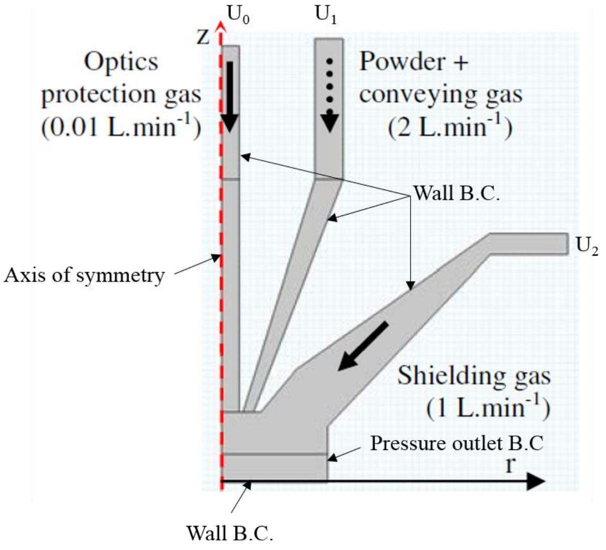

Fig. 2.1 Typical calculation domain and boundary conditions for powder flow model, according to [Morville2012a] [Zekovic2007].

The discrete phase is calculated by building a particle track model and solving particle kinematics equations, using the velocity information of the previously solved continuous gas phase. The trajectory of a dispersed phase particle is solved by integrating the force balance on each particle in a Lagrangian reference frame. The particle dynamics is driven by the gas flow drag and gravity. The force balance equates the particle inertia with the forces acting on the particle. The built-in force balance equation in FEM (Finite Element Method) software such as ABACUS, ANSYS, and COMSOL takes the form of the following equations.

$$\frac{du_{p,i}}{dt} = F_D\left(u_{g,i} - u_{p,i}\right) + \frac{g_i\left(\rho_p - \rho_g\right)}{\rho_p} + F_i \tag{2.5}$$

where $F_D = \frac{18\mu}{\rho_p D_p^2}\frac{C_D \,\mathrm{Re}}{24}$, $\mathrm{Re} = \frac{\rho_g D_p \left|u_{p,i} - u_{\mathrm{g},i}\right|}{\mu}$, $C_D = a_1 + \frac{a_2}{\mathrm{Re}} + \frac{a_3}{\mathrm{Re}^2}$, and $\frac{dx_i}{dt} = u_{p,i}$

In Eq. (2.5), u_p, D_p, and ρ_p are the velocity, diameter, and density of a particle; u_g and ρ_g are the velocity, and density of gas; F_i represent external forces acting on a particle; Re is the Reynolds Number, C_D is the drag coefficient; a_1, a_2, and a_3 are the empirical parameters for the relationship between drag coefficient and Re; and x_i is the position coordinates of a particle.

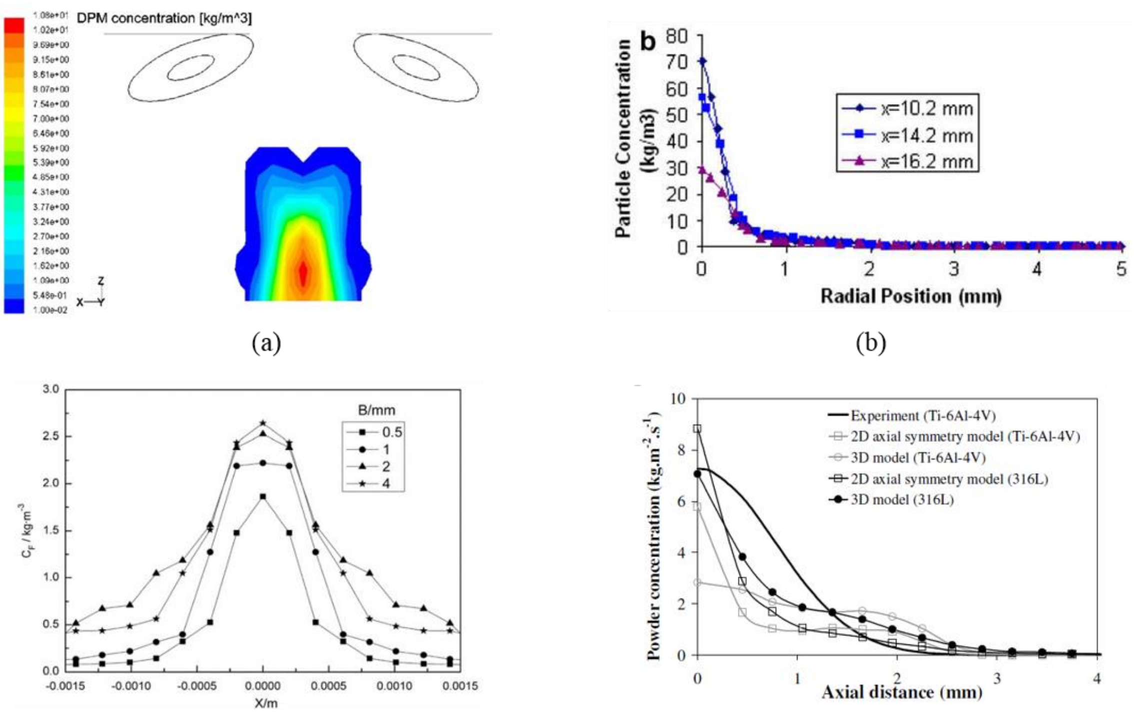

(a) (b)

(c) (d)

Fig. 2.2 Powder distribution profile obtain by both simulation and experiment in the literature [Zekovic2007] [Wen2009] [Zhu2011] [Morville2012a].

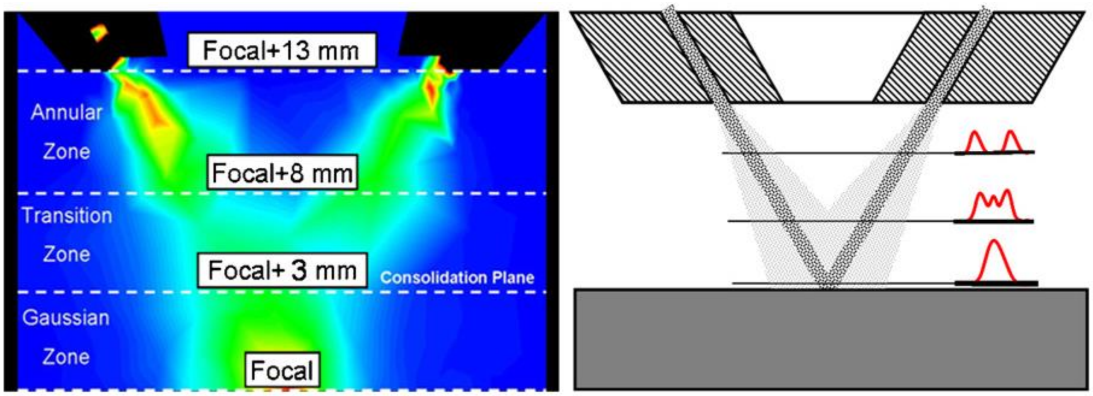

Fig. 2.3 Power concentration distribution in different regions [Tabernero2010].

The powder distribution is assumed to have a Gaussian profile in the literature [Lin1999a] [Pinkerton2004] [Zhu2011] [Balu2012] [Morville2012a]. Figure 2.2 shows some examples of Gaussian- powder distribution obtained by both simulation and experiment in literature. However, Tabernero et al. suggested that the powder flux distribution has Gaussian profile only when the substrate plane is within a certain height over the focal plane [Tabernero2010], as shown in Fig. 2.3. Yet, all the current models do not consider cases other than for a coaxial system and single type of powders. Unbalanced powder streams/jets may result in a powder concentration profile different from perfect Gaussian.

With respect to the powder distribution within a single powder stream/jet, Goodarzi et al. and Pinkerton approximated it as a perfect Gaussian distribution also, in order to develop an analytical model and explain the experimental results [Goodarzi2005] [Pinkerton2007]. Still, the current assumptions/approximations do not account for the effects of factors such as the shape of injection nozzles and the speed of feed gas.

In summary, the powder distribution should be analyzed according to different conditions, e.g., the configuration and shape/size of the injection nozzles, the speed of the delivering gas, and the distance between the nozzle tip and the substrate.

2.1.2 Laser Powder Interaction

Once the powder distribution is known, the temperature history of a single particle along its own trajectory should be determined. The interaction between laser and powder is considered prior to the laser heating of the substrate. Laser-powder interaction includes powder heating by laser, and laser attenuation due to powder flow. Figure 2.4 illustrates the phenomena that occur during deposition. A single particle is subject to direct irradiance by the laser beam, convection/radiation to the surroundings to release energy, and reflected irradiance by the substrate and other particles. The particles that remain in a solid phase are subject to a bounding effect by a solid substrate if injected outside the melt pool.

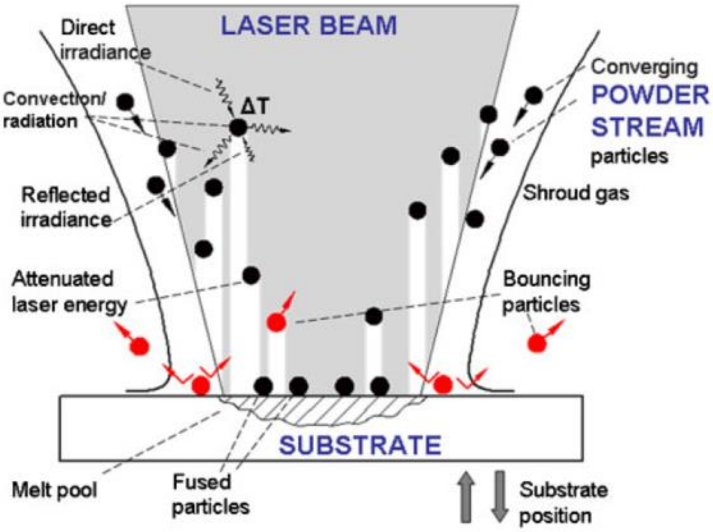

Fig. 2.4 Phenomena occur during deposition [Ibarra-Medina2011].

The powder temperature distribution at any point below the nozzle was calculated using analytical models that consider the particle velocity as well as the entire heating domain/work space [Jouvard1997] [Lin1999b] [Oliveira2005] [Pinkerton2007] [Giuliani2009]. These models provide a direct integration analytical solution for powder temperature. However, the analytical solutions are only limited to the specific system setups. The powder heating process has also been studied by looking at the heating, melting, and evaporation processes of a single spherical powder particle irradiated by laser beam; also, the single particle heating process is seen as heat transfer in a lumped system due to small Biot number [Grujicic2000] [Liu2003] [Han2004] [Huang2005] [He2007] [Wen2009] [Ibarra-Medina2011] [Morville2012a] [Yan2014]. When considering the single particle heating process, a number of researchers suggest to neglect the shading effect from other particles, i.e., the cloud of powder particles is considered sparse enough to be fully irradiated [Picasso1994] [Fu2002] [Liu2005] [Wen2009]. The energy balance of a single particle during laser heating is typically as follows (though some papers do not include the latent heat term):

$$m_p c_{pp} \frac{dT_p}{dt} = \eta_a I \frac{S_p}{4} - hS_p\left(T_p - T_\infty\right) - \varepsilon\sigma S_p\left(T_p^4 - T_\infty^4\right) - \delta L_f \frac{dm_p}{dt} \tag{2.6}$$

$$\text{where} \quad \delta = \begin{cases} 0 & T_p \le T_{sol} \text{ or } T_p \ge T_{liq} \\ 1 & T_{sol} < T_p < T_{liq} \end{cases}$$

In Eq. (2.6), m_p, c_{pp}, and S_p represent the mass, specific heat, and surface area of a particle respectively; T_p and T_∞ are the temperatures of the particle and the surroundings respectively; I is the laser intensity (W/m^2), and η_a is the laser absorptivity of the particle; ε is the surface emissivity of the particle; σ is the Stefan-Boltzmann constant (5.67×10^{-8} W/(m^2·K^4)); L_f is the latent heat of fusion of the particle materials; T_{sol} and T_{liq} are solidus and liquidus temperatures of the particle material respectively; and h is the convective heat transfer coefficient.

Eq. (2.6) gives the time evolution for the temperature of a single particle, which is effective and useful especially in numerical simulation. The effects of laser power, powder distribution, and particle properties such as particle size, initial velocity and in-flight distance on the heating process have also been studied in the literature mentioned above.

The heated particles transfer heat and add mass to the heated substrate. Before studying the laser heating of substrate, the attenuation of laser intensity due to powder flow should be considered. Picasso et al. developed the energy attenuation model in the laser cladding process [Picasso1994]. The model considers the ratio of the projected area of particles to the laser beam area, and the attenuation level is related to the particle properties such as density, radius, velocity, and injection angle. Lin et al. divides the 2D powder stream into three regions, where each region has a different theoretical expression for powder concentration and attenuation [Lin2000b]. Then, simplified models are proposed base on shadows while ignoring the effect of beam divergence and considering constant spherical particle shape [Fu2002] [Huang2005] [Liu2005]. In general, the Beer-Lambert law has been widely adopted to calculate the attenuation [Jouvard1997] [Lin2000b] [Han2004] [Pinkerton2007] [Zhou2009] [Tabernero2012]. The Beer-Lambert law generally takes the form:

$$I = I_0 e^{-\varepsilon C(z)z} = I_0 \exp\left(-\varepsilon \int_0^s C(z) dz\right) \tag{2.7}$$

where I is the attenuated laser intensity after passing through the powder cloud, I_0 is the original laser intensity, and s is the length of the section of the laser beam that traverses the powder cloud. The concentration term C(z) in Eq. (2.7) can be varied spatially and temporally, and the attenuation level depends on the exponential term. The attenuation calculation can take different forms due to different system configurations. In some research, the attenuation is calculated layer by layer [Qi2006b] [He2007]. However, in the literature, the attenuation level is calculated based on a coaxial axis configuration, and none of the current available models accounts for multi-materials and asymmetric power jetting.

2.1.3 Laser Heating of Substrate

The laser heating of the substrate can be abstracted to the problem of heat conduction due to a moving heat source. Researchers have developed analytical solutions using different models. Jaeger derived the analytical solution for a moving point heat source, band heat source, and rectangular heat source based on the assumption of a semi-infinite domain [Jaeger1942]. He considers the heating time $t = \infty$ for mathematical simplicity, and this limits the study to quasi-steady state only. He also introduces a dimensionless quantity $L = \frac{Vl}{2\alpha}$ to calculate the maximum and average temperatures over the area of the heat source. The general solution for heating by a moving rectangular laser is given as:

$$T_s = \frac{\eta I \alpha}{4(\pi\alpha)^{3/2} k_s} \int_0^T \frac{dt}{(T-t)^{3/2}} \int_{-b}^{b} dx' \int_{-b}^{b} dy' \exp\left[-\frac{\left[x - x' + V(T-t)\right]^2 + (y-y')^2 + z^2}{4\alpha(T-t)} \right] \quad (2.8)$$

where T_s is the substrate temperature; η is the heat source absorptivity by the substrate material; I is the heat source intensity; $\alpha = k_s / \left(\rho_s c_{ps}\right)$ is the thermal diffusivity of the substrate; k_s is the thermal conductivity of substrate; T is the travelling time of heat source from the beginning of heating; b is the rectangular laser spot width; x', y' are associated with the moving coordinate.

Numerous later publications present different analytical models in relevant fields, especially in tribology [Tian1994] [Bos1995] [Hou2000] and welding [Rosenthal1946] [Christensen1965] [Mackwood2005]. But studies on the various shapes of moving heat sources emerged only in the recent decades. For example, Tian et al. developed the approximated quasi-steady state solutions for moving circular, square, and elliptical heat sources of uniform and parabolic distributions profiles [Tian1994]. Hou et al. developed a general solution for plane heat sources of various shapes (elliptical, circular, rectangular, and square) with different heat intensity distributions (uniform, parabolic, and normal) [Hou2000]. Moreover, Akbari et al. provided a comprehensive review of the literature about studies on various shapes and intensity distributions of moving heat source, and presented a solution based on dimensionless numbers such as Péclet number (Pe) and Fourier number (Fo) [Akbari2011]:

$$\theta^* = \int_{-a^*}^{a^*} \int_{-\varepsilon_m a^* \left[1-(\chi/a^*)^n\right]^{1/n}}^{\varepsilon_m a^* \left[1-(\chi/a^*)^n\right]^{1/n}} \frac{e^{-Pe(X^*-\chi^*)}}{4\pi R^*}$$

$$\left[e^{PeR^*} erfc\left(\frac{R^*}{2\sqrt{Fo}} + Pe\sqrt{Fo} \right) + e^{-PeR^*} erfc\left(\frac{R^*}{2\sqrt{Fo}} - Pe\sqrt{Fo} \right) \right] d\gamma^* d\chi^* \tag{2.9}$$

Numerous studies have also been conducted using FEM to simulate the moving heat source problem [Shuja2010] [Anca2011] [Yilbas2013] [Marimuthu2013]. The problem practically can be a welding process, a friction process, or an AM process. The temperature or the residual stress of the substrate can also be found using commercial FEM software such as ABACUS, ANSYS, and COMSOL. The added mass can affect the dissipation of heat as well as the shape of the HAZ. Also, the heat brought to the melt pool by the heated powder particles should be considered. Before solidification, the shape of the melt pool evolves/changes as particles are injected into it. The consideration of the melt pool variation is reviewed in Section 2.1.4.

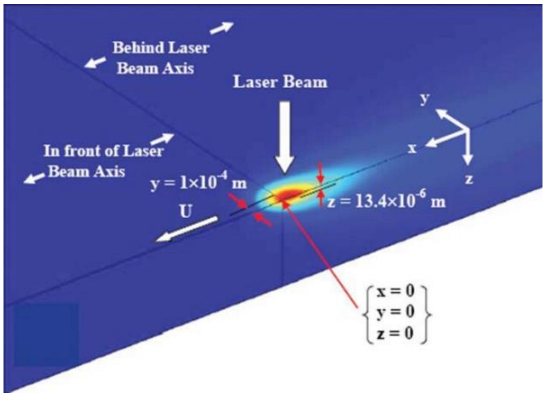

Fig. 2.5 A numerical solution of laser heating on moving substrate [Shuja2010].

2.1.4 Free Surface Evolution

The free surface of the melt pool evolves due to powder addition, impingement, heat transfer, and the relative movement between the laser and the substrate. This process is the most complex part of the study, which includes heat transfer and phase change, mass transfer, fluid flow in the melt pool (melt pool convection), melt pool cooling/solidification (clad formation), and dendrite growth and grain formation.

The clad profile/formation has been predicted by either static models such as in [Liu2005b] [Fathi2006] [Peyre2008] [Cheikh2012] [Morville2012b], or dynamic models such as in [Han2004] [Qi2006b] [Zhang2006] [Cao2007] [He2007] [Kong2010] [Wen2010], and both approaches show good agreement with experimental results. Specifically, in static models, the geometry of the clad profile is analytically predicted as a function of the process parameters, e.g., position, laser scanning speed, laser energy and powder flow distributions, powder feed rate, and density. In the dynamic models, the level-set method is used to track the liquid/gas interface and to simulate the continuous addition of material. Dynamic models are more sophisticated and have to solve the equations of conservation of mass, momentum, and energy in a coupled manner.

Level-set equation:

$$\frac{\partial \phi}{\partial t} + F\left|\nabla \phi\right| = 0 \tag{2.10}$$

or in a full form:

$$\frac{\partial\left(\rho\phi\right)}{\partial t} + \nabla\cdot\left(\rho\vec{V}\phi\right) = -\rho F_p\left|\nabla\phi\right| + \phi\frac{\partial\rho}{\partial H}\frac{\partial H}{\partial t} \tag{2.11}$$

where ϕ is the level-set function, F_p is the free surface growth velocity due to powder addition and fluid flow, H is the smooth approximation of the Heaviside function:

$$H_\varepsilon\left(\phi\right) = \begin{cases} 0 & \text{if } \phi < -\varepsilon \\ 0.5\left[1 + \dfrac{\phi}{\varepsilon} + \dfrac{1}{\pi}\sin\left(\dfrac{\pi\phi}{\varepsilon}\right)\right] & \text{if } \left|\phi\right| \le \varepsilon \\ 1 & \text{if } \phi > \varepsilon \end{cases} \tag{2.12}$$

where ε is half of the transition zone thickness, and the (mixture) physical properties such as density and viscosity in the whole calculation domain can be modified as:

$$\rho = \rho_{s,l} H_\varepsilon\left(\phi\right) + \left[1 - H_\varepsilon\left(\phi\right)\right]\rho \tag{2.13}$$

$$\mu = \mu_{s,l} H_\varepsilon\left(\phi\right) + \left[1 - H_\varepsilon\left(\phi\right)\right]\mu \tag{2.14}$$

where the subscript *s*, *l*, and *g* represent the solid, liquid, and gas phases respectively. The governing equations are typically given as follows.

Conservation of mass:

$$\frac{\partial \rho}{\partial t} + \nabla \cdot \left(\rho \vec{V} \right) = \frac{\partial \rho}{\partial H} \frac{\partial H}{\partial t} \tag{2.15}$$

Conservation of momentum:

$$\begin{aligned} \frac{\partial \left(\rho \vec{V} \right)}{\partial t} + \nabla \cdot \left(\rho \vec{V} \vec{V} \right) = \nabla \cdot \left(\mu_l \frac{\rho}{\rho_l} \nabla \vec{V} \right) - \nabla p - \frac{\mu_m}{\kappa} \vec{V} + \rho_r \vec{g} \beta_T \left(T - T_r \right) \\ - \left(\gamma \kappa \vec{n} - \nabla_s T \frac{\partial \gamma}{\partial T} \right) \frac{\partial H}{\partial \phi} + \frac{\partial \left(\rho \vec{V} \right)}{\partial H} \frac{\partial H}{\partial t} \end{aligned} \tag{2.16}$$

Conservation of energy:

$$\begin{aligned} \frac{\partial \left(\rho h \right)}{\partial t} + \nabla \cdot \left(\rho \vec{V} h \right) = \nabla \cdot \left(k \nabla T \right) - \nabla \cdot \left[\rho f_s \left(h_l - h_s \right) \vec{V} \right] + \\ \left[\eta I + q_p''' - h_c \left(T - T_\infty \right) - \sigma \varepsilon \left(T^4 - T_\infty^4 \right) \right] \frac{\partial H}{\partial \phi} + \frac{\partial \left(\rho h \right)}{\partial H} \frac{\partial H}{\partial t} \end{aligned} \tag{2.17}$$

The conservation of momentum equation accounts for the Darcy force $\frac{\mu_m}{\kappa} \vec{V}$ representing the damping effect when the fluid passes through the mushy region (mixture of solid and liquid phases), the buoyance force based on the Boussinesq's approximation $\rho_r \vec{g} \beta_T \left(T - T_r \right)$, the capillary force on the melt pool surface $\gamma \kappa \vec{n}$, and the Marangoni force on the melt pool surface $\nabla_s T \frac{\partial \gamma}{\partial T}$; and the last two terms are incorporated into the system with $\frac{\partial H}{\partial \phi}$ as boundary conditions. The conservation of energy equation accounts for the heat flux associated with relative phase motion between liquid and solid phases $\nabla \cdot \left[\rho f_s \left(h_l - h_s \right) \vec{V} \right]$, and the energy exchange at the melt pool surface due to laser absorption, convection, and radiation; and the last term is also incorporated into the system with $\frac{\partial H}{\partial \phi}$ as boundary conditions. For the bottom and side surfaces of the calculation domain, boundary conditions are given by the convective Cauchy boundary condition. The detailed explanation of the equations and solutions can be found in sources such as [Han2004] [Qi2006b] [Zhang2006] [He2007] [Wen2010] [Tan2011a] [Wen2011]. With the model, the evolution of the liquid/gas interface or the free surface movement can be tracked. The clad height and shape, melt pool peak temperature, melt pool width, dilution, temperature distribution, fluid velocity field, powder injection dynamics can be modeled. The clad shape and the quality of part have also been studied in the above mentioned literature with respect to process parameters such as the laser power, the powder feed rate, and the laser scanning speed. However, the free surface evolution based on asymmetric multi-material injection has not been studied, and the mixing effect of different powders inside the melt pool has drawn very few researchers' attention [Schneider1968] [Damborenea1994].

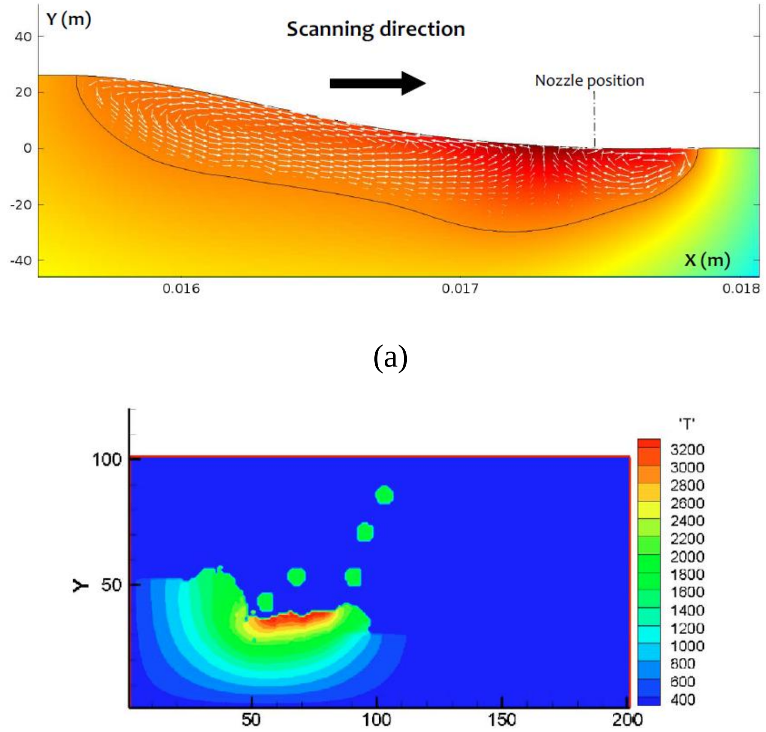

(b)

Fig. 2.6 Free surface evolution simulation results based on (a) static model [Morville2012b], and (b) dynamic model [Cao2007].

Furthermore, the microstructure and the quality of the fabricated part have been widely investigated, especially in the laser cladding/coating process. For example, Majumdar et al. carried out a detailed microstructural study of the surface and cross-section quality of the fabricated layer using optical and scanning electron microscopy to understand the effect of laser parameters, and found that the grain size decreases with the increase of scanning speed at a medium powder feed rate

[Majumdar2005]. Frenk et al. investigated the effect of cooling rate on the microstructure in laser cladding of cobalt-based alloy, and found that increasing the scanning speed leads to a considerable refinement of the microstructure as well as the decrease of secondary dendrite arm spacing [Frenk1993].

As for the dendrite growth modeling in the fields of welding and laser cladding, Yang et al. and Koseki et al. used the Monte Carlo model to predict the grain size and distribution in the melt pool and the heat affect zone [Yang2000a] [Koseki2003]. Pavlyk et al., Zhan et al., and Yin et al. simulated the dendrite morphology using cellular automata and phase field models [Pavlyk2004] [Zhan2009] [Yin2010]. Cao et al., Böttger et al., and Farzadi et al. applied the phase field model to obtain the quantitative predictions of dendrite morphology [Cao2007], and Cao et al. found that the dendrite tip that grows in the same direction with the heat flux has a higher velocity than a tip that grows in the opposite direction [Cao2007]. The effect of undercooling is also studied in [Cao2007], but the study was based on pure metal and some critical assumptions. Later on, Tan et al. simulated the microscale dendritic growth using the so called CAPF (Cellular Automata-Phase Field) model and compared with experimental results [Tan2011b].

The real 3D microstructure modeling is complex and has computational restrictions; the dendrite growth and grain formation modeling will not be the focus of this research. However, since the mechanical properties of parts are related to the grain size, the emphasis of the research should be placed on the quantitative relationship between the primary dendrite arm spacing (PDAS) or secondary dendrite arm spacing (SDAS) and the cooling rate. The relationship is shown in literature such as [Frenk1993] [Patel2001] [Easton2011] [Zhang2009] [Franke2010] [Tan2011a]:

$$DAS = C\dot{T}^{-1/} \tag{2.18}$$

where C is a constant, and the grain size and microstructure are related with the mechanical properties (hardness, strength, plasticity, toughness) of the fabricated parts.

2.2 Design of Injection Nozzle

In DMD of multi-materials, the dissimilar powder particles are delivered into the melt pool via two fashions typically: powder premixing [Schwendner2001] [Collins2003] [Domack2005] [Zhong2006] [Yue2008] [Hofmann2014] (Fig. 2.7 (a)), and powder in situ mixing [Lewis2000] [Liu2003] [Pintsuk2003] [Yakovlev2005] [Ocylok2010] (Fig. 2.7 (b)). The former style mixes elemental particles in a mixer and then distributes the mixture into different nozzles. In the latter style, dissimilar powder particles are sprayed out from different nozzles without premixing.

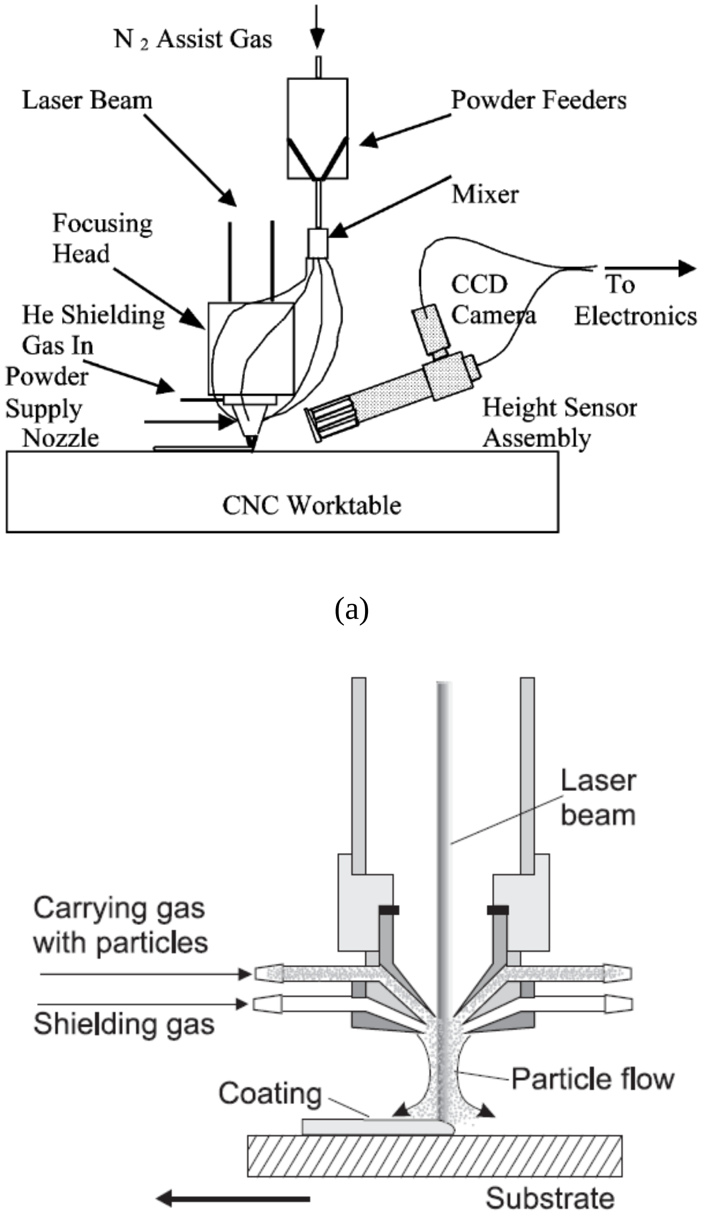

(a)

(b)

Fig. 2.7 Two different powder injection approach: (a) powder premixing [Shin2003], and (b) powder in situ mixing [Yakovlev2005].

The powder premixing approach can adjust the proportion of different powders, and the mixture of different powder particles are evenly sprayed out, subject to the same operation conditions, e.g., the trajectory and the time for interacting with the laser beam. This approach has the benefit of being easier to operate. However, the product quality can be affected. For this approach, segregation effect of dissimilar powders due to the different densities and remixing effects within the powder mixer exist, which increase the composition control difficulty and reduce the deposition accuracy. Moreover, the process flexibility is decreased. Compared to the former approach, the in situ powder injection approach is more flexible. Different powders are sprayed through different nozzles and mixed in the melt pool. The main advantage of this approach is that the powder composition can be adjusted on demand, and the aforementioned defects are avoided.

The design of the injection nozzle system can not only affect the trajectory of powder particles, but also affect the laser attenuation and thus the substrate heating. Most of the currently used print heads are coaxial since they are more likely to deposit a symmetric clad, allowing the fabrication to be omnidirectional. The coaxial nozzles can be generally classified into two categories: continuous coaxial nozzles and discrete coaxial nozzles [Lamikiz2011]. Specifically, the continuous coaxial nozzles can be a single ring-shaped nozzle [Lin1999a] [Pan2006] [Tabernero2010] [Cheikh2012] [Whitfield2008] (Fig. 2.8 (a)), or a single ring-shaped nozzle with inner wall shorter than the outer wall [Liu2005a] [Qi2006a] [Buongiorno1994]. The discrete coaxial nozzles can be a coaxial nozzle array consisting of typically four or more inward sub-nozzles [Guo2004] [Lowney2000] [Nowotny2000] [Lewis1995] (Fig. 2.8 (b)), or outward sub-nozzles [Zekovic2007] [Kong2010] [Tabernero2012] [Peng2006] [Everett1993] [Miyagi2010] (Fig. 2.8 (c)).

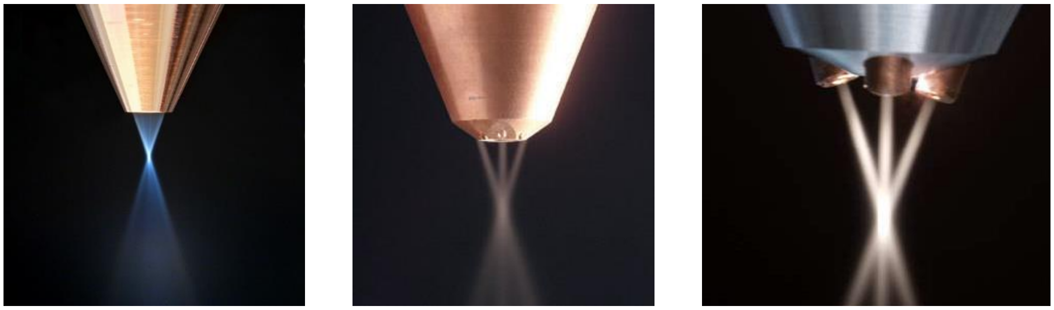

(a) (b) (c)

Fig. 2.8 Typical designs of injection nozzles (photo courtesy Reis lasertec and Fraunhofer ILT).

Yet, present studies do not investigate the geometrical details of injection nozzles. Basically, the shape of the injection nozzles can be classified into three types (Fig. 2.9): e.g., straight chamber [Lin1999a] [Whitfield2008] [Guo2004] [Lewis1995] [Buongiorno1994] (Fig. 2.9 (a)), truncated cone [Morville2012a] [Pan2006] [Sato2005] (Fig. 2.9 (b)), or truncated cone with straight chamber at end(s) [Peng2006] [Pyritz2002]

[Everett1993] (Fig. 2.9 (c)).

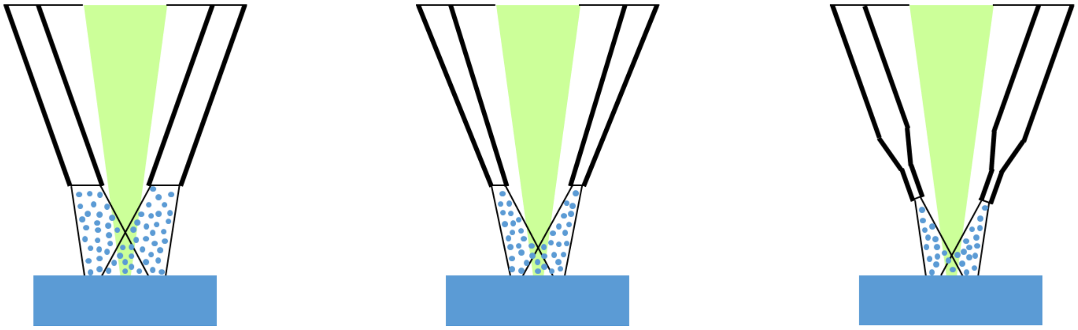
(a) (b) (c)

Fig. 2.9 Typical internal geometry designs of injection nozzles.

The nozzle geometry can affect the powder trajectories during injection. For example, Lin compared the powder distribution for both an inward position nozzle and an outward position nozzle through FLUENT simulation, and he found that the peak powder concentration of an inward position nozzle is about 50% of that of outward position nozzle [Lin2000a]. Pan et al. investigated the gas flow and powder distribution with respect to powder properties, several different nozzle shapes, and shielding gas settings based on continuous coaxial nozzles, and they found that the particle concentration mode is influenced significantly by nozzle geometries and gas settings [Pan2006]. Balu et al. parametrically studied the effects of injection angle on the powder distribution using both single powder and premixed multi-material powder based on discrete coaxial nozzles

[Balu2012]. Grigoryants et al. experimentally showed that a convergence angle of 52° results in a minimum width of the single bead, and a convergence angle of 64° gives a maximum width of bead, using continuous coaxial nozzles [Grigoryants2015]. Still, these research findings focus more on the effects of the external configuration of nozzles instead of on their interior geometry, and a systematic geometrical design for injection nozzles is missing.

2.3 FGM Parts Fabrication by DMD

2.3.1 Deposition Materials

Ever since multi-material deposition using the LENS^{TM} or DMD technology was performed and published in the late 1990s [Griffith1997], the investigations and fabrications of simple FGM parts have been reported in a number of papers [Huang2000b] [Morvan2001] [Huang2001] [Huang2002] [Shin2003] [Thivillon2009] [Müller2013]. In order to fully take advantage of the potential of heterogeneity in objects, the ability to manufacture the material distribution and shape according to a part’s design is needed. An FGM part example is shown in Fig. 2.10, where the two materials (LRF SS316 and Rene88DT) are smoothly graded layer by layer.

Previous studies have shown that DMD and similar processes have the potential for fabricating FGM parts, and some of the research work has been well summarized by Qi et al. [Qi2006a]. Many other publications are focused on the characterization of the FGM parts built by the DMD process. For example, Lewis et al. [Lewis2000] built a plate with transition from commercially pure titanium to 80Ti-20Nb alloy, Liu et al. [Liu2003] fabricated a TiC/Ti composite material with compositions ranging from pure Ti to 95 vol% TiC. Yakovlev et al. [Yakovlev2005] built stellite and SS 316L composite structures. JPL (Jet Propulsion Laboratory) of Caltech [Hofmann2014] also demonstrated the ability of DMD to fabricate heterogeneous objects in both axial and radial directions, and they have examined and tested the mechanical properties of the built parts. In addition, Ocylok et al. used tensile tests and hardness tests to study the mechanical strength of the FGM parts made of Marlok and Stellite 31 powders [Ocylok2010]. Soodi et al. investigated the tensile strength and fracture mechanisms of FGM parts using different metal/alloy powders, i.e. 316 SS with 420 SS, Colmonoy6 with 316 SS, AlBrnz with 420 SS, and 316 SS with tool steel [Soodi2014]. The effects of laser power and powder mass flow rates of SS316L and Inconel 718 on the microstructure and physical properties such as hardness, wear resistance, and tensile strength of FGM were discussed by Shah et al. [Shah2014]. These published results show the improvement of certain properties of a part when compared to a homogeneous part.

2.3.2 Challenges in Quality of Parts

Challenges exist in the fulfillment of the desired FGM parts' quality such as mechanical properties and thermal properties. An unexpected local composition could seriously affect the performance of the FGM part. To achieve the goal from the design, a well-mixed and smooth-transitioned part is required. Therefore, the manufacturing system should be capable to selectively apply different material components at user defined regions of a build, and allow the change in powder compositions on-the-fly [Ensz2002]. Development of the process also needs other considerations, such as mutual dissolution of powders to form the intermetallic phases [Yakovlev2005], gas dynamics and in-flight thermal constraints to trace the particle dynamics and temperature evolution [Lin1999a] [Grujicic2001] [Morville2012a] [Wen2009].

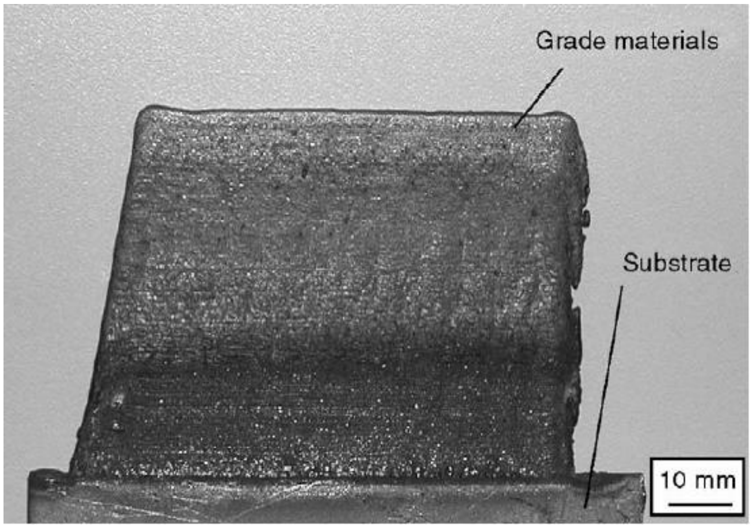

Fig. 2.10 The solid form of the LRF SS316/Rene88DT FGM [Lin2005].

However, the critical issue of crack failure remained in the past explorations of DMD fabrication of FGMs. For example, solidification cracks or elemental segregations at the grain boundaries, dendritic structures, and porosities for graded Ti-6Al-4V/Inconel 718 parts were observed [Domack2005] [Shah2008]. Pores and cracks were found in the functionally graded titanium and aluminum alloy systems [Shishkovsky2012]. Other titanium and nickel alloys have been previously functionally graded but only with very limited success [Lin2005] [Xu2009] [Lin2007] [Chen2011]. The occurrence of cracking and other failures is due to metallurgical and/or mechanical issues [Pulugurtha2014]. Cracking is a result of accumulated internal stresses due to multiple rapid cooling cycles and mismatches in thermal and mechanical properties between the powders and the substrate, forming unwanted intermetallic phases [Liu2006]. Although numerous researchers investigated the cracking/failure mechanisms and parametric studies on part quality have been carried using single material [Li2000] [Pinkerton2004] [Liu2005c] [Krishna2008] [Zhao2009] [Gu2012], very few work focused on tailoring the process parameters to fabricate crack-free smoothly transitioned FGM parts. Earlier studies showed that the characteristics of the final FGM parts can be affected by a number of process parameters. Yakovlev and Shah studied the effects of laser modes (pulsed and continuous) on the geometry and microstructure of FGM parts [Yakovlev2005] [Shah2008]. Shah also investigated the effects of specific energy and line mass on the microstructure and physical properties (residual stress, hardness and wear resistance) [Shah2014]. Mahamood et al. produced functionally graded Ti6Al4V/TiC parts composites with optimized process parameters obtained from empirical model and demonstrated their superior wear resistance and microhardness behaviors [Mahamood2015]. Zhang et al. deposited thin walls of different ratios of Ti and TiC with optimized process parameters, and they showed that there was no clear interface between layers and the microstructure and hardness change smoothly with composition changes. However, their optimization method was unclear [Zhang2008].

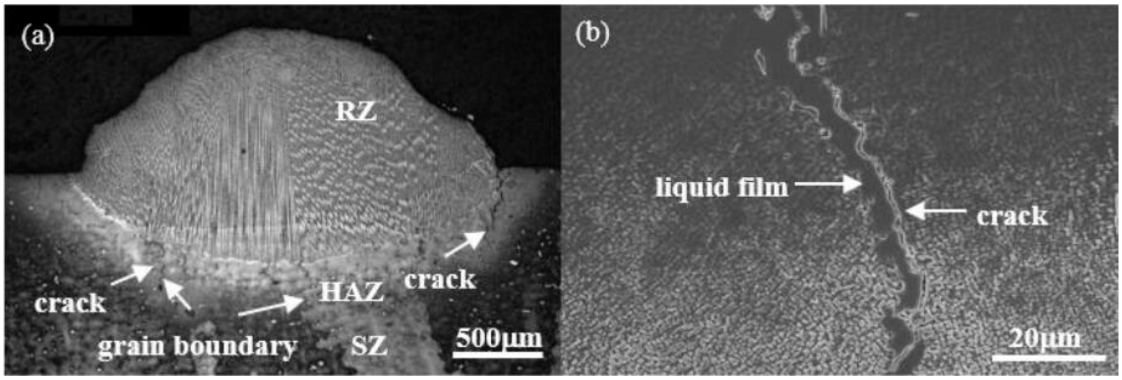

Fig. 2.11 Typical microstructure of LFRed K465 deposition: (a) morphology of LFRed deposition and (b) cracking characteristics in HAZ [Li2016].

2.3.3 Modeling the DMD of Multi-Material

Still, these studies are limited to experiments without modeling. Balu et al.

[Balu2012] established a computational fluid dynamics (CFD) based powder flow model to characterize the coaxial powder flow behavior of Ni-WC composite powders. Both numerical and experimental results reveal the optimal process parameters used, such as the exact stand-off distance where the substrate needs to be placed, the diameter of the powder stream at the stand-off distance, and a combination of suitable nozzle angle, diameter, and carrier gas flow rates to obtain a maximum powder concentration at the stand-off distance with a stable composite powder flow. But this study used a premixed powder in each nozzle instead of injecting different powders through different nozzles, and it still lacks the thermal modeling and the bonding process between the molten material and the heated substrate.

In terms of understanding heterogeneous material fabrication with the DMD process based on modeling and optimization, very few studies provide additional insight. The work of [Kumar1999] [Huang2000b] [Huang2001] [Siu2002] [Hu2006] [Kou2007] [Hu2008] [Wang2009] does target the design and optimization of heterogeneous components however not taking into consideration process relevant manufacturing constraints. In these papers, the deposition is uniform throughout each circular or straight track, allowing a composition change only at the next track/layer. This constrains the flexibility of the DMD's parts manufacturing potential with respect to process flexibility. To our knowledge, the investigation of composition change point by point has not been researched nor published. Meanwhile, despite the large number of reports on modeling and designing FGM parts, limited literature on the influence of the mixed/shared portion of a certain track/layer with its adjacent tracks/layers has been published. Moreover, the influence of the changing dilution rates and material properties during the process remain elusive when considering design for manufacturing.

2.4 Scope of the Present Study

Heterogeneous components, especially FGMs, can improve both mechanical and thermal properties of a part. In different applications, a part can have different mechanical or thermal loading functions, e.g., stress, strain, temperature, or heat flux. An FGM part with designed composition should be linked to a certain series of process parameters that can deposit precise composition and controllable resolution and manufacturing speed. The DMD technique for AM is a complex process governed by many strongly coupled physical phenomena. To facilitate the optimal design of its operating parameters, e.g. laser power, scanning speed, injection angles, injection speed, and particle size to guide the control of the manufacturing process, a comprehensive numerical model of the DMD process where concurrent delivery, deposition, mixing and solidification of two different metallic powders occur is needed.

In this dissertation, both analytical and numerical models are used to systematically investigate the effects of various process parameters on the process, and then the system and process parameters are designed to satisfy the manufacturing constraints and the composition requirements. The research starts from designing an injection nozzle to find out the relationship between the geometry of nozzle and the powder distribution. The design objectives are to maximize the powder usage and maximize the laser energy efficiency, in order to increase the process efficiency. Then, the powder mixing is considered in the second part of the research. In this part, dissimilar powders are taken into account for fabricating a heterogeneous object. The mixing efficiency is examined by studying the in-flight melting of powder particles and the melt pool convection. Dissimilar particles are injected from different nozzles and are subject to laser heating during the flight. The mixing of dissimilar materials is more efficient when the particles are in liquid phase. Meanwhile, a fast melt pool convection can also help with the mixing. Therefore, the second part of the research deals with particle in-flight heating and mixing, while maintaining the same design objectives. Last, a comprehensive investigation is conducted, which is the third part of the research. In this part, the links between the desired FGM part’s composition and the process parameters are explored considering the dilution and overlapping effects, as well as the varying parameters and varying material properties. Since the process physical properties are fully coupled with each other, a tailored plan for the varying process parameters is established to obtain a precise composition using analytical and numerical models. The models can also be used to perform sensitivity analyses and better understand the effects of the various parameters to then enable the optimal control of the process.

CHAPTER THREE

DESIGN OF INJECTION NOZZLE IN DMD MANUFACTURING OF THIN-WALLED STRUCTURES

3.1 Introduction

In this study, an injection nozzle design methodology is proposed based on the finite element modeling of substrate temperature and powder distribution. The design methodology is applied to the deposition of Ti-6Al-4V powder when building thin-walled structures. The methodology is also applicable to solid parts and other materials. This study focuses on building thin-walled structures because powder catchment is more difficult when building thin-walled structures, and nozzle designs that work for thin-walled structures will be more efficient for general 3D printing. The DMD process builds a part by using laser to melt a substrate and injecting powders into the melt pool. The most significant cost of the process are related to the laser energy consumption and the amount of building powders. Therefore, the objective of this study is to explore and define the shape of an injection nozzle for DMD that can maximize powder usage and minimize laser energy needs, later defined as powder catchment and laser energy efficiencies. Two models are used to accomplish this task. They simulate the laser heating of the substrate and the flow of the particle-laden gas respectively. First, a proper set of process parameters is chosen to model the melt pool shape on the substrate that can build a thin-walled structure of a certain width. Then the powder distribution is studied by testing various injection nozzle shape parameters based on the solutions of a particle-laden injection turbulent flow. A neural network is built in order to reduce computational cost while exploring the variations of objective functions that are due to changes in the design variables. The first output of the neural network predicts the particle concentration in flight. The second output evaluates the powder catchment efficiency. The process efficiency is defined as the product of the two outputs, since one of the design objectives (powder catchment efficiency) is either acceptable or not. After validating the neural network, multiple sets of injection nozzle geometric parameters are provided to map their process efficiencies. With the methodology proposed, the injection nozzle can be designed to maximize the process efficiency. Note that, after designing the nozzle, other factors such as the stand-off distance and the injection angle will also affect the powder distribution in the DMD process. These parameters for the external configuration of injection nozzles are discussed in the literature [Lin2000] [Pan2006] [Balu2012] [Grigoryants2015]. In this study, we only focus on the interior geometry of the injection nozzles.

The rest of the chapter is organized as follows. In Section 3.2, the numerical modeling of powder flow for a perpendicular injection nozzle is described and explained. In Section 3.3, the design procedure is provided using a neural network method and the problem is formulated, followed by design results. The discussion of design results is presented in Section 3.4, regarding the two design objectives. Section 3.5 summarizes the conclusions and future work.

3.2 Modeling the Particle-Laden Gas Flow

The laser energy efficiency can be estimated by the amount of powder deposited on the substrate within a time span, which is discussed in Section 3.3. The powder catchment efficiency is also named powder utilization ratio, or powder usage, which is defined as the ratio of the powder trapped in the melt pool to the total amount of powder deposited on the substrate within a certain amount of time. In previous work, the powder catchment efficiency was mathematically modeled and experimentally evaluated by Lin et al. [Lin1997] [Lin1999]. Zhou et al. developed an analytical model which assumed powder particles to be evenly distributed across the stream while being injected at constant speed [Zhou2011]. The effects of process parameters on the powder catchment efficiency were analyzed and an analytical expression was given by Liu et al. based on experimental results [Liu2014]. Pursuing a higher powder catchment efficiency is necessary, especially for making thin-walled structures where powder catchment is more difficult and thus could result in more powder waste. The nozzle designs that work for thin-walled structures will be more efficient for general 3D printing.

For the purposes of the study, a realistic set of data is assumed, and the design is performed for that case, although it can be generalized to other cases. The target thin-walled structure has a wall thickness of 0.7 mm (as shown in Fig. 3.1, for illustration). In order to assess the efficiency of the 3D printing process, it has to be modeled with a significant degree of accuracy. Therefore, COMSOL Multiphysics® is used as a finite element tool to model the laser substrate heating process and the particle-laden turbulent gas flow.

In the DMD process, the particles are injected into the melt pool by an inert carrier gas (argon typically). The general shape of a nozzle is typically designed to be composed of three sections (see Fig. 3.2). The top section is designed to connect the nozzle to a plastic tube that transports powder into it. The middle neck section works to increase the gas speed and to concentrate particles. The bottom section is designed to straighten the trajectories of particles.

Due to symmetry, studying the powder streams for coaxial nozzles can be converted to studying the powder stream for a single nozzle. Moreover, the gravitational force plays an insignificant role on the particle dynamics. Therefore, investigating the powder injection using inclined nozzles can be converted to investigating the powder injection for perpendicular nozzles in this study. To demonstrate the feasibility of the above mentioned conversion, the Froude number (the ratio of the flow inertia to the gravitational force) is used, which is defined as:

$$Fr = \frac{V_g}{\sqrt{gd_p}} \tag{3.1}$$

where V_g is the characteristic particle velocity, g is the acceleration due to gravity, and d_p represents the particle diameter. If V_g equals to 1 m/s, and d_p is 20 μm, it can be estimated that the Froude number is 71.4, which is far greater than 1. The particles in this study can be seen as "a bundle of particles", which means the trajectory of a single particle does not affect the contour of the whole powder jet: a cone shape with constant divergence angle. From Fig. 3.2 (a), it can be seen that the powder jet – substrate contact length changes with the injection angle θ. Fig. 3.2 (a) can be equated to Fig. 3.2 (b), where the substrate rotates instead of the injection nozzle while the shape of powder jet is intact. It can be demonstrated from geometrical relationships that the powder jet-substrate contact length increases with the injection angle - hence the powder catchment efficiency is lowered as θ increases (the outermost "ring" of particles inside the melt pool become outside). Besides, it has been proved by modeling and other literature that the powder always follows a Gaussian distribution [Morville2012] [Zekovic2007] [Wen2009] [Zhu2011]. Therefore, considering a perpendicular nozzle has little effect on the comparison among different designs. Also, the counting of the total number of particles on the substrate is not affected since the lowering of the left axis is assumed to be compensated by the lifting of the right axis, as shown in Fig. 3.2 (b).

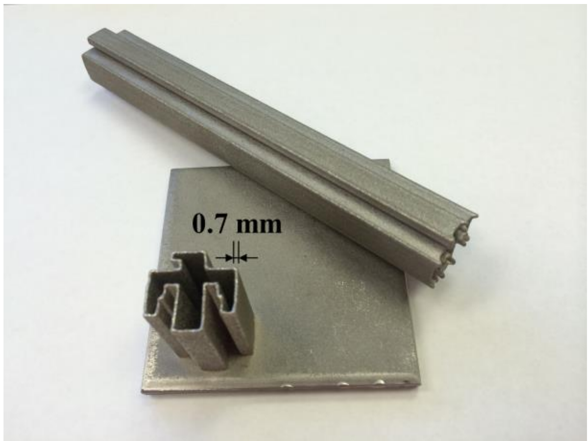

Fig. 3.1 A thin-walled structure built by DMD process with a 0.7 mm wall thickness (part manufactured at Optomec® Inc., Albuquerque, NM).

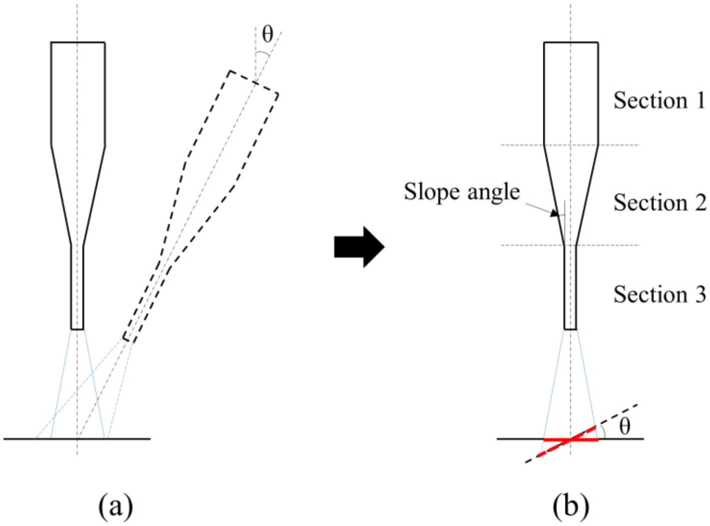

Fig. 3.2 Contact length between powder jet and substrate for different angles. The contact length is the shortest when the nozzle is perpendicular to the substrate.

The particle-laden jet flow is a two phase flow that incorporates a continuous gas phase and a discrete particle phase. The two phase flow is solved by first modeling the primary gas (Argon) phase using the standard *k*-*ε* turbulence model, and then incorporating the secondary particle phase. It is assumed that there is no heat transfer between gas and particles, and the particles remain in their solid phase in flight.

3.2.1 Modeling the Gas Turbulent Flow

The gas turbulent flow is modeled using Reynolds-averaged-Navier-Stokes equations and the standard *k*-*ε* turbulence model because it is the most efficient for engineering problems [Lin2000b] [Pan2006] [Zekovic2007] [Tabernero2010] [Ibarra-Medina2011] [Zhu2011] [Balu2012] [Morville2012a]. The Reynolds time-averaged equations for turbulent flow include conservation of mass, conservation of momentum, conservation of kinetic energy, and two transport equations regarding the kinetic energy and the dissipation of kinetic energy.

Conservation of mass:

$$\rho_g \nabla \cdot u = 0 \tag{3.2}$$

Conservation of momentum:

$$\rho_g \left(u \cdot \nabla \right) u = \nabla \cdot \left[- pI + \left(\mu + \mu_T \right) \left(\nabla u + \left(\nabla u \right)^T \right) - \frac{2}{3} \rho_g \right] \tag{3.3}$$

where $\mu_T = \rho_g C_\mu \frac{k^2}{g}$

Transport equation for kinetic energy:

$$\rho_g \left(u\cdot\nabla\right) k = \nabla\cdot\left[\left(\mu + \frac{\mu_T}{\sigma_k}\right)\nabla k\right] + P_k - \rho_g \tag{3.4}$$

Transport equation for dissipation of kinetic energy:

$$\rho_g \left(u\cdot\nabla\right)\varepsilon = \nabla\cdot\left[\left(\mu + \frac{\mu_T}{\sigma_k}\right)\nabla\varepsilon\right] + C_{\varepsilon 1}\frac{\varepsilon}{k}P_k - C_{\varepsilon 2}\rho_g\frac{\varepsilon^2}{k} \tag{3.5}$$

where $P_k = \mu_T\left[\nabla u : \left(\nabla u + \left(\nabla u\right)^T\right)\right] - \frac{2}{3}\rho_g k\nabla\cdot u$

In the above equations, ρ_g is the gas density (1.784 kg/m^3), u is the gas velocity vector, P is the pressure, μ and μ_T denote the laminar and turbulent viscosities respectively, P_k is the volumetric production rate of turbulent kinetic energy by shear forces, and k and ε are the turbulent kinetic energy and dissipation rate of turbulent kinetic energy respectively. The values of the turbulence model constants are taken from the default empirical values proposed by COMSOL Multiphysics®.

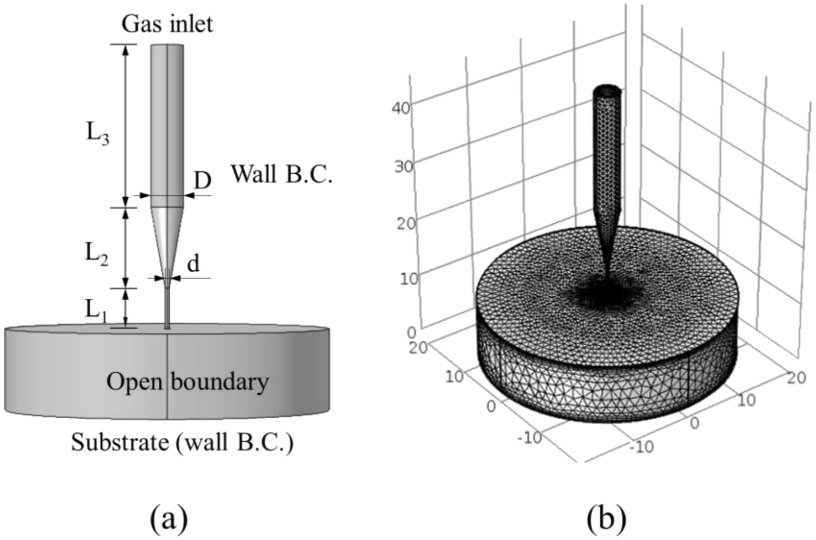

Fig. 3.3 3D calculation domain for powder flow model with boundary conditions (B.C.) and mesh.

The physics-controlled calculation domain is shown in Fig. 3.3, where a cylindrical domain for powder flow is created beneath the injection nozzle. The delivery gas is assumed fully developed at the nozzle inlet with a mean velocity of 1 m/s (and maximum velocity of 2 m/s), which is expressed as:

$$u_{in} = 2 \times \left(1 - \frac{x^2 + y^2}{r^2}\right) \times u \tag{3.6}$$

where r is the inlet radius, x and y represent the coordinate positions, and u is the inlet gas mean velocity into the nozzle. The lateral boundary between the nozzle tip and the substrate is set as open boundary with zero normal stress. Wall functions bouncing boundary condition (B.C.) is set for all the other boundaries. The calculation is performed to find a time-averaged stationary solution.

3.2.2 Modeling the Particle Dynamics

The discrete phase is calculated by building the particle track model and solving the particle kinematics equations. The trajectory of a dispersed phase particle is solved by integrating the force balance on each particle in a Lagrangian reference frame. The particle dynamics is driven by the gas flow drag force. The force equation balances the particle inertia and the drag force acting on the particle. The drag law is set to Harder-Levenspiel [Morville2012a], and the force balance equation in COMSOL Multiphysics® takes the form below.

$$\frac{du_p}{dt} = \frac{1}{\tau_p} m_p \left(u + \zeta \sqrt{\frac{2k}{3}} - u_p \right) \tag{3.7}$$

where $\tau_p = \frac{4\rho_p d_p^2}{3\mu C_D \mathrm{Re}}$, $\mathrm{Re} = \frac{\rho_p D_p \left| u_p - u_g \right|}{\mu}$, and

$$C_D = \frac{24}{\mathrm{Re}} \left[1 + A\left(S_p\right) \mathrm{Re}^{B\left(S_p\right)} \right] + \frac{C\left(S_p\right)}{1 + D\left(S_p\right) / \mathrm{Re}}$$

In the above equations, u_p, d_p, m_p, ρ_p are the velocity, diameter, mass, and density of a single particle, respectively; Re is the Reynolds number, C_D is the drag coefficient; S_p represents the particle sphericity, which is defined as the ratio of the surface area of a volume equivalent sphere to the surface area of the considered non-spherical particle. A, *B, C* and *D* are the empirical correlations of the particle sphericity. The turbulent dispersion is added with the term $\zeta\sqrt{\frac{2k}{3}}$, where ζ is a normally distributed random number with zero mean and unit standard deviation.

As for the B.C.s, the particles' inlet boundary conditions are similar to those of the gas inlet, and 1350 particles are released every 0.001 s for a total 0.02 s, resulting in a 1.5 g/min powder feed rate. The particle distribution density is set to be proportional to the gas velocity at the nozzle inlet, following a parabolic distribution. A "freeze" wall B.C. is set for the substrate surface, where a particle's velocity is displayed in COMSOL at the moment when it strikes the substrate. A "disappear" wall B.C. is set for the lateral outlet. A "bounce" wall condition is set for all the other boundaries. The calculation is performed for 0.05 s with a step size of 0.001 s.

The quantification of particle numbers is carried by the following procedure. First, the suitable process parameters are selected to induce a melt pool with appropriate size for making thin-walled structures (about 0.7 mm width), as shown in Fig. 3.4. The 200 W attenuated laser power (assuming the attenuation is uniform throughout the laser beam) is selected, and the laser spot radius is chosen as 0.5 mm. The modeling procedure is not shown here since it is a typical heat transfer by a moving heat source (Gaussian) problem with convection and radiation B.C.s. Second, the resultant melt pool region is estimated by an ellipse, whose major axis is 0.7 mm and minor axis is 0.6 mm, as measured from

Fig. 3.4. The melt pool region is then created in the calculation domain for powder flow in order to quantify the number of particles dropped into this region. Last, both the particle number in the melt pool and the total particle number on the substrate are respectively calculated.

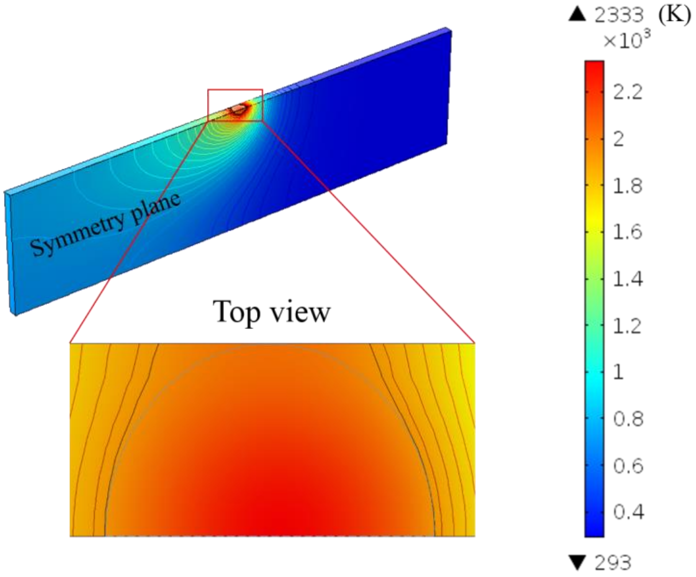

Fig. 3.4 Simulation result for laser substrate heating at t = 1 s. Figure displays half of the solution domain due to symmetry (the symmetry plane is shown in the figure).

3.3 Design Procedure and Results

In this study, we formulate that the injection nozzle geometric design should result in a maximum laser energy efficiency, and a powder catchment efficiency of no lower than 90%. The distributions of particles are examined for a series of combinations of nozzle geometric parameters, allowing the process efficiencies to be calculated for each combination.

Herein, we set the distance between the nozzle orifice and the substrate a constant 10 mm. The five geometric parameters (L_1, L_2, L_3, d, and D) of a nozzle can be found in Fig. 3.3. Since the inlet gas flow is assumed to be fully developed, the length of L_3 would have little effect on the powder flow and is fixed to 20 mm. The other four parameters are chosen to be design variables. Table 3.1 shows the ranges and possible values of the four design variables.

Table 3.1 Value ranges of design variables and their discrete values for testing.

	L_1 (mm)	L_2 (mm)	d (mm)	D (mm)
Range	0 – 20	5 - 20	0.5 - 1.5	4 - 6
Step size	1	1	0.1	0.5
No. of values	21	16	11	5
Discrete values chosen to test	0, 5, 10, 15, 20	5, 10, 15, 20	0.5, 1, 1.5	4, 6

According to Table 3.1, there could be thousands of possible combinations (21×16×11×5) of the design variables, and each simulation takes up about 3 hours to complete, computational cost is high if running all the simulations. Consequently, several discrete values are chosen for each variable as evenly distributed in their value ranges, as shown in Table 3.1, resulting in a total combination of 120. The outputs for any other possible combinations can be predicted using a properly defined and trained neural network.

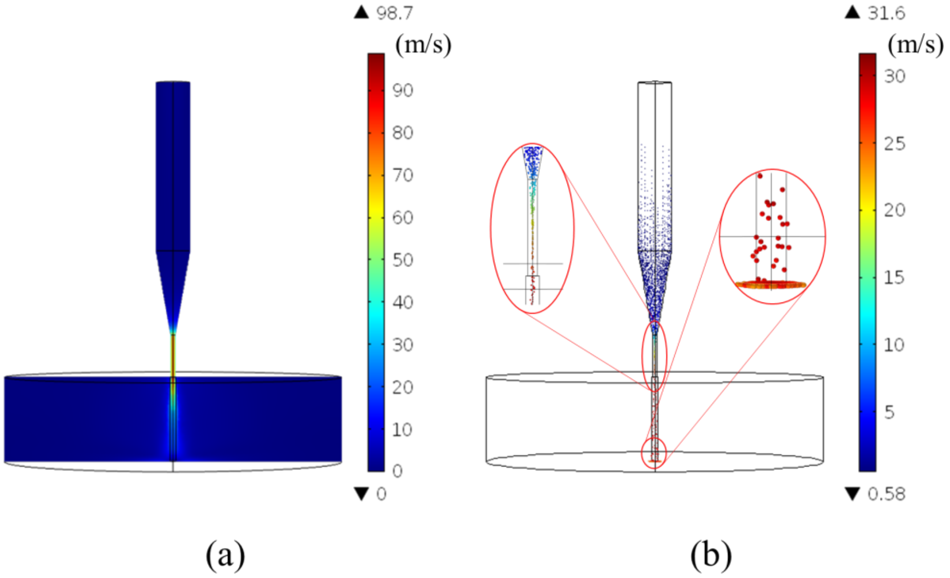

Fig. 3.5 Simulation results for a) gas flow without powder (cross-sectional view), and b) powder flow at 0.05 s.

The time averaged stationary solution for gas flow and time dependent solution for particle dynamics are presented in Figs. 3.5 (a) and (b) respectively (L_1 = 5 mm, L_2 = 10mm, D = 4mm, and d = 0.5 mm). The gas quickly accelerates at the bottom of the neck, and the color bar represents the gas velocity. The gas then decelerates when jetting out of the nozzle after a certain distance and strikes the substrate.

The concerned quantities for the design include the total number of particles on the substrate, and the portion of the former dropped in the melt pool. The total number of particles on the substrate is of concern because it is related to the laser energy efficiency in the way described as follows. The laser energy efficiency is mainly determined by the attenuation due to the particle shadowing effect, which is calculated using the Beer-Lambert Law [Jouvard1997] [Lin2000] [Han2004] [Pinkerton2007] [Zhou2009] [Tabernero2012]:

$$I_{laser} = I_{init} e^{-\varepsilon C(z)} \tag{3.8}$$

where I_{init} is the initial laser intensity (W/m^2) before entering the powder cloud, and ε, the molecular absorptivity or extinction coefficient (m^2/kg), can be evaluated as [Jouvard1997] [Zhou2009]:

$$\varepsilon = \frac{3\eta}{2 r_p \rho_p} \tag{3.9}$$

where r_p is the particle radius, $C(z)$ is the concentration of the particles (kg/m^3) as a function of the vertical penetration distance z. Then the rest of the exponential term is:

$$C(z) = \int_0^h \frac{F}{V_p S(z)} dz \tag{3.10}$$

where h is the laser - powder interaction height, F is the powder feed rate, V_p represents the particle velocity at the z plane, $S(z)$ denotes the cross section area of the particle beam at a vertical plane z. In order to improve the laser energy efficiency, the attenuated energy by powder cloud should be minimized. It can been seen from Eq.s (3.8), (3.9), and (3.10) that the laser attenuation is dependent on V_p. However, the particle velocity is a spatial variable beneath the orifice and carrying numerical integration would be extremely time consuming for the 120 testing cases. Therefore, we take the total number of particles on the substrate as an alternative measurement for particle concentration: a larger number indicates a spatial averagely higher particle velocity, and thus a lower average concentration; hence a higher laser energy efficiency. So the transformation from measurement of laser attenuation to the measurement of total number of particles on the substrate is employed, and this is the first output from simulation.

The second output is the powder catchment efficiency. The amount of particles in the melt pool region is counted as well as the amount of particles on the substrate. The resultant powder catchment efficiencies from the simulation are in a range of about 20% to 100%. Comparing with the values stated in other literature (around 70% at best) [Lin1997] [Lin1999] [Liu2014], the results in this parametric study show a variation of powder catchment efficiency from close to 0% to almost 100%, indicating a potential of approaching perfection. Particularly, the powder catchment efficiency is classified into 0 and 1, where 0 represents a powder catchment efficiency lower than 90% and 1 over 90%.

The aforementioned 120 samples are simulated and their outputs are documented for the Neural Network training and validation. A backpropagation (BP) Neural Network (NN) with one hidden layer and five nodes is created to predict the two outputs for any parametric case. Among the 120 samples, 100 random samples are chosen to train the neural network, and the remaining 20 samples serve to validate the trained network. The errors for the two outputs are defined and evaluated as follows.

$$\begin{aligned}&\text{First output: error} = \frac{1}{\text{No. of samples for validation}} \sum_{\text{n=1}}^{20} \left| \frac{\text{prediction}_{\text{n}} \text{-actual}_{\text{n}}}{\text{actual}_{\text{max}} - \text{actual}_{\text{min}}} \right| \\ &\text{Second output: error} = \frac{\text{No. of inaccurate predictions}}{\text{No. of samples for validation}}\end{aligned} \tag{3.11}$$

The main errors are obtained by performing the training and validation of the BP NN for 20 times. The typical results (single performance) for the NN prediction and classification are presented in Figs. 8(a) and (b) respectively, and the prediction errors for every performance are listed in Table 3.2. It can be calculated that the mean errors for the two outputs are 1.62% and 8.75%, with standard deviations of 0.92 and 4.55 respectively. The variation of the errors is due to the applied initial weights associated with the input variables of the neural network, and the randomness of the initially employed training and validation samples.

In order to find the designs that meet the two objective functions, we define the process efficiency as the product of the two outputs:

$$M = \text{function output 1} \times \text{fu} \tag{3.12}$$

where the function output 2 (powder catchment efficiency) is used as an eliminator, i.e., *M* equals to 0 if the powder catchment efficiency is lower than 90%, then the corresponding design is eliminated. The value of function output 1 become the new judgment after eliminating the unwanted designs by function output 2. The objective designs are those who are linked to the largest *M* values.

Using the developed NN, the function output 1, function output 2, and *M* can be predicted for all the remaining 18360 designs (Fig. 3.7). The x-axis represents the number of designs, arranging them in an iterative way, i.e., D has the highest cycling frequency, followed by d, L_2, and L_1 (their values are referred by Table 3.1). The results are further confirmed by running the prediction process for many more times, resulting in similar results, i.e., the results obtained from a new run overlap well with the results from previous runs. This confirms that the randomly chosen training/validation samples and the randomly applied initial weights do not significantly affect the final results, but only affect the relative prediction errors.

Table 3.2 Error of testing results for the neural network.

Performance No.	1	2	3	4	5	6	7	8	9	10	11	12	13	14	15	16	17	18	19	20
Output 1 error (%)	1.1	0.7	2.2	1.4	1.1	2.0	0.2	1.1	4.4	1.2	2.1	1.9	1.0	0.4	1.7	1.5	1.3	2.2	2.6	2.3
Output 2 error (%)	5	15	5	0	10	10	15	10	15	10	5	0	10	10	10	5	10	15	5	10

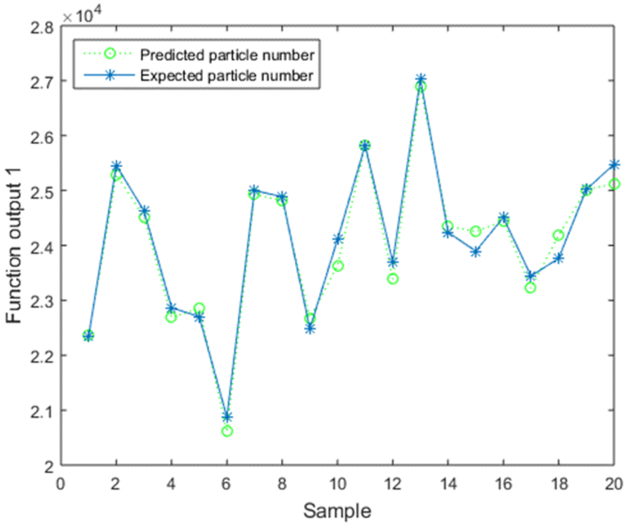

(a)

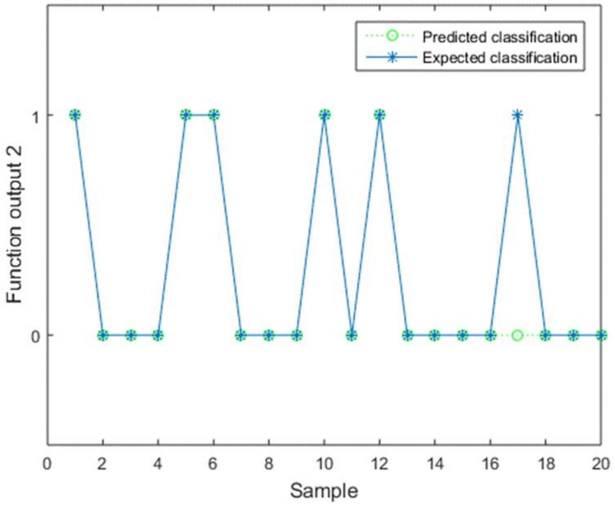

(b)

Fig. 3.6 The expected values and the predicted values for the neural network validation: a) prediction of total number of particles on the substrate, and b) classification of particle catchment efficiency.

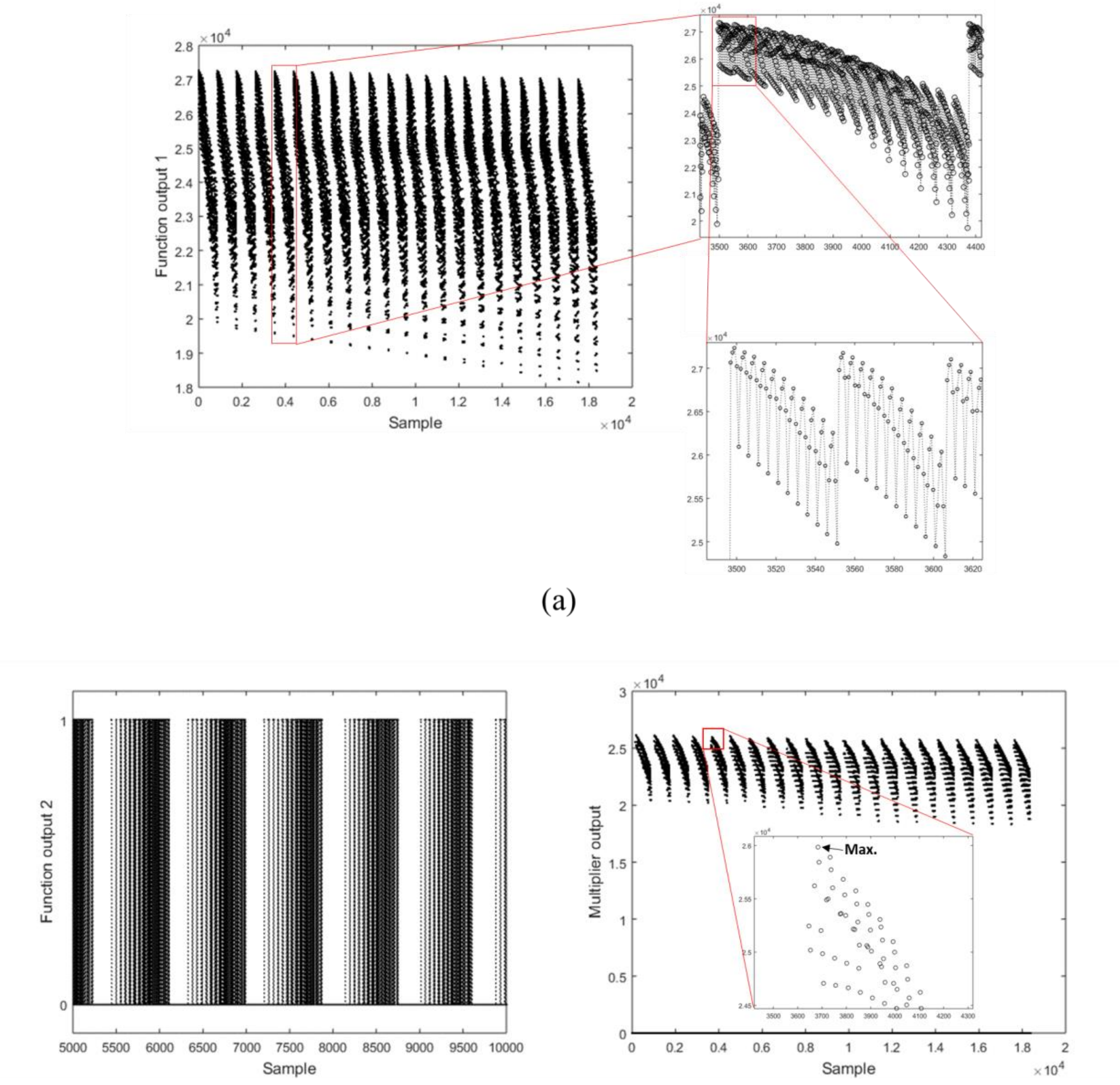

(a)

(b)

(c)

Fig. 3.7 Prediction results for all the rest 18360 designs: a) function output 1, b) function output 2 (taking sample numbers from 5000 to 10000 for a closer view), and c) the *M* values.

It can be seen from Fig. 3.7 that similar groups of results repeat periodically. The non-zero values form a “scale-like” arrangement, and appear in a frequency of about 880 samples. The prediction results can be divided into 21 groups by the clear gaps among them. When zooming into each group, two more iterative loops can be identified, as shown in the partially enlarged views of Fig. 3.7 (a). The three iterative loops indicate the effects of the alternation of the design variables (L_1, L_2, and d). For example, each of the 21 “top-level scale” corresponds to a single L_1 design value, and so forth.

The peaks (maximum *M* values) correspond to the theoretically best designs, and Fig. 3.7 shows that actually 21 peaks exist. If the slight difference among these 21 peaks is negligible, then the 21 peak values would correspond to 21 feasible designs, shown in Table 3.3. The resultant designs have not considered manufacturing or other assessment criteria, which is beyond the scope of this research, but we believe there should not be any significant issue. Table 3.3 also shows that the resultant L_2 values are from 6 mm to 9 mm, and they tend to increase with L_1. The upper diameter D is 4 mm or 4.5 mm, and the bottom diameter d is 1.5 mm. It should be mentioned that though 4 mm appears to be the most common value of D, repeated calculation reveal that 4.5 mm shares almost the same occurrence frequency. This is due to the nature of the neural network approach and certain randomness of the process. The situation is similar for L_2. Take design No.1 for example, repeated calculations may result in different L_2 values (5 mm, 6 mm, or 7 mm).

But what is unchanged is that the resultant D cannot be larger than 5 mm, and d is almost always 1.5 mm. Rather than focusing on the exact dimensions of a design, this study investigates the trends that can guide a design.

Table 3.3 The injection nozzle shape designs.

No.	1	2	3	4	5	6	7	8	9	10	11	12	13	14	15	16	17	18	19	20	21
L_1	0	1	2	3	4	5	6	7	8	9	10	11	12	13	14	15	16	17	18	19	20
L_2	6	6	5	5	7	7	6	6	6	8	7	7	7	8	8	8	8	9	9	9	9
d	1.5	1.5	1.5	1.5	1.5	1.5	1.5	1.5	1.5	1.5	1.5	1.5	1.5	1.5	1.5	1.5	1.5	1.5	1.5	1.5	1.5
D	4.5	4.5	4	4	4.5	4.5	4	4	4	4.5	4	4	4	4	4	4	4	4	4	4	4

3.4 Discussion and Data Analysis

The design basically expects more particles dropping on the substrate and more particles dropping in the melt pool. The objective is the geometric design of injection nozzles that deposit Ti-6Al-4V powders to form a 0.7 mm thin-walled structure. Besides a small laser beam spot size, the thin deposition target requires small-diameter injection nozzles as well. The diameter for the bottom section of the nozzle is preset between 0.5 mm and 1.5 mm since some preliminary tests show that too large a diameter will significantly disperse the particles, thus lowering the powder catchment efficiency. The diameter for the upper section of nozzle is preset from 4 mm to 6 mm to assure that it is easy to connect to a powder delivering pipe. The convergence for stationary solutions of gas flow become more difficult to achieve if this diameter is larger than 6 mm, and only time-dependent solutions exist, indicating an unsteady particle laden gas flow and a poor manufacturing consistency.

1. Process parameters. The melt pool size under different process parameters can be predicted from simulation, experimental determination, or both, such as in [Amine2014] [Ermurat2013] [Emamian2010] [Tabernero2013]. In the current study, however, the injection nozzle design is the focus, and no further simulation tests are necessary as long as the feasible laser parameters are found. The process parameters used are 200 W (attenuated) Gaussian laser beam, 10 mm/s scanning speed, and 0.5 mm laser spot radius. Since it is well known that increasing the laser power has an equivalent effect as decreasing the scanning speed and/or decreasing the laser spot size, in fact, there are more than one feasible process parameters that can meet the requirements. An alternative feasible solution, for example, is: 280 W laser power, 20 mm/s scanning speed, and 0.3 mm laser spot radius.

The estimated melt pool region is an inscribed ellipse within the simulated melt pool, taking up about 93% of the whole melt pool area. There are two reasons to justify this approximation. First, rather than overestimating the powder catchment efficiency, an underestimated efficiency is preferred. With this approximation, the powder catchment efficiency would be slightly underestimated. Second, the definition of the melt pool region affects the finite element mesh for the gas flow simulation. A perfect symmetrical melt pool region is beneficial to the solution convergence.

2. The first objective function: laser energy efficiency. Based on the aforementioned theory, the total number of particles on the substrate is the object of study. Although the number varies between 20000 and 27000, the corresponding driving force and thus the resultant average particle velocity beneath the nozzle can vary from less than 10 m/s to tens of meters per second (> 60 m/s). It can be estimated from Eq.s (3.8) to (3.10) that the attenuation varies from 0.8 to 0.5 when the average particle velocity varies from 10 m/s to 30 m/s. This is a considerable drop of attenuation, meaning that about 30% more laser power can be preserved if we increase the particle velocity from 10 m/s to 30 m/s.

The following trends can be observed. First, Fig. 3.7 (a) shows that L_1 has little effect on the total number of particles on the substrate, since there is no great difference among the 21 streaks. The slight decreasing trend can be due to the difference of L_1 length: it takes the particles more time to reach the substrate given a longer L_1. Second, the number of particles decreases with L_2 and d. A sharp decrease can be observed (the “tail” of each streak) as L_2 goes toward its maximum. The decreasing trend for d can be seen from the first partially enlarged view of Fig. 3.7 (a). Both the increase of L_2 and d actually decrease the slope angle of nozzle, which is marked in Fig. 3.2. A small slope angle can decrease the gas flow speed, and thus decrease the particle speed. Third, it can also be seen from the second partially enlarged view that the number first increases and then decreases as D increases from 4 mm to 6 mm. The maximum is reached when D equals to 5 mm, while the minimum is reached when D is 6 mm, and this trend becomes more obvious as L_2 and d increase. Despite the preference for a large slope angle, particles would suffer more from the bouncing effect if this angle is too large, weakening the particle-accelerating effect.

3. The second objective function: powder catchment efficiency. The powder catchment efficiency is classified as 0 and 1, using 90% efficiency as a partition criterion. Although it is hard to tell exactly what effect does each design variable have on the output from Fig. 3.7 (b) and Fig. 3.8, it is clear that the "gap" among the 21 groups tends to get larger as L_1 increases. This means more 0s are obtained as L_1 goes larger, since only 0s appear in the gap regions. Additionally, within each group of data, there are more 1s as L_2 increases, which can be seen from the first partially enlarged view of Fig. 3.8. Further examining the second partially enlarged view of Fig. 3.8, one can tell that the occurrence frequency of 1s gets higher from left to right, meaning that the powder catchment efficiency gets higher as d increases. However, the trend with D is not obvious from Fig. 3.8.

The initial purpose of adding the bottom section (L_1) is to further straighten and concentrate the powder flow. However, low powder catchment efficiency is more likely to occur for a longer L_1. The explanation of this phenomenon can be found in Fig. 3.5 (b). We can see that the powder has already concentrated in the middle of this section and begins to spread out after passing the most concentrated point (waist). The expanded powder beam is like a cone, and the further it goes down, the larger its cross section area would be. Hence a longer L_1 gives the powder more space to expand, enlarging the cross section area, thus decreasing the chance of a single particle to drop into the melt pool.

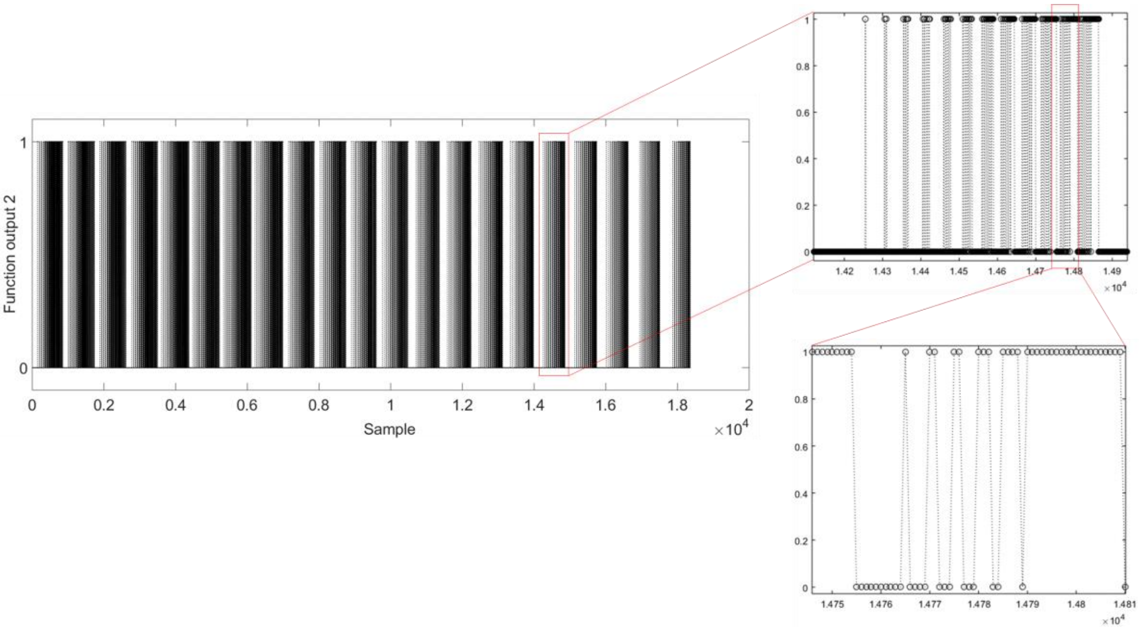

Fig. 3.8 Neural network prediction for powder catchment efficiency.

The powder catchment efficiency increases with L_2 and d. In fact, these two parameters determine the slope angle of a nozzle. The increase of L_2 and d leads to the decrease of the slope angle. The nozzle looks much “smoother” for a smaller slope angle, thereby the particles bounced by the nozzle wall become straighter down. Consequently, the particles are less likely to bounce away. Moreover, the powder beam waist would appear later in a lower place, allowing a shorter distance for the powder to further expand. Based on the above conclusions, we can also infer that the effect of D is similar: a larger D brings a larger slope angle, resulting in a lower powder catchment efficiency.

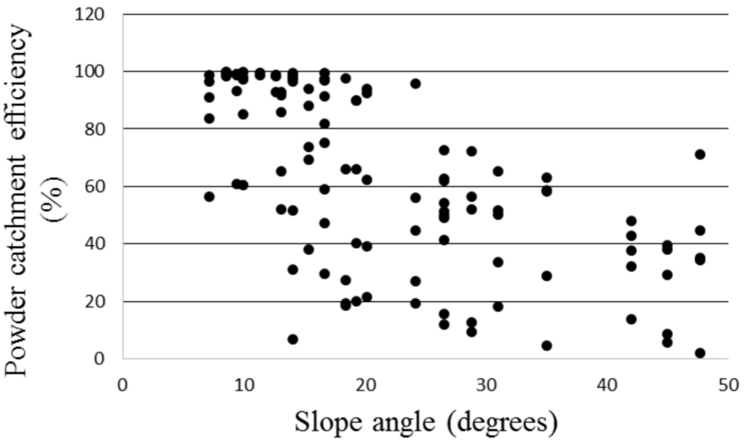

Fig. 3.9 The sample data points showing the relationship between the slope angle and the powder catchment efficiency in percentage.

Figure 3.9 plots the slope angle versus powder catchment efficiency. It can be seen that the points correspond to powder catchment efficiencies higher than 90% are all clustered in the low slope angle region. The powder catchment efficiency has a decreasing trend with the slope angle, with the R value equals to 0.65. They are not very significantly correlated, because the final effect is the synergy of all the design variables. Meanwhile, the whole physical process is a coupled two-phase flow, and factors including some random terms can also affect the final result. As shown in Fig. 3.9, though, the correlation coefficient between slope angle and powder catchment efficiency is not high, if we classify the efficiency into 0 and 1, it is clear that all 1s appear at smaller slope angles.

4. Final design results. After multiplying by the eliminator (powder efficiency), it can be seen from Fig. 3.7 (c) that a proportion of the results from function output 1 fall on the bottom line due to the corresponding 0 values from function output 2. The maximum values emerge not among the first several data points in each of the 21 groups, but after about 100 data points. Thus, it can be seen that all the data points with relatively large values from function output 1 are eliminated by the eliminator, and the largest value in the remaining samples is about 26000.

To summarize, the preference for injection nozzle geometric parameters regarding the two objective functions and the final designs are shown in Table 3.4. As discussed before, on the one hand, the first objective (laser energy efficiency) favors minimum L_2 and d, and a medium D. On the other hand, the second objective (powder catchment efficiency) favors maximum L_2 and d, and minimum D. Both objectives have no obvious preference for L_1. The two objective functions drive the final designs simultaneously, resulting in a small L_2 (about 5 mm to 9 mm), a small D (4 mm or 4.5 mm), and a maximum d (1.5 mm). The results reveal that L_2 is more driven by the first objective function, while d is more driven by the second objective function. Since 4 mm and 4.5 mm have the same occurrence frequency for D, it can be considered as driven by both objectives functions.

Table 3.4 Summary for the parameters preference of the two objectives and the final designs.

	L_1	L_2	d	D
Objective 1	N/A	Min.	Min.	Medium
Objective 2	N/A	Max.	Max.	Min.
Final designs	N/A	Small	Max.	Small

As illustrated in Fig. 3.7 (c), the least effort should be made for designing L_1, since each point in one of the 21 groups of results can find its counterpart in every other groups. However, the design for L_1 should be considered when it comes to manufacturing constraints, which is beyond the scope of this research. Generally speaking, it is more economical to make a nozzle without the bottom section, or in other situations such as the total height of the print head is limited. Conversely, a longer nozzle is needed if a certain stand-off distance is asked to protect the optical apparatus from heat. Likewise, L_3 is also adjustable in case other design or manufacturing constraints exist. Therefore in this study, one of the design output can be: $L_1 = 0$ mm, $L_2 = 6$ mm, $d = 1.5$ mm, and $D = 4.5$ mm.

3.5 Conclusions and Future Work

In this research, a finite element model based injection nozzles geometric design is developed to optimize the laser energy efficiency and powder catchment efficiency in the DMD additive manufacturing process of Ti-6Al-4V. A neural network was developed to confront the problems of having a great amount of alternative designs and a considerable amount of calculation time. The suitable process parameters are applied based on simulations, and the synergetic effects of the nozzle geometric parameters on the two design objectives are investigated and analyzed. It is found that the bottom section of the nozzle has little effect on the laser energy efficiency, and a large slope angle is preferred. It is also found that the powder catchment efficiency decreases with the bottom section of the nozzle, and a small slope angle is preferred. In order to combine the two objectives, we define the process efficiency as the product of the two objective function outputs. Using this definition, the final designs are obtained, having a maximum laser energy efficiency and a powder catchment efficiency higher than 90%. The final design is driven by both design objectives: the objective function for laser energy efficiency has the dominant effect on L_2, while the objective function for powder catchment efficiency has the dominant effect on d, and D is driven by both objective functions. A couple of feasible designs exist. If other manufacturing constraints are not considered, one of the designs can be: L_1 = 0 mm, L_2 = 6 mm, d = 1.5 mm, and D = 4.5 mm. Some prescribed constants include: a 10 mm gap distance from nozzle tip to the substrate, a 20 mm length for the top section (L_3) of the injection nozzle, a 1 m/s inlet gas mean velocity, and a powder feed rate of 1.5 g/min.

Future work should involve the printing of multiple layers, modeling the melt pool shape considering mass addition and driving forces for melt pool convection. Multiple injection nozzles should be implemented to calculate the coaxial or non-coaxial nozzle based powder catchment efficiency, the laser attenuation level and thus the laser energy efficiency. Last but most significant, experimental results should be shown in the future to validate and assess the results from modeling, and further improve the DMD process.

CHAPTER FOUR

A MATHEMATICAL MODEL-BASED OPTIMIZATION METHOD FOR DMD OF MULTI-MATERIALS

4.1 Introduction

In this work we employ a multi-objective optimization algorithm based on the modeling of the DMD of multiple materials to optimize the fabrication process. The optimization methodology is applied to the deposition of Inconel 718 and Ti-6Al-4V powders with prescribed powder feed rates, which is also applicable to other materials. Eight design variables are accounted in the example, including the injection angles, injection velocities, and injection nozzle diameters for the two materials, as well as the laser power and the scanning speed. The multi-objective optimization considers that the laser energy consumption and the powder waste during the fabrication process should be minimized. The optimization software modeFRONTIER® is used to drive the computation procedure with a MATLAB code. The results show the design and objective spaces of the Pareto optimal solutions, and enable the users to select preferred setting configurations from the set of optimal solutions.

The approach proposed is applied to the DMD process, where multi-materials deposition is allowed. It is also applicable to any similar processes consisting of powders injected into a laser beam and a melt pool, such as in laser cladding, where typically just one material is added to the substrate [Han2004] [Wang2009] [Kamara2011]. To improve the DMD performance and better control the process, a number of papers have focused on the modeling of the coaxial powder flow [Wen2009] [Wen2011] [Balu2012], powder in-flight melting [Grujicic2001] [Liu2003] [Yan2015], melt pool temperature and geometry [Toyserkani2004] [Saedodin2010], and cladding height/profile [Han2004] [Kamara2011] [Urbanic2016]. The real-time closed loop control of the process has also been studied by a variety of researchers, e.g., [Mazumder2000] [Toyserkani2003] [Salehi2006] [Peyre2008] [Tang2011]. However, these models are based on the fabrication of homogeneous objects, i.e., deposition of a single kind of powder. Also, one disadvantage of real-time control is that time delay and perceptible perturbation exist, so it is not easy to achieve a desired stable material deposition rate.

The aim of this study is to propose a pre-process parameter optimization method, which serves as a first step toward creating an operation guide for the fabrication of heterogeneous objects using the DMD process. The optimization algorithm is based on the modeling of the whole process under constraints on the deposition of multiple materials, regarding powder and substrate phase changes, powder utilization, and laser energy consumption. The models are firstly formulated in Section 4.2. Then, in Section 4.3, the optimization procedure with the modeFRONTIER® software is presented. In

Section 4.4, a case study for mixing Inconel 718 and Ti-6Al-4V powders is provided to illustrate the proposed method, and the results and decision making process based on the optimization results are discussed. Finally, conclusions and future work are outlined in Section 4.5.

4.2 Model Formulation

The schematic of a modifiable coaxial DMD work space is shown in Fig. 4.1 (cross-sectional view). The DMD free form fabrication process consists of a continuous wave laser inducing a melt pool on the substrate, and nozzles injecting different types of powders (material 1 and material 2) from two opposite nozzles into the melt pool in an inert environment. Inert gas such as argon is used as the delivering gas. A deposited layer consisting of two materials forms as the melt pool cools down and solidifies. The mathematical models in this study are mainly based on the schematic shown in Fig. 4.1. Note that, in most DMD implementations, four nozzles are used instead of two. The models based on a four-nozzle configuration can be easily modified from the models based on the schematic in Fig. 4.1, so this study only focuses on the two-nozzle configuration.

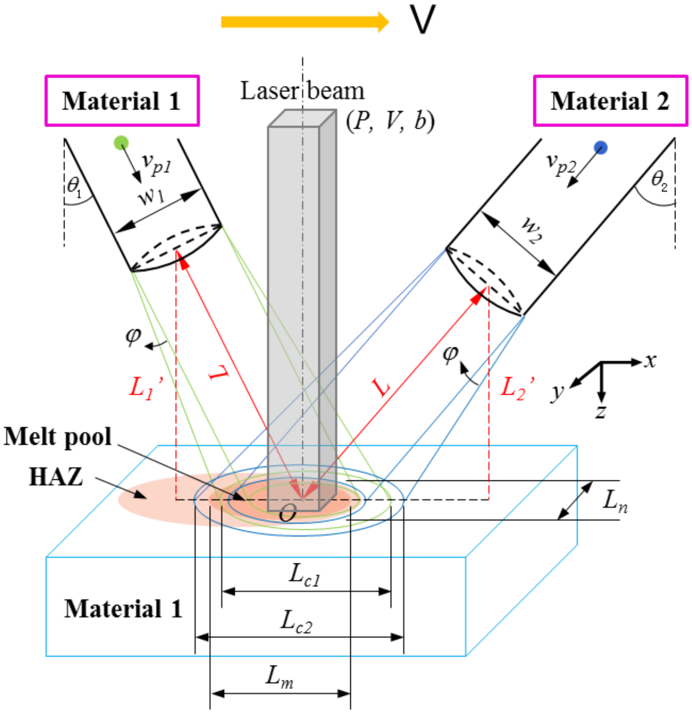

Fig. 4.1 The schematic of the modifiable coaxial DMD process.

The laser spot shape is assumed to be square with a width *2b* in this study. Square laser is the basic 3D model for moving substrate heating, circular or other shape laser beam would require a new more computing intensive model derivation. The laser beam, which has a power *P*, is scanning at a speed *V* on the substrate. Two types of powders are delivered from two different nozzles simultaneously, with the nozzle diameters w_1 *and* w_2, *and* injection angles θ_1 and θ_2. The particle velocities are v_{p1} and v_{p2} respectively. The shape of the powder jets is approximated as conical, with a gradually increasing outer diameter from the nozzle tip to the substrate due to the decrease of pressure. The resulting divergence angles are denoted as φ. The nozzles' centerlines are always pointing to the center of the laser spot, and the distance from the center of the spot to the center of the nozzle orifice is kept at L. Laser power, laser scanning speed, injection angles, injection velocities, nozzle diameters, and powders feed rates are the important process parameters, all of which are the design variables that need to be tailored to meet the designed part material variation during the pre-process stage.

The models are based on the following main assumptions: (1) the laser is top-hat with a uniform energy distribution; (2) the particles have the same size, perfectly spherical and absorb energy uniformly; (3) the particles are evenly distributed inside the powder jets with constant divergence angles; (4) the particles' velocities are unchangeable during the flight, and the relative velocity between particles and the feed gas is also constant; (5) particle collisions are neglected; (6) the heat transfer between the particles and the substrate is neglected; and (7) thermal properties (density, thermal conductivity, and heat capacity) are constant for each material.

4.2.1 Particle Heating

Particles are heated by the laser beam during the flight. The occurrence of phase change depends on particle properties and laser intensity. Complete melting of a particle is a requirement and an indication of good mixing between the different build materials.

To guarantee the complete melting of a particle before it finally solidifies within the melt pool, the particle needs to be melted either during the flight or in the melt pool. However, it has been demonstrated that a particle's melting inside a pool with constant melting temperature is instantaneous [Chande1985] [Qi2006]. Therefore, in this study, particles in-flight melting is not considered as a necessary condition for good mixing, as long as the particles can be melted in the melt pool.

Note that if a particle's temperature exceeds its boiling point during the flight, metal vapor is formed as well as possible plasma. The vapor and/or plasma can effectively absorb laser energy and impede the process [Vetter1993] [Antipas2015] [Luo2015]. Therefore, a constraint needs to be imposed on the process to ensure there is no inflight boiling. The governing equation for the in-flight heating of a single particle is as follows.

$$m_p c_{pp} \frac{\mathrm{d}T_p}{\mathrm{d}t} = \eta I \frac{S_p}{4} - h_p S_p \left(T_p - T_\infty\right) - E_p \sigma S_p \left(T_p^4 - T_\infty^4\right) - \delta_1 L_f \frac{\mathrm{d}m_p}{\mathrm{d}t} - \delta_2 L_v \frac{\mathrm{d}m_p}{\mathrm{d}t} \quad (4.1)$$

$$\delta_1 = \begin{cases} 0, \ T_p \le T_{sol} \ or \ T_p \ge T_{liq} \\ 1, \ T_{sol} < T_p < T_{liq} \end{cases} \ and \ \delta_2 = \begin{cases} 0, \ T_p < T_{boil} \\ 1, \ T_p \ge T_{boil} \end{cases} \quad (4.2)$$

where m_p, c_{pp}, and S_p are the mass, specific heat, and surface area of a particle; T_p and T_∞ are the temperatures of the particle and the surroundings respectively; I is the laser intensity (W/m^2), and η is the laser absorptivity of the particle; E_p is the surface emissivity of the powder; σ is the Stefan-Boltzmann constant (5.67×10^{-8} W/(m$^2\cdot$K^4)); L_f

and L_v are the latent heat of fusion and the latent heat of vaporization for the particle material; T_{sol}, T_{liq} and T_{boil} are solidus, liquidus, and boiling temperatures of the particle material respectively; h_p is the convective heat transfer coefficient, which can be determined from the Nusselt number (Nu) [Ranz1952] [Gu2004]:

$$h_p = \frac{Nuk_g}{d_p} = \frac{k_g\left(2 + 0.6Re^{\frac{1}{2}}Pr^{\frac{1}{3}}\right)}{d_p} \tag{4.3}$$

$$Re = \frac{\rho_g d_p \left| v_g - v \right|_l}{\mu_g} \tag{4.4}$$

where d_p is the particle diameter; k_g is the thermal conductivity of the surrounding feed gas; Re is the Reynolds number; ρ_g, v_g, v_p, and μ_g are the density and velocity of the feed gas, the velocity of the particle, and the dynamic viscosity of the feed gas respectively; and Pr is the Prandtl number. It should be noted here that for pure material (not a mixture such as an alloy), the solidus and liquidus temperatures are replaced by a single melting temperature T_{melt}. Thus, Eq. (4.2) becomes:

$$\delta_1 = \begin{cases} 0, & T_p < T_{melt} \; or \; T_p > T_{melt} \\ 1, & T_p = T_{melt} \end{cases} \quad and \quad \delta_2 = \begin{cases} 0, & T_p < T_{boil} \\ 1, & T_p \geq T_{boil} \end{cases} \tag{4.5}$$

Following [Wen2009] [Yan2014] [Yan2015], neglecting the radiation term and modifying the solution according to Eq. (4.1), the laser-particle interaction time needed to start vaporizing a particle can be determined as follows.

$$t_{boil} = -\frac{1}{B}\ln\left(\frac{T_{sol} - A}{T_\infty - A}\right) - \frac{1}{C}\ln\left(\frac{T_{liq} - A}{T_{sol} - A}\right) - \frac{1}{B}\ln\left(\frac{T_{boil} - A}{T_{liq} - A}\right) \tag{4.6}$$

where $A = T_\infty + \frac{\eta I}{4h_p}$, $B = \frac{h_p S_p}{m_p c_{pp}}$, and $C = \frac{h_p S_p}{m_p c_{pp} + \frac{m_p L_f}{T_{liq} - T_{sol}}}$. For pure material, the solution becomes:

$$t_{boil} = -\frac{1}{B}\ln\left(\frac{T_m - A}{T_\infty - A}\right) - \frac{1}{B}\ln\left(\frac{T_{boil} - A}{T_m - A}\right) \tag{4.7}$$

With this model, the phase of a particle is predictable as time evolves. The adjustable process parameters can be tailored to prevent the boiling of particles, i.e., the particle in-flight heating time should be kept below t_{boil}.

4.2.2 Material Mixing by Melt Pool Convection

A particle can be better mixed with the substrate material if it is melted during the flight. Moreover, the mixing effect could be more efficient if the melt pool has a large convection. The passive mixing of dissimilar materials in the melt pool is an important step of mixing and, since it is passive and instability-driven, unavoidable. However, the passive mixing can be controlled by varying the process parameters. A full mixing of different materials can result in smooth transitions between different materials while avoiding critical crack and porosity, which is beneficial to the mechanical properties of a heterogeneous object or FGM.

Among the mixing strategies, the role of fluid mechanics instability is critical and represents the sole passive physical mechanism that drives the mixing process. There are four main instabilities that control the mixing in the melt pool: (1) Marangoni instabilities driven by surface tension differentials, (2) the Rayleigh-Taylor instability between fluids of different densities driven by buoyancy effects, (3) the convective Rayleigh-Bénard instability due to temperature gradients between the top and the bottom of the melt pool and driven by thermocapillary effects, and (4) the Kelvin-Helmholtz instability due to differential velocities of the injected particles. These instabilities are not independent, but actually interweaved with each other. The first and second driven factors are the main driving forces, and therefore they are considered in the simulation.

Before looking at the melt pool mixing, the free surface evolution should be modeled in order to track the formation of clad shape. A static model is used to simulate the boundary layer movement with mass addition. In this model, the geometry of the deposited layer is explicitly described using an Arbitrary Lagrangian-Eulerian (ALE) moving mesh, which takes into account mass addition, melting and solidification phase changes, surface tension and Marangoni effect. The liquid phase is assumed to be incompressible Newtonian laminar flow. The governing equations include mass conservation, momentum conservation and energy conservation equations:

$$\rho_l \nabla \vec{u} = 0 \tag{4.8}$$

$$\rho_l c_p \left[\frac{\partial \vec{u}}{\partial t} + \nabla \cdot \left(\vec{u} - \vec{u}_m \right) \vec{u} \right] = \nabla \cdot \left[-pI + \mu \left(\nabla \vec{u} + \left(\nabla \vec{u} \right)^T \right) \right] + \vec{F}_{buoyance} + \tag{4.9}$$

$$\rho c_p \left[\frac{\partial T}{\partial t} + \left(\vec{u} - \vec{u}_m \right) \cdot \nabla \ T \right] = \nabla \cdot \left(k \nabla \ T \right) + \dot{\ } \tag{4.10}$$

where ρ_l is the density of liquid (melted substrate), c_p is the equivalent heat capacity due to two phases, $\vec{u}_m$ is mesh velocity, $\overrightarrow{F}_{buoyance}$ is the buoyance force and $\overrightarrow{F}_{Darcy}$ the Darcian term when fluid goes through the porous media (the schematic of the microstructure in the mushy zone can be seen in Fig. 4.2).

The boundary conditions for the calculation domain is:

On surface:

Heat transfer: $$k \cdot \nabla T \cdot \vec{n} = I - h_a \left(T - T_\infty \right) - \varepsilon \sigma \left(T^4 - T_\infty^4 \right) - \rho c_p \overrightarrow{V_p} \cdot \vec{n} \left(T - T_p \right) \tag{4.11}$$

Fluid: $$\vec{\sigma}_n = -\kappa \sigma \cdot \vec{n} \tag{4.11}$$

$$\vec{\sigma}_t = \frac{\partial \sigma}{\partial T} \nabla T \cdot \vec{t} \tag{4.12}$$

On other edges:

Heat transfer: $$k \cdot \nabla T \cdot \vec{n} = -h_a \left(T - T_\infty \right) - \varepsilon \sigma \left(T^4 - T_\infty^4 \right) \tag{4.13}$$

Fluid: $$\vec{u} = 0 \tag{4.14}$$

where κ is curvature, and σ is surface tension. $\overrightarrow{V_p}$ is the top boundary moving velocity, which is defined and modified from:

$$\overrightarrow{V_p} = N_p \frac{\eta_p D_m}{\rho_l \pi r_p^2} exp\left(-N_p \frac{\left(x - V_s t \right)^2}{r_p^2} \right) \cdot \vec{j} \tag{4.15}$$

following [Morville2012b] for the 2D case, where N_p is the constriction coefficient, r_p the standard deviation of the Gaussian distribution, η_p the powder catchment efficiency. The powder distribution in Eq. (4.15) basically follows a Gaussian distribution and it can be modified based on the solution of powder distribution. The liquid phase is typically modeled as laminar flow, although it has also been simulated as turbulent flow due to a different view of the melt pool in the welding realm [Choo1994] [Yang2000b] [Chakraborty2004].

A typical 2D simulation carried out in COMSOL is presented in Fig. 4.2. The substrate material thermal properties are modified based on its composition. The clad is built up on the substrate, and the black curve denotes the isotherm temperature of the melting point of the substrate. The velocity field in liquid phase is marked by arrows whose length and direction imply the velocity magnitude and moving direction. Basically, the fluid in the melt pool moves away from the center of the beam spot on the surface and then moves down and back up inside the melt pool, forming a Marangoni flow. This is because the main driving force in the melt pool is the thermocapillary force and the shear force is proportional to the thermocapillary force due to the temperature gradient, which can be seen from Eq. (4.12). It can be seen from Fig. 4.2 that the melt pool convection velocity is in the order of 0.1 m/s, and the melt pool size is around 3 mm. Therefore, the melt pool convection should be sufficient for a good mixing.

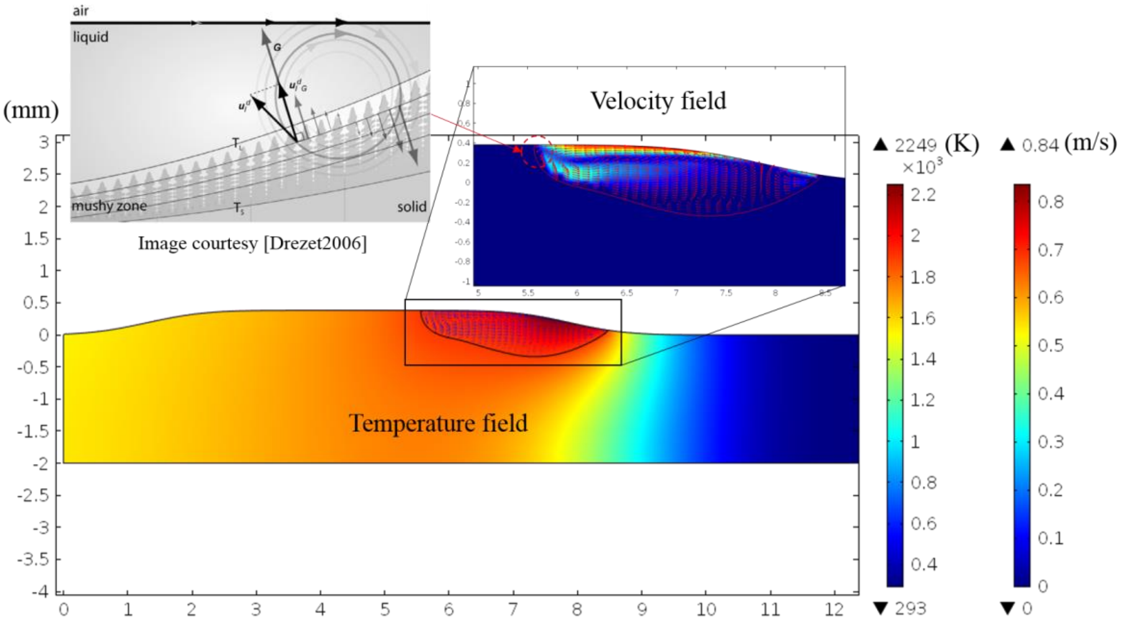

Fig. 4.2 A typical simulation result for the clad formation and melt pool convection.

4.2.3 Laser Attenuation

The laser intensity is attenuated during the fabrication process due to the shadowing effect of the powder jets. In this study, the laser attenuation model will be built based on a detailed mathematical/analytical model. The attenuated laser intensity, rather than the original laser intensity, should be considered as the input heat source on the surface of the substrate. In general, the Beer-Lambert law has been widely adopted to calculate the attenuation [Han2004] [Jouvard1997] [Lin2000] [Pinkerton2007] [Zhou2009] [Tabernero2012]. The Beer-Lambert law takes the form:

$$I = I_0 e^{-\varepsilon C(z)} \qquad (4.16)$$

and $(1-e^{-\varepsilon C(z)z})$ is the attenuation, where I is the attenuated laser intensity, I_0 is the original laser intensity, $C(z)$ is the particle density/concentration as a function of z coordinate, and $\varepsilon = \dfrac{3(1-\eta)}{2r_p\rho_p}$ is the molar absorptivity or extinction coefficient (m^2/kg).

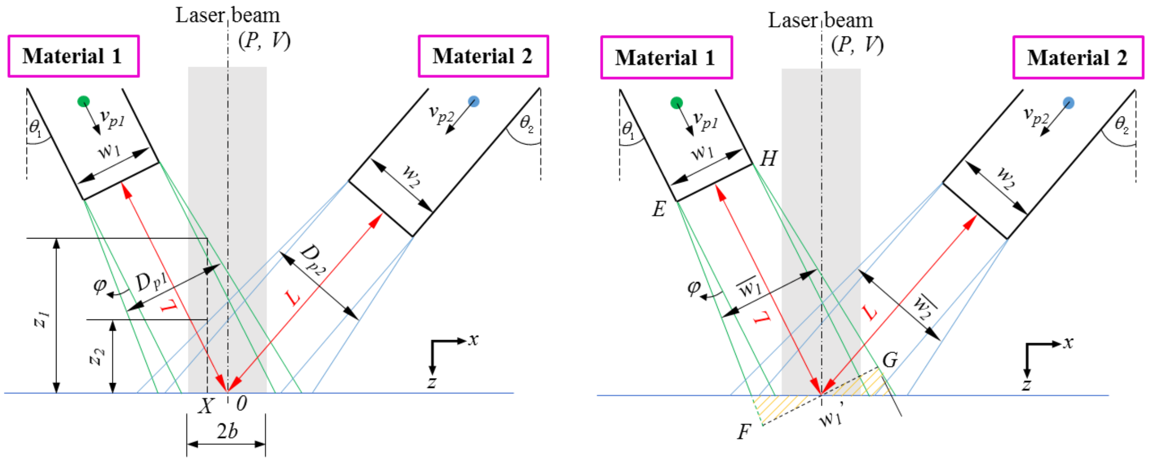

Fig. 4.3 The cross-sectional view of the working space.

The term $C(z)$ can be varied spatially due to the overlapping of the powder streams, and consequently the attenuation varies spatially. Since full consideration of attenuation is complicated, existing simplified models are based on shadowing while ignoring the effect of beam divergence [Fu2002] [Huang2005] [Liu2005]. In other research, the attenuation is calculated in a layer by layer manner, either analytically [Qi2006] [He2007] or numerically [Tabernero2012]. For the models cited, the attenuation is calculated based on the symmetric nozzles configuration, and none of the current available models accounts for multi-materials with asymmetric nozzles. In addition, the three-dimensional features of powder streams are not fully considered as the laser beam intersects their trajectories.

Following our previous work, the attenuated laser intensity I can be calculated using a superposition method [Yan2014] [Yan2015], i.e., the total attenuation is seen as the sum of the attenuations for the laser beam to traverse each of the powder streams. For example, in the cross-sectional view shown in Fig. 4.3 (a), the slice of laser beam pointing at position (x, 0, 0) is attenuated by a layer of particle cloud with thickness z_1 (material 1) and a layer of particle cloud with thickness z_2 (material 2). On the x-y substrate plane, the attenuation varies within the laser spot region, so the attenuation should be treated as a function of x and y coordinates:

$$I(x,y)=I_0\exp\left[-\varepsilon_1 C_1|z_1|\right]\exp\left[-\varepsilon_2 C_2|z_2|\right] \tag{4.17}$$

where C_1 and C_2 are the powder concentrations in the two powder streams that the laser traverses. The powder concentrations can be expressed as:

$$C_i=\frac{M_{pi}}{\pi\left(\frac{D_{pi}(z)}{2}\right)^2 v_{pi}} \tag{4.18}$$

where $M_{pi}(i=1,2)$ are the powders feed rates, $D_{pi}(i=1,2)$ are the cross-sectional diameters of the cone-shaped powder jets as a function of the z coordinate due to the divergence angle. Since the D_{pi} are gradient variables along the L direction, they are replaced by their average values $\overline{w_i}\left(i=1,2\right)$, which is equal to the median of the Trapezoid EFGH, marked in Fig. 4.3 (b). Thus,

$$C_i = \frac{M_{pi}}{\pi\left(\frac{\overline{w_i}}{2}\right)^2 v_{pi}} = \frac{M_{pi}}{\pi\left(\frac{w_i + L\tan\varphi}{2}\right)^2 v_{pi}} \tag{4.19}$$

In Eq. (4.17), $|z_1|$ and $|z_2|$ are both functions of the *x* and *y* coordinates, and they can be determined by solving the simultaneous equations of the powder jet cone surface and the plane surface of *x* = *X* (-b < *X* < b is a specific value on the *x*-axis) to get the intersection line equation.

The schematic based on which the intersection line equation is deduced is illustrated in Fig. 4.4. According to the geometric relationship, the cone surface equation in the *x*'-*y*'-*z*' coordinates is:

$$\frac{x'^2}{a^2} + \frac{y'^2}{a^2} - \frac{\left(z' + L + \frac{w_1}{2\tan\varphi}\right)^2}{b^2} = 0 \tag{4.20}$$

The *x*-*y*-*z* coordinate can be seen as the *x*'-*y*'-*z*' coordinate rotated by an angle θ_1 about the *y*' axis in clockwise direction:

$$\begin{bmatrix} x \\ y \\ z \end{bmatrix} = \begin{bmatrix} \cos\theta_1 & 0 & \sin\theta_1 \\ 0 & 1 & 0 \\ -\sin\theta_1 & 0 & \cos\theta_1 \end{bmatrix} \begin{bmatrix} x' \\ y' \\ z' \end{bmatrix}, \text{ so } \begin{bmatrix} x' \\ y' \\ z' \end{bmatrix} = \begin{bmatrix} \cos\theta_1 & 0 & -\sin\theta_1 \\ 0 & 1 & 0 \\ \sin\theta_1 & 0 & \cos\theta_1 \end{bmatrix} \begin{bmatrix} x \\ y \\ z \end{bmatrix} \tag{4.21}$$

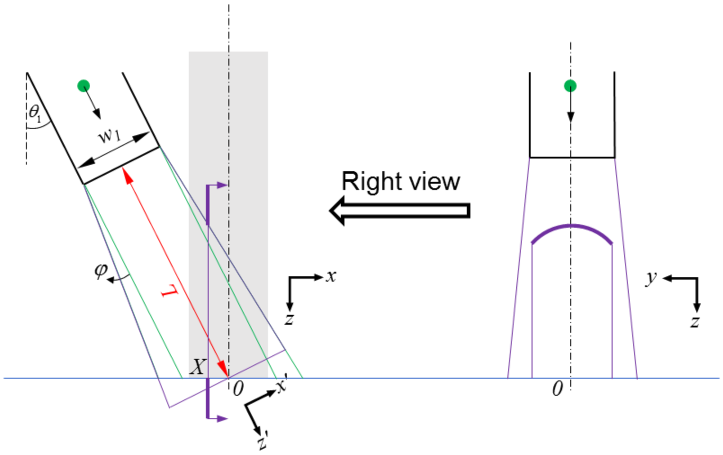

Fig. 4.4 Illustration of the intersection line between the laser beam and the powder jet.

Substituting the relationship above into Eq. (4.20), the cone surface equation in the *x*'-*y*'-*z*' coordinate becomes:

$$\frac{(x\cos\theta - z\sin\theta)^2}{a^2} + \frac{y^2}{a^2} - \frac{\left(x\sin\theta + z\cos\theta + L + \frac{w_1}{2\tan\varphi}\right)^2}{b^2} = 0 \qquad (4.22)$$

Since $\frac{a^2}{b^2} = (\tan\varphi)^2$, Eq. (22) can be finally written as:

$$\frac{(x\cos\theta - z\sin\theta)^2}{(\tan\varphi)^2} + \frac{y^2}{(\tan\varphi)^2} = \left(x\sin\theta + z\cos\theta + L + \frac{w_1}{2\tan\varphi}\right)^2 \qquad (4.23)$$

$$\text{with } -b \le x \le b, -b \le y \le b$$

The laser penetration depth $|z_1|$ in the particle cloud of material 1 at any point (*x*, *y*) on the substrate plane can be solved from Eq. (4.23) by taking the absolute value of the negative solution. Similarly, the laser penetration depth $|z_2|$ in the particle cloud of material 2 can be solved from:

$$\frac{(x\cos\theta + z\sin\theta)^2}{(\tan\varphi)^2} + \frac{y^2}{(\tan\varphi)^2} = \left(-x\sin\theta + z\cos\theta + L + \frac{w_2}{2\tan\varphi}\right)^2 \tag{4.24}$$

$$\text{with } -b \le x \le b, -b \le y \le b$$

Summarizing the equations above, we get the final expression for the attenuated laser intensity:

$$I(x,y) = I_0 \cdot \exp\left[-\frac{3(1-\eta)}{2r_p\rho_{p1}} \frac{M_{p1}}{\pi\left(\frac{w_1 + Ltan\varphi}{2}\right)^2 v_{p1}} |z_1|\right] \cdot \exp\left[-\frac{3(1-\eta)}{2r_p\rho_{p2}} \frac{M_{p2}}{\pi\left(\frac{w_2 + Ltan\varphi}{2}\right)^2 v_{p2}} |z_2|\right] \tag{4.25}$$

where $|z_1|$ and $|z_2|$ should be solved from Eq.s (4.23) and (4.24) respectively. Then, by discretizing the laser spot region, the final attenuated laser intensity is calculated as an average value in this study.

$$I = \frac{\sum_{x=1}^{i}\sum_{y=1}^{j} I(x,y)}{i \times j} \tag{4.26}$$

4.2.4 Substrate Heating

In order to characterize the powder waste and laser energy consumption, the substrate heating process is the critical step. It determines both objectives: the powder waste and the laser energy consumption.

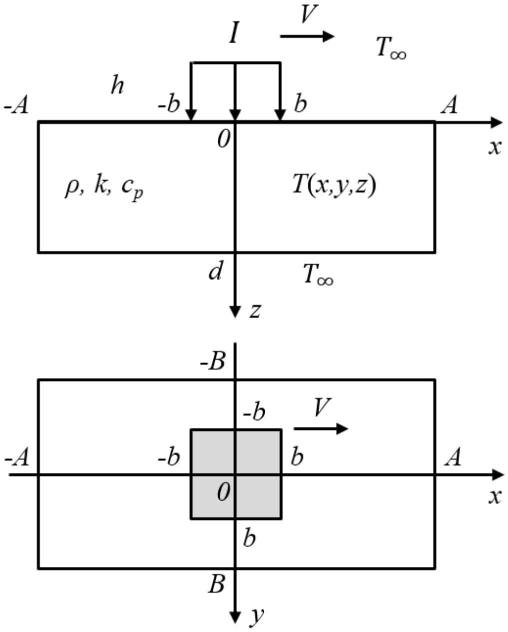

Fig. 4.5 Schematic for the substrate heating model.

To facilitate the design process and provide a stable output, boundary conditions and the analytical solution are provided to compute the three-dimensional temperature field in the substrate [Osman2009]. As shown in Fig. 4.5, the moving heat source equation governs the heating process:

$$\frac{\partial^2 T_s}{\partial x^2}+\frac{\partial^2 T_s}{\partial y^2}+\frac{\partial^2 T_s}{\partial z^2}-\frac{V}{\alpha}\frac{\partial T_s}{\partial x}=0 \tag{4.27}$$

Where T_s represents the substrate temperature; α is the thermal diffusivity of the substrate. The boundary conditions regarding a continuously moving laser/substrate are:

$$\left(T_s\right)_{x=-A}=\left(T_s\right)_{x=A} \tag{4.28}$$

$$\left(\frac{\partial T_s}{\partial x}\right)_{x=-A} = \left(\frac{\partial T_s}{\partial x}\right)_{x=A} \tag{4.29}$$

$$\left(\frac{\partial T_s}{\partial y}\right)_{y=0} = 0 \tag{4.30}$$

$$\left(\frac{\partial T_s}{\partial y}\right)_{y=B} = \left(\frac{\partial T_s}{\partial y}\right)_{y=-B} = 0 \tag{4.31}$$

$$-k_s\left(\frac{\partial T_s}{\partial z}\right)_{z=0} = \begin{cases} I_{att}, x < 0 \\ h_s\left[T_\infty - \left(T_s\right)_{z=0}\right],\ x \geq \end{cases} \tag{4.32}$$

$$\left(T_s\right)_{z<0} = \left(T\right)_{z=d} = T_\infty \tag{4.33}$$

In Eq. (4.32), h_s represents the effective forced convective heat transfer coefficient on the substrate surface, which combines both convection and radiation effects [Goldak1984]:

$$h_s = 2.4 \times 10^{-3} E_s T_s^{1.6} \tag{4.34}$$

where E_s denotes the surface emissivity of the substrate; The analytical solution is given as:

$$\begin{aligned} T(x,y,z) = T_\infty + I_{att}\frac{b^2(d-z)}{AB(hd+k)} + 2\sum_{m=1}^{\infty}\Re_e\left\{\tilde{T}_{m0}e^{\frac{jm\pi x}{A}}\right\} + 2\sum_{n=1}^{\infty}\tilde{T}_{0n}\cos\left(\frac{n\pi y}{B}\right) \\ + 4\sum_{n=1}^{\infty}\left[\cos\left(\frac{n\pi y}{B}\right)\sum_{m=1}^{\infty}\Re_e\left\{\tilde{T}_{mn}e^{jm\pi x/A}\right\}\right] \end{aligned} \tag{4.35}$$

$$\tilde{T}_{mn} = \frac{I_{att\,mn}\mathrm{sh}\left[\gamma_{mn}(d-z)\right]}{h\,\mathrm{sh}(\gamma_{mn}d) + k\gamma_{mn}\mathrm{ch}(\gamma_{mn}d)} \tag{4.36}$$

$$\gamma_{mn} = \left[\left(\frac{m\pi}{A}\right)^2 + \left(\frac{n\pi}{B}\right)^2 - i\left(\frac{m\pi}{A}\right)\frac{V}{\alpha}\right]^{\frac{1}{2}} \tag{4.37}$$

$$I_{att_{mn}} = I_{att} \frac{\sin\left(m\pi b / A\right)\sin\left(n\pi b / B\right)/}{\left(m\pi\right)\left(n\pi\right)} = \begin{cases} \frac{b}{A}\frac{\sin\left(\frac{n\pi b}{B}\right)}{n\pi}, when\, m = \\ \frac{b}{B}\frac{\sin\left(\frac{m\pi b}{A}\right)}{m\pi}, when\, n = \end{cases} \qquad (4.38)$$

4.3 Optimization Methodology

Our goal is to fabricate heterogeneous objects by mixing different powders. In order to make the best use of powders and to minimize the laser energy consumption for depositing a certain quantity of materials in a given time frame while achieving full melt and mixing of different particles, we aim at optimizing the process parameters in the DMD process. Generally, the powder waste is the ratio of the amount of powder actually used for deposition (powder dropped into the melt pool) to the total amount of powder used. The laser energy consumption is defined as the laser power divided by the laser scanning speed. Similar terms have been used as different names in literature, such as the specific energy $E_{specific} = \frac{P}{V \cdot D}$ [Valsecchi2012] or linear heat input $E_{linear} = \frac{P}{V}$ [Heigel2015]. Two types of powders are injected from two nozzles.

Table 4.1 Critical process parameters and/or their possible ranges.

Parameter	Value
Laser parameters	
Laser power, P (W)	120-1000 (step 10)
Laser scanning speed, V (mm/s)	5-60 (step 5)
Laser spot width, $2b$ (μm)	600
Powder parameters	
Powder velocities, v_{pi} (m/s)	1-51 (step 5)
Divergence angles, φ_i (°)	5
Powder feed rates, M_{pi} (g/min)	20 (changeable in future)
Particle radius, r_p (μm)	10
Nozzle parameters	
Injection angles, θ_i (°)	15-75 (step 5)
Nozzle diameters, w_i (mm)	0.5-1.5 (step 0.1)
Nozzle – spot center distance, L (mm)	9.5

The laser power (P), laser scanning speed (V), particle velocities (v_{pi}), injection angles (θ_i), and nozzle diameters (w_i) in the following optimization example are the design parameters and their possible ranges are specified according to the DMD equipment Optomec® MR-7 (Optomec® Inc., Albuquerque, NM) with a few minor modifications. All the critical process parameters and/or their possible ranges are classified into laser parameters, powder parameters, and nozzle parameters. The available values are scattered by the step values shown in Table 4.1. Specifically, the powder feed rates are supposed to be spatially changeable according to the design of the heterogeneous part. However, they are set at constant 20 g/min in this study for one specific location.

In the following case study, Inconel 718 and Ti-6Al-4V are used as the build materials. Heterogeneous parts, especially functionally graded parts made of Inconel 718 nickel alloy and Ti-6Al-4V titanium alloy are specially employed in aerospace applications because of their superior corrosion resistance and mechanical properties [Chen2011]. Titanium and nickel graded alloys are also used for medical applications because of their good biocompatibility [Watari2004] [Lahoz2004]. The physical and thermal properties of the two materials are listed in Table 4.2 [Chen2011] [Ross1992] [Boivineau2006] [David2008].

Table 4.2 Physical and thermal properties of Inconel 718 and Ti-6Al-4V.

Properties	Inconel 718	Ti-6Al-4V
Laser absorptivity, η	0.3	0.3
Density, ρ (kg/m^3)	8190	4420
Specific heat, c_{pp} (J/kg/K)	435	610
Thermal conductivity, k_p (W/m/K)	21.3	17.5
Latent heat of fusion, L_f (kJ/kg)	272	290
Latent heat of vaporization, L_v (kJ/kg)	5862	9460
Boiling point, T_{boil} (K)	3190	3315
Solidus temperature, T_{sol} (K)	1533	1878
Liquidus temperature, T_{liq} (K)	1609	1928

We assume that the laser beam is moving from the left to the right of the substrate. Suppose that in Fig. 4.1, the Material 1 from left nozzle is Inconel 718 and the Material 2 from the right nozzle is Ti-6Al-4V, and the substrate is composed of only Inconel 718.

The rectangular laser beam heats the substrate and generates an HAZ (Heat Affected Zone). Within the HAZ, the melt pool forms with a boundary profile at the isotherm of the substrate melting temperature (1609 K). The contact length between the powder jets and the substrate in *x*-direction is denoted by L_{c1} and L_{c2} respectively. The maximum widths of the melt pool in the *x* and *y* directions are denoted by L_m and L_n respectively. With this, the powder waste can be determined by calculating the portion of powders that land outside the melt pool. However, since the melt pool is not a regular ellipse from the analytical solution in Section 4.2.4, the exact amount/ratio of the powder waste is difficult to determine. Under a certain laser scanning speed, the widths of the melt pool in two directions increase simultaneously with the laser intensity. Based on this fact, we characterize the powder waste using the differences between the contact lengths and the melt pool width in the *x*-direction (or *y*-direction), instead of calculating the area differences between the powder jet – substrate contact regions and the melt pool region. According to Fig. 4.1, the powder waste in mm is represented by:

$$PowderWaste = L_{c1} + L_{c2} - 2L_m \tag{4.39}$$

where $L_{ci}\left(i=1,2\right)$ represent the contact length and can be derived from geometric relationships according to Fig. 4.1:

$$L_{ci} = \frac{w_i}{\cos\theta_i} + \left(L_i + w_i\sin\theta_i\right)\tan\left(\theta_i + \phi\right) - w_i\sin\theta_i\tan\theta_i - L_i\tan\left(\theta_i'\right) \tag{4.40}$$

The other optimization objective is the laser energy consumption:

$$Laser\ Energy\ Consumption = \frac{P}{V} \tag{4.41}$$

The optimization process is as follows: the averaged laser attenuation is first calculated using Eq. (4.26) under tentative process parameters. Then the temperature distribution on the substrate can be calculated using Eq. (4.35), and the left and right bounds of the melt pool are determined by knowing the positions where the melting temperature of substrate is reached. Finally, the results are checked against the constraint functions. The particle traveling distance within the laser beam should not be too long to heat a particle above its boiling temperature:

$$\frac{2b}{v_{p_i}\sin\theta_i} \le t_{bo_i i} \tag{4.42}$$

where $\frac{2b}{\sin\theta_i}$ is the particle's longest traveling distance in laser beam, illustrated in Fig. 4.6 by dashed lines.

The substrate temperature should be kept above the two materials' maximum melting temperature to ensure fully melting and thus good mixing of the two powders, while keeping it lower than the two materials' minimum boiling temperature to prevent boiling of the substrate and powders. In addition, since powder is more costly than energy, the melt pool width is lower bounded by the laser spot diameter to eliminate the designs that exhibit a very high powder waste.

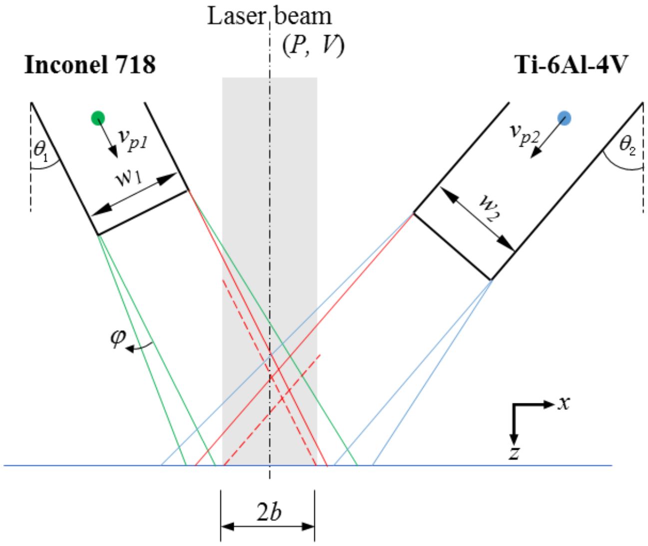

Fig. 4.6 Illustration of a particle's longest traveling distance in laser beam.

Using the conventional notation, the optimization problem can be stated as:

Minimize: Powder Waste, Laser Energy Consumption

Subject to: (a) $120 \text{ W} \leq P \leq 1000 \text{ W}$

(b) $5 \text{ mm/s} \leq V \leq 60 \text{ mm/s}$

(c) $1 \text{ mm/s} \leq v_{pi} \leq 51 \text{ mm/s}$

(d) $15° \leq \theta_i \leq 75°$

(e) $0.5 \text{ mm} \leq w_i \leq 1.5 \text{ mm}$

(f) $\dfrac{2b}{v_{pi} \sin \theta_i} \leq t_{boil_i}$

(g) $L_m \geq 2b$

(h) $\max (T_{melt\_1}, T_{melt\_2}) \leq T_{max} \leq \min (T_{boil\_1}, T_{boil\_2})$

Note that the laser spot width (2b), the divergence angle (φ), the feed rates of the two powders (M_{pi}), the particle radius (r_p), and the nozzle – spot center distance (L) are all set at the constant values shown in Table 4.1.

Design Variables. The ultimate design variables for the practical application are the following process parameters: the laser power P, the laser scanning speed V, the injection velocities v_{p1} and v_{p2}, the injection angles θ_1 and θ_2, and the nozzle diameters w_1 and w_2, in total 8 design variables.

Objective Functions. As discussed above, there are two objective functions: the powder waste and the laser energy consumption, both to be minimized:

Min. $PowderWaste = L_{c1} + L_{c2} - 2L_m$

and Min. $Laser\ Energy\ Consumption = \frac{P}{V}$

Computation using modeFRONTIER® with Matlab.

The bi-objective optimization problem is solved using the software modeFRONTIER®, which is a multi-objective and multi-disciplinary optimization platform. Due to the uncertainty of the fabrication process, and to reduce the calculation time, the 8 design variables are set at discrete values. The step change for each of the variables are defined in Table 4.1.

The Sobol space filter is based on a pseudo random Sobol sequence. It works best with 2 to 20 variables, and the experiments are uniformly distributed in the design space.

The Sobol method is used as the Design of Space (DOE) space filter, and the number of designs is set at 20. The MOGA-II scheduler is based on a Multi Objective Genetic Algorithm (MOGA) designed for fast Pareto convergence, and is selected as the optimizer. The number of generations is set at 100, with probabilities of directional cross-over, selection, and mutation set at default values, which are 0.5, 0.05 and 0.1 respectively. In real application, these numbers might be varied according to the apparatus and preference to balance the total calculation time and the number of feasible designs. For the 20×100 design scheduler, a fast convergence occurs after about 250 experiments (feasible designs emerge in large number) as can be seen from the design history table. Figure 6 shows the graphical flowchart implemented in modeFRONTIER$^{®}$.

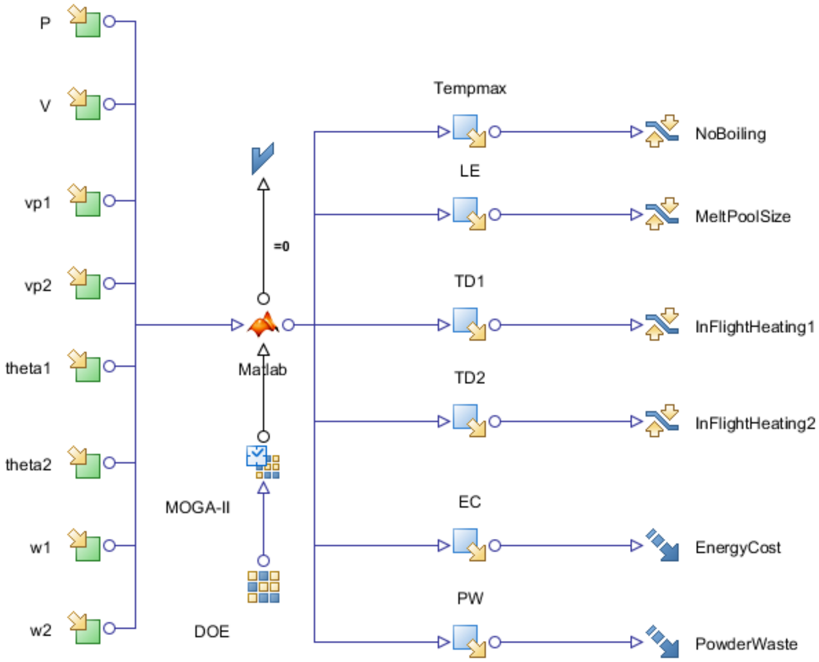

Fig. 4.7 Graphical optimization flow chart in modeFRONTIER$^{®}$.

4.4 Results and Discussion

Using the two materials' physical and thermal properties in Table 4.2, the resulting design space is created in Fig. 4.8. The feasible designs show a trade-off relationship between the two objective functions. The Pareto front solutions are marked with a green color. The two objective functions are conflicting with each other, since in order to reduce the powder waste, the nozzles should be more vertical (smaller injection angles), which results in a higher laser attenuation. As a consequence, the laser energy consumption would be larger. It can be seen from Fig. 4.8 that the laser energy consumption among the feasible designs ranges from about 5.5 kJ/m to 11 kJ/m. The powder waste among the feasible designs ranges from about 3 mm to 16 mm, but most designs are clustered at 3 mm to 8 mm.

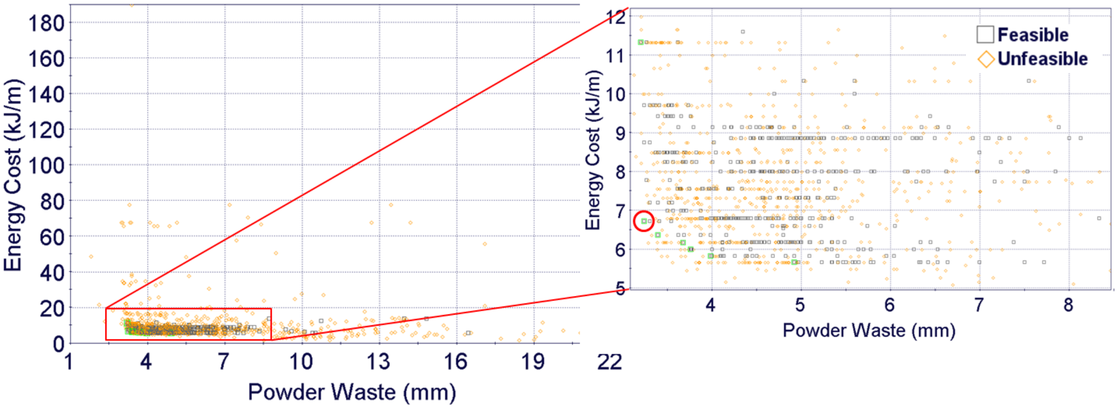

Fig. 4.8 Scatter of the designed two objective functions.

Comparing with the melt pool width L_m, which is around 0.6 mm from the design results, the values of the powder waste is high. This means that a great portion of powders land outside the melt pool according to our models and parameters settings. Therefore, the powder waste is seen as a more significant objective function in this study.

To better explain and learn from the optimization results, the design histories of the 8 design variables are shown in Fig. 4.9. The *x*-axis is the design ID, representing the generation evolution. The Genetic algorithm can quickly find the feasible range of the attenuated laser power by learning from the parental designs. The trends and/or convergence regions can be detected. For example, the laser power is initially searched between 120 W and 1000 W, and reaches a plateau after 200 designs. Finally it converges to the range between 300 W and 400 W (Fig. 4.9 (a)). The Pareto designs begin to emerge after about 1200 designs, resulting in a total of 14 Pareto designs after 100 generations or 2000 designs. Note that the number of Pareto designs is low because of the constraint on the melt pool width reduces the feasible design space. The laser scanning speed initially has an increasing trend, but it does not have a plateau. Instead, it stabilizes in the range of 30 mm/s to 60 mm/s, with Pareto designs of 30 mm/s, 55 mm/s and 60 mm/s. The particle velocities have similar trends but slightly different ranges: v_{p1} stabilizes between 20 – 45 m/s, while v_{p2} stabilizes between 25 – 40 m/s. The convergence and Pareto design distributions for the injection angles of the two powders are similar: both are finally in the range of 15° to 40°. The last couple of design variables are w1 and w2. Though the convergence of w_1 is faster than w_2, they finally rest also in a similar range: it is obvious that a 0.5 mm – 1 mm nozzle diameter is preferred. However, for w_1 almost all Pareto designs are at 0.5 mm, while the Pareto designs for w_2 are more scattered.

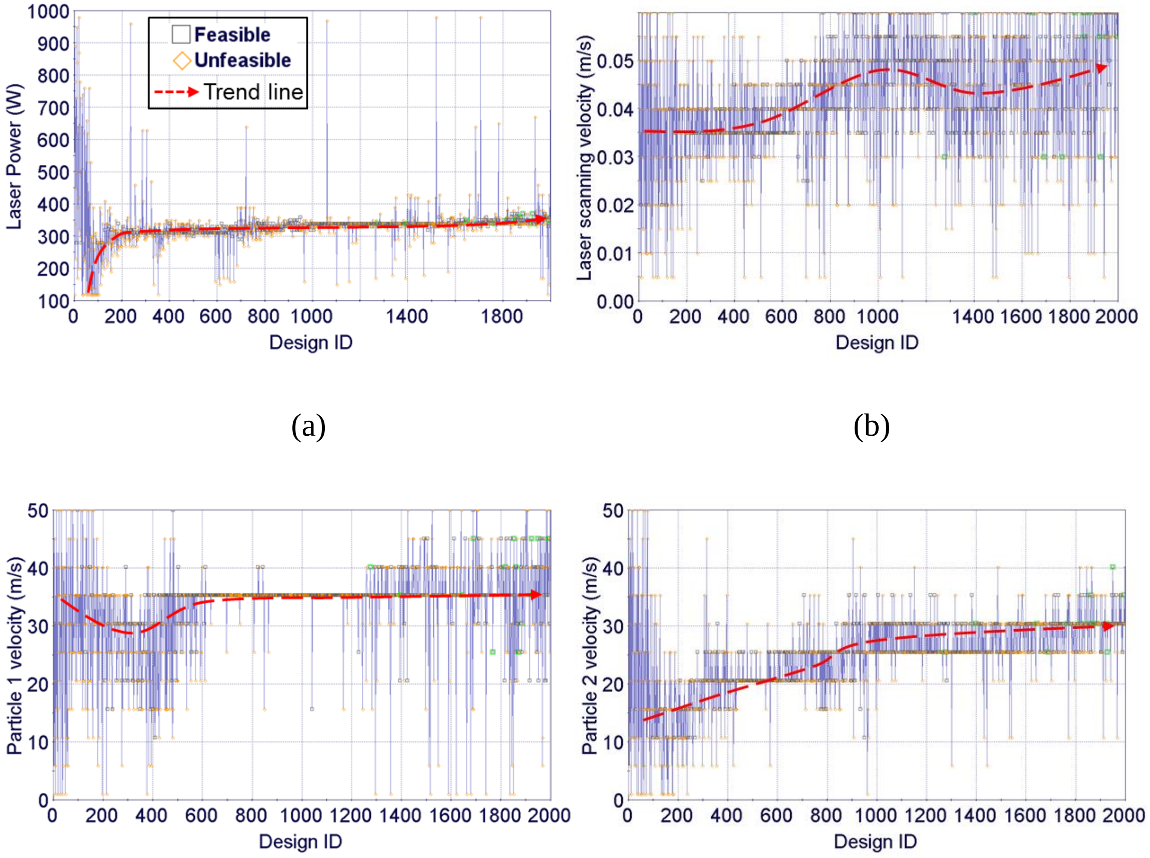

(a) (b)

(c) (d)

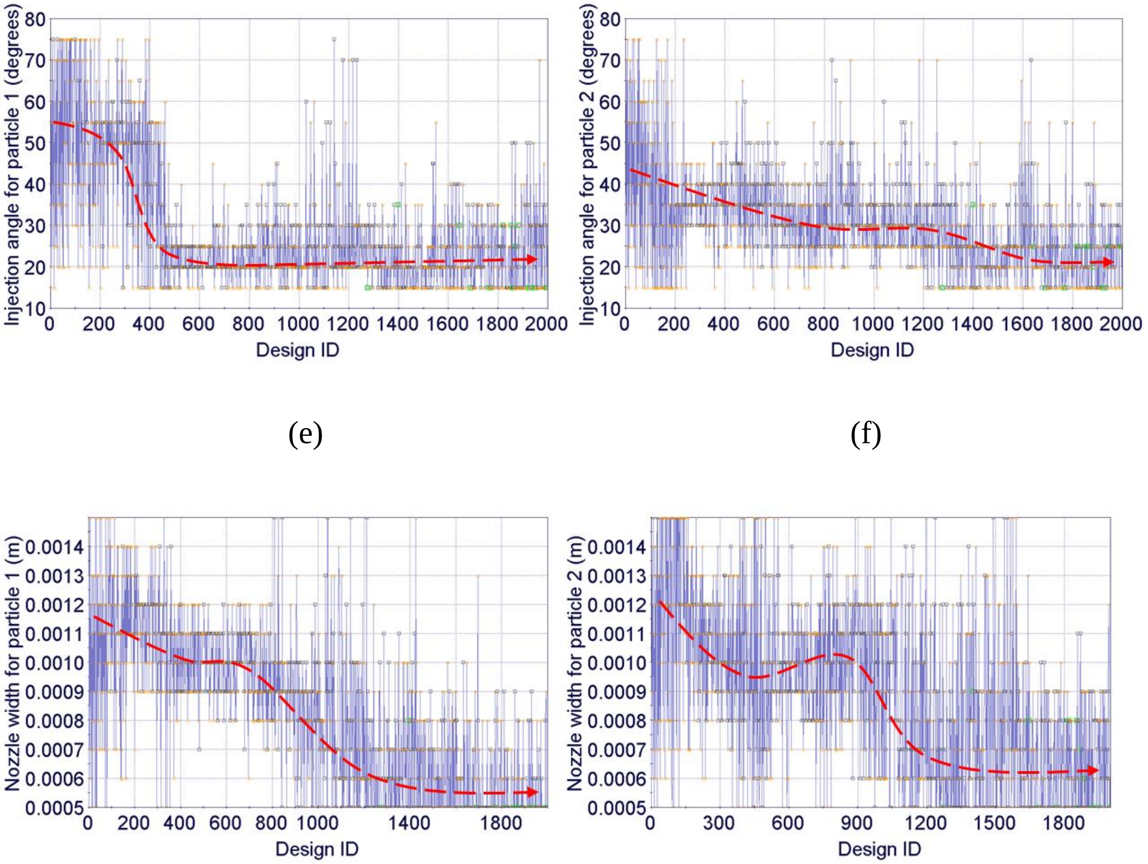

(e) (f)

(g) (h)

Fig. 4.9 Design histories of the 8 design variables (pictures share the same legend as Fig. 4.9 (a)).

The powder waste is mainly affected by the nozzles' diameters w_i and the injection angles θ_i, but also affected by other parameters, while the laser energy consumption is mainly affected by the laser power P and the laser scanning speed V. All the design variable are intertwined and synergistically affect the final designs.

First of all, the laser power finds a balance at around 350 W. The increase of laser power can lead to the following results: 1) the particle temperature and/or substrate temperature exceed the boiling temperature; 2) the melt pool size increases so that powder waste decreases; 3) the laser energy consumption increases.

Second, the laser scanning speed fluctuates between 30 mm/s and 60 mm/s. It ends up with relatively high scanning speeds, because a low scanning speed can have the following effects: 1) the substrate temperature exceeds its boiling temperature; 2) the laser energy consumption increases; 3) the melt pool size increases so that the powder waste decreases. Although the lattermost effect is beneficial, the melt pool size is not the main factor for powder waste. The powder waste is more determined by the nozzle diameters and the injection angles. Since the laser scanning speed plays a more important role on the laser energy consumption, it is advantageous to increase the scanning speed rather than decreasing it.

Third, the particle velocities. From Fig. 4.9 (c) and (d), the Inconel 718 particle velocity (v_{p1}) is obviously higher than the Ti-6Al-4V particle velocity (v_{p2}). This is due to the fact that Inconel 718 has a lower thermal resistance: a lower specific heat, a higher thermal conductivity, a lower boiling point, and lower latent heat of fusion and vaporization. Besides, Inconel 718 has a higher density, so in order to decrease the laser attenuation (for better use of the laser), it needs to be injected at a higher speed. The particle velocities singly have effect on the powder waste: increasing the particle velocities can decrease the laser attenuation, increasing the melt pool size, thus lowering the powder waste. It has no effect on the laser energy consumption, but too high velocities can also result in a low attenuation, thus vaporizing the substrate.

Then, the injection angles have conflicting effects on the powder waste: On the one hand, increasing the injection angles results in a wider spread of particles, thus increasing the powder waste; on the other hand, increasing the injection angles decreases the laser attenuation, increasing the melt pool size, thus decreasing the powder waste. The injection angles singly have effect on the powder waste. However, the former effect is more dominant than the latter, and too large injection angles can also vaporize the substrate. Therefore, the feasible designs show relatively small injection angles Fig. 4.9 (e) and (f).

Last, the nozzle diameters also have conflicting effects on the powder waste. Increasing the nozzle diameters can result in a wider spread of particles, thus increasing the powder waste. It can also decrease the laser attenuation due to the decrease of particle concentration, thus decreasing the powder waste. The nozzle diameters singly have effect on the powder waste. However, the former effect is also more dominant than the latter, and too large nozzle diameters can also vaporize the substrate. Therefore, narrower nozzle diameters are preferred, as shown in Fig. 4.9 (g) and (h).

The above example is a one-time optimization of some process parameters given the powders feed rates both at 20 g/min. When choosing the proper design(s) from Fig. 4.8, if the energy consumption is more critical than the powder waste, then the designs on the bottom of the design space are preferred; if the powder waste is more critical, then the designs on the left side of the design space are preferred. To find the best design, both costs (material cost and energy cost) should be taken into consideration. For example, in this study, the powder waste is more critical, we choose the circled Pareto design marked in Fig. 4.8. The corresponding design variables are: P = 370 W, V = 55 mm/s, $\theta_1 = \theta_2$ = 15º, V_{p1} = 45 m/s, V_{p2} = 30 m/s, $w_1 = w_2$ = 0.5 mm. This design relates to a relatively low material cost. Moreover, comparing with the topmost design, this design drastically reduces the laser energy cost. In practical applications, however, the powder recyclability and other technical conditions should also be considered to assist in the final decision.

4.5 Conclusions and Future Work

The fabrication of heterogeneous objects requires the mixing of a variable ratio of multiple powders. The powders feed rates are thus a changing variable during the fabrication process according to the material-embedded design model. The real-time optimization is difficult to achieve due to the time-consuming calculation (5 hours approximately). Therefore, this approach is more suitable as a pre-processing stage to analyze the design model and generate an operation file, which connects the model to a processing language that can be recognized by the DMD system. The proposed pre-process optimization approach has its merits in improving the print quality, and the DMD system should be able to memorize and/or even learn from the previous calculation results, which would greatly reduce the calculation time and be useful for potential real-time control.

This study provides an approach to optimize the process parameters in the pre-process stage of multi-materials DMD. A calculation example is presented for prescribed powder feed rates. This approach can be easily generalized to any materials other than Inconel 718 and Ti-6Al-4V. Additional parameters other than the 8 design variables in this study may have to be considered in the future, e.g., laser spot size/shape would alter the approach and results.

In the future, the models in this study will be modified into a coaxial four-nozzle design, and the same material will be injected from two opposite nozzles. The four-nozzle configuration can also be applied to three or four materials mixing. Also, more physical-based realistic models should be applied, considering the gas-particle two phase flow and the free surface evolution when using dissimilar materials. In addition, fully numerical solutions will be used instead of analytical ones to account for more complex configurations in the fabrication process, e.g. fabrication of multiple layers, fabrication of a thin wall, and fabrication including mixing in the melt pool. In this case, more effects should be considered when choosing the suitable designs. For example, the side effect of a high particle injection velocity might be considered: the splatter of the liquid in the melt pool, and its influence on surface finish/resolution. This type of analysis also needs a practical test based on the optimized process parameters on the real DMD system to further substantiate the model predictions before advancing to real applications.

CHAPTER FIVE

PROCESS PARAMETERS PLANNING DURING DMD OF FGM PARTS

5.1 Introduction

The DMD process can locally deposit different metallic powders to produce FGM parts as needed. Yet inappropriate mixing of materials without considering the influence of dilution/overlapping effects among layers/tracks and the variation of material properties can result in inaccurate material composition in the fabricated parts when compared to the desired compositions. Within such a context, this chapter proposes a design method that links the process parameters to the desired composition of the part based on mathematical models. The proposed scheme is illustrated through three case studies. Using the proposed method, the process parameters can be planned prior to the manufacturing process, and the material distribution deviation from the desired one can be reduced.

The DMD process can deliver dissimilar powders either via powders premixing, or via powder in situ mixing. For the powder premixing of elemental powders approach, segregation effect of dissimilar powders (due to the different densities) and remixing effect within the powder mixer exist, which increase the composition control difficulty and reduce the deposition accuracy. Therefore, in this study, the focus is on the in-situ mixing approach, where different powders are injected through different nozzles and mixed in the melt pool. The main advantage of this approach is that the powder composition can be adjusted on demand.

The schematic of the DMD working space is shown in Fig. 5.1, where the part being fabricated is an FGM part. Dissimilar powders are injected from different nozzles (typically four coaxial nozzles) and mixed in the melt pool induced by the laser beam. The part is fabricated layer by layer, and the material composition is adjustable whenever needed. The information of the part composition drives the control of the powder mixing ratio by regulating the powders feed rates. It should be noted that the delay effect due to the length of the powder delivering hose and nozzles is to be considered by introducing a time delay.

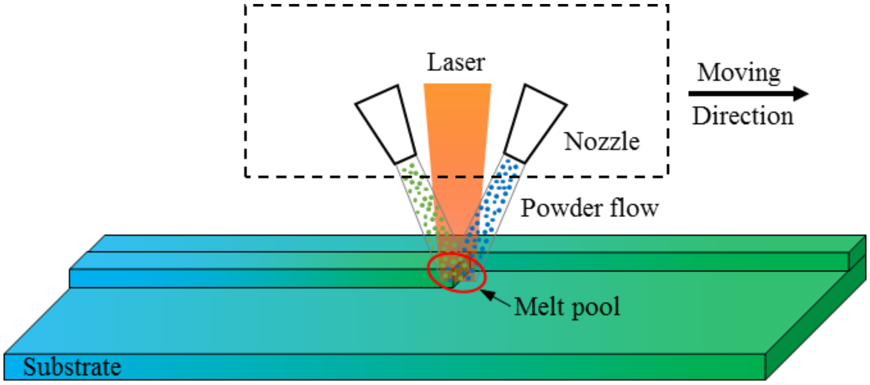

Fig. 5.1 Schematic of the DMD fabrication of a functionally graded part.

Past work in FGM parts fabrication considered a uniform material in circular or straight track, allowing a composition change only at the next track/layer [Ocylok2010] [Muller2013] [Shah2014]. This constrains the DMD's potential of FGM parts manufacturing in respect of process flexibility. To our knowledge, the investigation of composition change point by point has not been researched nor published. Meanwhile, despite the large number of reports on modeling and design of FGM parts, limited literature on the influence of the mixed/shared portion of a certain track/layer with its adjacent tracks/layers have been published. Moreover, the influence of the changing dilution rates and material properties during the process remained elusive when it comes to design for manufacturing.

In this study, a methodology for planning the process parameters in DMD fabrication of FGM parts is proposed in order to understand the link between the desired material distribution and the process parameters. Mathematical models are derived and formed to aid the design process. The proposed scheme is illustrated through three design case studies. Two case studies are of 2D thin-walled structures fabrication with one-dimensional composition variation and two-dimensional composition variation respectively. The third case study is to fabricate a 3D FGM block structure which has a three-dimensional composition variation. The materials used for the 2D cases are Inconel 718 and Ti-6Al-4V, while the materials used for the 3D case is copper and nickel. The design method is also applicable to other materials.

5.2 2D Thin-Walled Structure Fabrication

5.2.1 Model Based Design Methodology

A thin-walled part can be approximated as a 2D structure where the material distribution is homogeneous in the wall thickness direction. As shown in Fig. 5.2, the wall thickness direction is perpendicular to the paper. Basically, the volume fraction or concentration for each component material throughout the part can be analytically expressed. For manufacturing and modeling consideration, the FGM part is discretized and represented by cell arrays, as illustrated in Fig. 5.2. The cell volume is sufficiently small compared to the part, and the material composition remains the same within each cell. In this premise, the process parameters only vary when the laser scans across cells. According to our previous work [Yan2014] [Yan2015], many process parameters can be varied in order to achieve specific objectives such as minimize powder waste and/or laser energy consumption. These parameters include the laser power and scanning speed, the powder injection velocity and angle, and other changeable parameters. Herein we adopt a similar idea but focus on how to plan the process parameters in order to fabricate a part with specific composition variation. Since the manufacturing stability and composition control are also critical issues in this focus, some process parameters need to be preset. These parameters mainly include three categories: (1) the laser power P which is uniformly attenuated from the initial laser power P_0, the laser scanning speed V, and the laser spot radius r_l (2) the total powder volumetric feed rates $\dot{V}_{pi}$ (i=1,2 represents two powders), the particle radii r_{pi} and the particle speeds v_{pi}; (3) the nozzle diameter w, and the injection angles θ_i (i = 1,2 for separate nozzles). Since studying the variations of all these parameters can be computationally expensive and can even destabilize the fabrication process, the design variables in this study only include the volumetric feed rates of the two powders $\dot{V}_{pi}$ and the initial laser power P_0.

The mixing of powders occurs in the melt pool, where multiple driving forces exist. The magnitude of the melt pool molten flow speed is analytically calculated to be about 0.5-1 m/s [DebRoy1995] [Yan2000] [He2003], and this has also been demonstrated computationally in the DMD process and the like [Picasso1994] [Ki2002] [Morville2012], as well as in our previous work shown in Section 4.2.2. With the high melt pool velocity, the mixing process can be seen as instant and uniform.

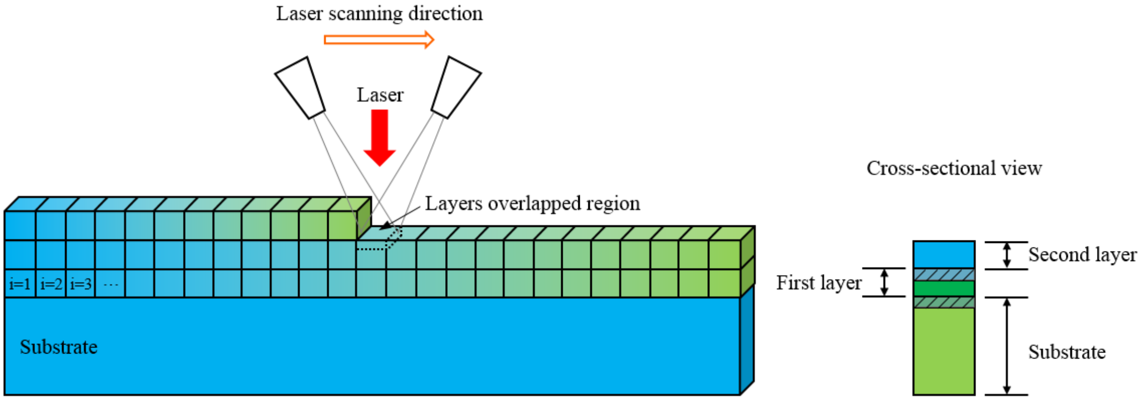

Fig. 5.2 Schematic illustration for 2D thin-walled part discretization and the dilution effect on mixing.

The substrate used is a uniform material. In this study, we will apply uniform substrate. The dashed cell under the laser beam indicates the melted region on the former layer. The shaded regions in the cross sectional view represent the shared portions between layers due to dilution. Each new layer starts on top of the previous layer, but has an overlapped region with the previous layer. The composition of a cell in the new layer is the resultant of the mixing of the instant powder composition and the composition of the cell beneath. The dilution rate *D* is defined as the ratio of the cross-sectional area of the melted substrate to the total cross-sectional area of the melted substrate and the deposited clad. When determining the composition of the actual fabricated part, the effect of dilution should be considered as well as the instantaneous powder composition:

$$C^1_{i,des} = D^1_i \times C_{i,sub} + \left(1 - D^1_i\right) \times C^1_{i,} \tag{5.1}$$

$$C^{2}_{i,des} = D^{2} \times C^{1}_{i,des} + (1-D)^{2} \times C^{2}_{i,} \tag{5.2}$$

$$C^{n}_{i,des} = D^{n} \times C^{n-1}_{i,des} + (1-D)^{n} \times C^{n}_{i,} \tag{5.3}$$

where C is artificially defined as the concentration of a specific material; the superscripts represent the layer number; i is the cell number in each layer, as shown in Fig. 5.2; the secondary subscripts indicate the layer number; and C_{des}, C_{sub}, and C_{pow} represent the desired concentration, the substrate concentration, and the powder concentration respectively. The desired concentration is a function of the dilution rate, the previous layer's concentration, and the powder concentration. Note that the concentration always refer to the same material specified.

The dilution rate can be predicted using the following equation [Unocic2003]:

$$D = \left(1 + \frac{\eta_d \dot{V}_p \Delta H_s}{\eta_a \eta_m P_0 - \eta_d \dot{V}_p \Delta H_p}\right)^{-1} \tag{5.4}$$

where η_a, η_d, and η_m are the efficiencies for laser absorption, powder deposition, and melting; $\dot{V}_p$ is the total powder volumetric feed rate (mm^3/s); P_0 is the initial laser power; and ΔH_s and ΔH_p are the melting enthalpies (J/mm^3) of the substrate and the powder materials. The efficiency of laser absorption η_a includes two parts: the absorptivity due to material optical property (η_l) and the absorptivity due to the shadowing effect of powders (η_n). The melting efficiency (η_m) is defined as the fraction of the laser energy actually used for inducing the melt pool. The remaining energy other than the energy used for melting is the dissipated to the unmelted region by thermal conduction.

$$\eta_m = \frac{Vol}{q_i}\left[\Delta h_f + \int_{T_r}^{T_l} C_p(T)\, dT\right] \tag{5.5}$$

where *Vol* is the volume of melt pool, q_i is the input power, Δh_f is the heat of fusion, T_r and T_l represent room temperature and liquidus temperature respectively, C_p is heat capacity, and T is temperature. For a 2D case, the melting efficiency is given by [Wells1952] [DoPont1995]:

$$\eta_m = \frac{1}{\frac{8\alpha}{5Vd} + 2} \tag{5.6}$$

where V is the laser scanning speed; d is the melt pool width; and α is the thermal diffusivity, which is related to the material composition of the substrate. It can be seen from Eqs. (5.4) and (5.6) that the dilution rate depends on the substrate concentration, since ΔH_s, ΔH_p, and α are all functions of the substrate concentration. The substrate herein is not restricted to the original substrate, but also can be any underlying layer on top of which the new layer is being deposited.

In Eq. (5.4), the $\eta_a P_0$ term is defined as the attenuated laser power P, where $\eta_a = \eta_m \eta_n$. Considering the powder shadowing effect, η_n can be calculated using the Beer-Lambert Law:

$$P = \eta_l \eta_n P_0 = \eta_l e^{-\varepsilon C_{pow} z} P_0 \tag{5.7}$$

where C_{pow} is the powder concentration; $\varepsilon = \frac{3(1-\eta_l)}{2 r_p \rho_p}$ is the molar absorptivity or extinction coefficient (m^2/kg); r_p and ρ_p are the radius and density of the powder particles, and ρ_p is also dependent on the powder composition. The powder concentration is a variable along the laser scanning direction due to the overlapping of the two powder jets. However, it can be seen from Fig. 5.3 (a) that the two shadowed areas can be equalized. Flipping the lower shadowed area, the equivalent shadowing effect can be represented as Fig. 5.3 (b), where the laser beam passes two trapezoidal regions of two materials respectively. Then, assuming the attenuation is constant within the laser beam at a specific time, Fig. 5.3 (b) can also be equalized to Fig. 5.3 (c), where the laser beam passes two rectangular regions of two materials respectively. We assume that the powder injection angle is θ, the laser beam width equals to b, and neglect the powder jet divergence angle. Then Eq. (5.7) can be rewritten as:

$$\begin{aligned} P &= \eta_l exp\left[-\frac{3(1-\eta_l)}{2r_{p1}\rho_{p1}} \cdot \frac{\dot{V}_{p1}\rho_{p1}}{\pi\left(\frac{w}{2}\right)^2 v_{p1}} \cdot z - \frac{3(1-\eta_l)}{2r_{p1}\rho_{p2}} \cdot \frac{\dot{V}_{p2}\rho_{p2}}{\pi\left(\frac{w}{2}\right)^2 v_{p1}} \cdot z \right] P_0 \\ &= \eta_l exp\left\{ -\frac{6(1-\eta_l)\dot{V}_{p1}}{\pi w^2 r_{p1} v_{p1}} \left[\frac{L\sin\varphi}{sin(\theta+\varphi)} + \frac{w}{2\sin\theta} \right] - \frac{6(1-\eta_l)\dot{V}_{p2}}{\pi w^2 r_{p1} v_{p1}} \left[\frac{L\sin\varphi}{sin(\theta+\varphi)} + \frac{w}{2\sin\theta} \right] \right\} P_0 \end{aligned} \tag{5.8}$$

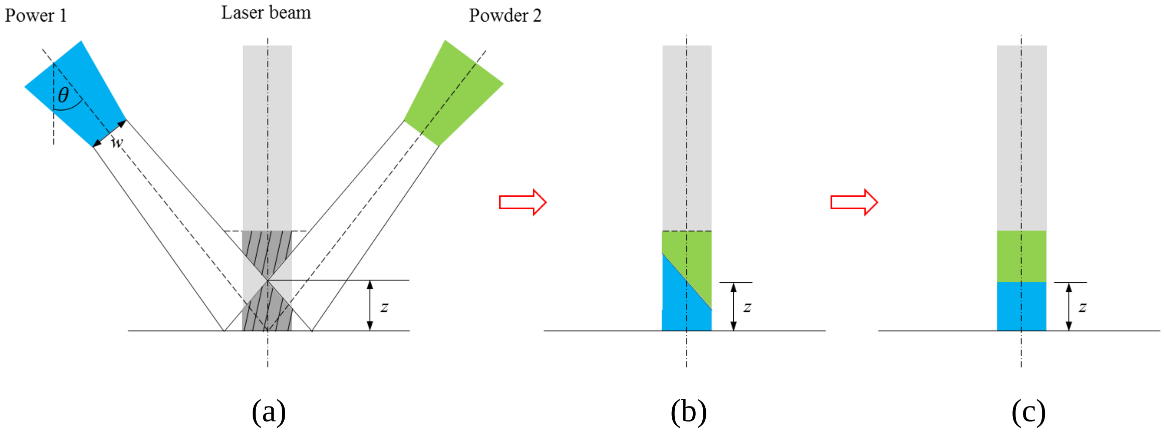

(a) (b) (c)

Fig. 5.3 Equating of the powder shadowing effect.

The attenuated laser power (P) required can be determined via FEM simulation, which is discussed in the case studies. Then the initial laser power (P_0) can be reversely solved using Eq. (5.8). Following Eq. (5.3), the required powder concentration ($C_{i,pow}^{n}$) at any layer and any cell can also be solved. During the calculation, the material properties of the mixture are calculated following the mixing theory:

$$P_{mixture} = \left(1 - C\right) P_1 + C P_2 \tag{5.9}$$

where $P_{mixture}$ is any material property for the mixture, P_1 and P_2 are the material properties for material 1 and material 2 respectively. It is assumed in this study that the material properties are not a function of temperature. Other mixture rules could be used, however, our objective is to show a process, and let the engineers decide which is the most appropriate mixture rule depending on the materials they use and their own expertise. For example, the properties of the mixture can also be estimated by using the mass fractions of the two components:

$$P_{mixture} = \frac{\rho_1}{(1-C)\rho_1 + C\rho_2}(1-C)P_1 + \frac{\rho_2}{(1-C)\rho_1 + C\rho_2}CP_2 \qquad (5.10)$$

The results of using different mixture rules are presented and compared in the case studies in Section 5.2.2. The design process that the case studies follow is illustrated in Fig. 5.4. The input variables are given by the designers and are circulated in the dashed rectangles, and the output variables are in the bold rectangles.

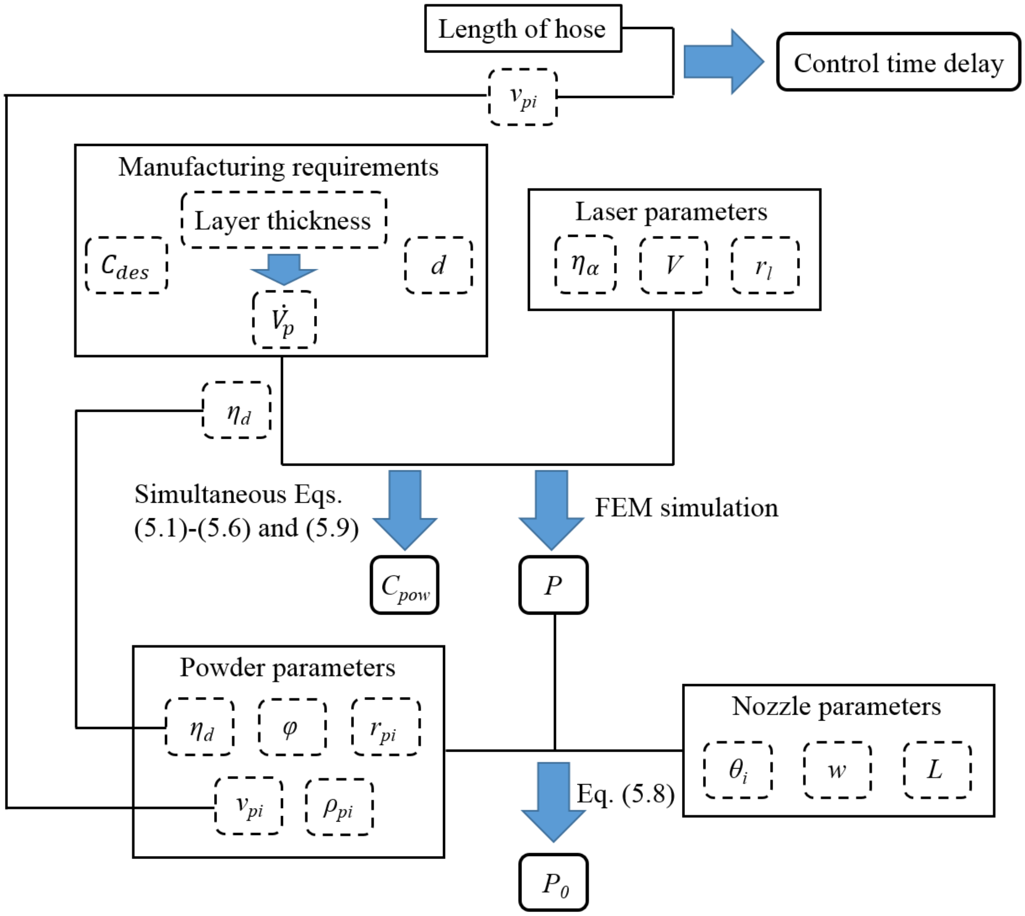

Fig. 5.4 Design process flowchart for 2D FGM part fabrication.

5.2.2 Case Studies

5.2.2.1 Case 1: FGM Part Fabrication with 1D Composition Variation

The objective of this case study is to fabricate a thin-walled FGM part with dimension 3 mm × 20 mm (Fig. 5.5 (a)). The component materials are Inconel 718 (material 1) and Ti-6Al-4V (material 2). The physical and thermal properties of the two materials are listed in Table 5.1 [Pottlacher2002] [Boivineau2006] [Chen2011].

Table 5.1 Physical and thermal properties of Inconel 718 and Ti-6Al-4V.

Properties	Inconel 718	Ti-6Al-4V
Laser absorptivity, η_l	0.3	0.3
Emissivity, E	0.4	0.4
Density, ρ (kg/m^3)	8190	4420
Specific heat, c_p (J/kg/K)	435	610
Thermal conductivity, k (W/m/K)	21.3	17.5
Thermal diffusivity, α (m^2/s)	5.98×10^{-6}	6.49×10^{-6}
Melting temperature, T_{melt} (K)	1609	1928
Melting enthalpy, ΔH (J/mm^3)	8.19	6.63

The concentration in this case study is always specified for the Ti-6Al-4V. The concentration distribution of the desired part has the following function (Fig. 5.5):

$$C = \frac{x}{L_x} \tag{5.11}$$

Consequently, the concentration for Inconel 718 is $\left(1-\frac{x}{L_x}\right)$. For the case of 1D composition variation, the concentration only varies along the *x*-axis. Therefore, the fabrication process is iterative, layer by layer, and the process parameters remain the same among layers. However, the manufacturing direction does not necessary follow the direction in Fig. 5.5 (a). The fabrication direction in Fig. 5.5 (b) provides a way to reduce the changing rate of powder concentration in each layer. The tradeoff is that the number of layers will increase, which may affect the manufacture speed and the physical properties of the fabricated part. Determining which manufacturing direction to choose depends on different situations. In this study, we perform process parameters planning for both building directions.

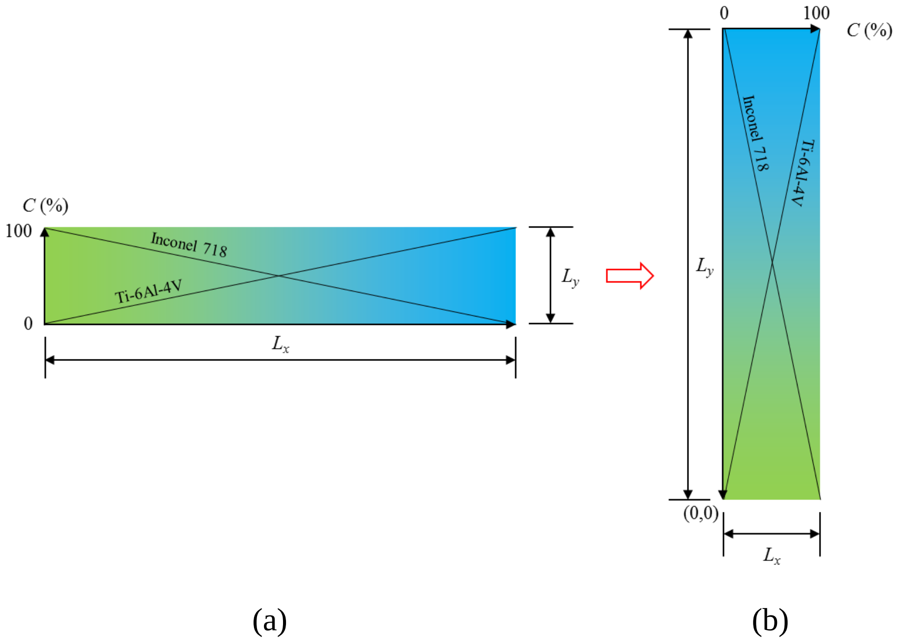

Fig. 5.5 FGM part with 1D composition variation.

Case 1 (a):

Before calculating the key variables ($\dot{V}_{pi}$ and P_0), some constant variables need to be preset as input variables to stabilize the fabrication process. As discussed above, these preset parameters include the attenuated laser power P, laser scanning speed V, laser spot radius r_l, powder total volumetric feed rate $\dot{V}_p$, injection angle θ_i, nozzle diameter w, particle speed v_{pi}, particle radius r_{pi}, powder divergence angle φ, the distance between the nozzle center and the spot center L, and the width (wall thickness) of the thin-walled part d. According to Eq. (5.8), the selection of these input parameters can affect the value of the final laser power. The laser power decreases with the injection angle and the size of a particle, and increases with the nozzle diameter. However, the powder deposition efficiency $\eta_d \approx b / w$ will decrease as the nozzle diameter increases. If different process parameters are applied to the two powders, the attenuation effect should be treated separately, as Eq. (5.8) shows.

The width of the part d is set at constant 0.7 mm, the particle radius is assumed to be constant 10 μm. The particle speed v_p, injection angle θ and the nozzle diameter w are set at 10 m/s, 30º and 2 mm respectively. The divergence angle φ is assumed to be 5º, and L is set at 10 mm. The laser beam radius b is 0.6 mm. To determine the attenuated laser power needed to melt the substrate, the FEM simulations on COMSOL Multiphysics® are performed. Since the composition of the part keeps changing during the fabrication, it is difficult to determine the minimum laser power needed for every spot. Therefore, in order to find a minimum P for every spot, two extreme simulations are run assuming that the substrate consists of only Inconel 718 or Ti-6Al-4V respectively. The power should be able to at least generate a melt pool width large enough to cover the width of the part d. The P required is then the maximum P of the two extreme simulations. In the simulation, r_l is fixed to 0.3 mm, and V is fixed to 20 mm/s. A continuous Gaussian beam moves on the symmetrical semi-domain. The energy distribution of the moving Gauss beam under Cartesian coordinate can be expressed as:

$$P(x, y) = \eta_a P_0 \frac{1}{\sigma\sqrt{2\pi}} e^{-\frac{(x-Vt)^2+y^2}{2\sigma^2}} \tag{5.12}$$

where σ is the standard deviation which equals to $r_l/3$. The governing heat equation for the temperature evolution of the substrate due to a moving laser heat source is:

$$\rho c_p \frac{\partial T}{\partial t} + \rho c_p V \cdot \nabla T = \nabla \cdot \left(k \nabla T\right) \tag{5.13}$$

where T is the substrate temperature, t is time. The convection and radiation boundary conditions are applied on the peripheral surfaces of the substrate, and the bottom surface is subject to thermal insulation. The minimum P required for pure Inconel 718 and Ti-6Al-4V are 130 W and 105 W respectively, and we choose the larger one (130 W) as P.

The remaining process parameter that needs to be predetermined is the powder volumetric feed rate $\dot{V}_p$, and it is related to the manufacturing resolution in the vertical direction, i.e., the height of a single layer h. According to Fig. 5.2 and from mass conservation,

$$h = \frac{\eta_d \dot{V}_p}{Vd} \tag{5.14}$$

where the deposition efficiency η_d is assumed to be a constant 0.3 (estimated from b/w). Suppose that a 0.3 mm layer height is needed to complete the fabrication in 10 loops. This requires a total volumetric powder feed rate of 14 mm^3/s. For the horizontal direction, we require a 1 mm resolution for the concentration change, which means that the dimension of a cell in the *x*-axis is 1 mm. The *x* position of any cell is represented by the *x* position of its center. Hence the desired concentrations for a consecutive of cells (i = 1, 2, 3, …, 20) in one layer are $C_{i,des}^{n}$ = 2.5%, 7.5%, 12.5%, …, 97.5%.

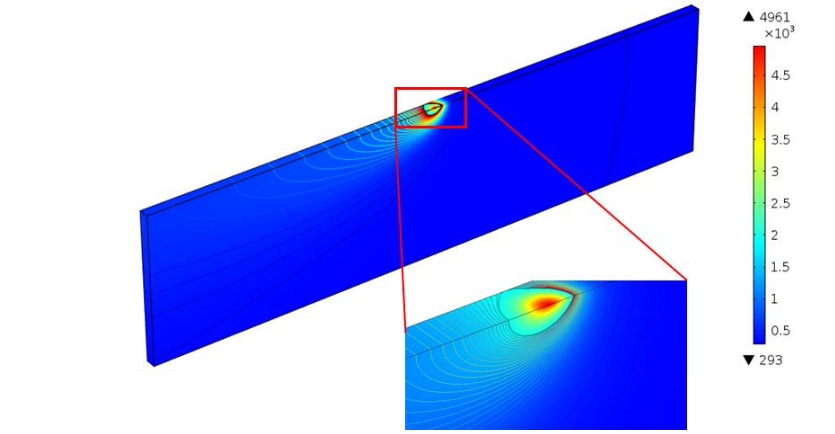

Fig. 5.6 Typical simulation result (half space due to symmetry) for laser substrate heating. The innermost isotherm line represent the melt pool.

The substrate composition is also critical to the whole process. The best condition is that the substrate has the same composition as the desired FGM part, then the powder concentration will be exactly the same as desired regardless of the dilution effect. However, in most situations the substrate composition is a single material which is most available. Therefore, we start from the substrate which is composed of a single component material only. The first layer or several layers may not achieve the desired concentration but eventually it will. The final part can be fabricated by finally removing the first several sacrificial layers. In this case, we choose Ti-6Al-4V as the substrate material ($C_{i,sub} = 1$, $i = 1, 2, \ldots, 20$).

Combining Eqs. (5.1) - (5.6) and (5.9), the locally varied dilution rate and the volumetric powder feed rates ($\dot{V}_p \times C_{i,pow}^n$ for Ti-6Al-4V and $\dot{V}_p \times \left(1 - C_{i,pow}^n\right)$ for Inconel 718) we should actually apply can be obtained by solving these simultaneous nonlinear equations. The calculated locally variation of the two powders' feed rates and the dilution rate for the first layer are shown in Fig. 5.7. It is understandable that the injected powder at the initial locations is composed of only Inconel 718, since the desired Ti-6Al-4V concentration in the part should be increased gradually from 0 to 1 and the substrate is made of pure Ti-6Al-4V. It can also be imagined that when mixed with the substrate material, several sacrificial layers are needed in order to achieve the desired concentration. These sacrificial layers should finally be cut off via post processing such as lathing or milling. Therefore, a second trial is then conducted to test the achievability of the desired composition. An indicator of the achievability is the maximum/minimum powder feed rate of Inconel 718/Ti-6Al-4V at the initial locations: only when there is no maximum/minimum powder feed rate can we assert that the desired composition is achieved. From Fig. 5.8 we can see that the desired composition is still not achieved, so the trail is continued. However, a contradiction exists in that the substrate is made of pure Ti-6Al-4V but we desire a zero concentration of Ti-6Al-4V in the leftmost location of the part. In this sense, we may assume that the desired composition is achieved whenever the second location does not require a maximum/minimum powder feed rate. Fig. 5.9 shows the powders feed rates and dilution rates when depositing the third layer. We can believe that the desired composition is achieved only at this layer, and this "third layer" is thus seen as the actual "first layer". Then, when calculating the remaining layers, their previous layer's physical properties will be calculated directly according to the desired composition.

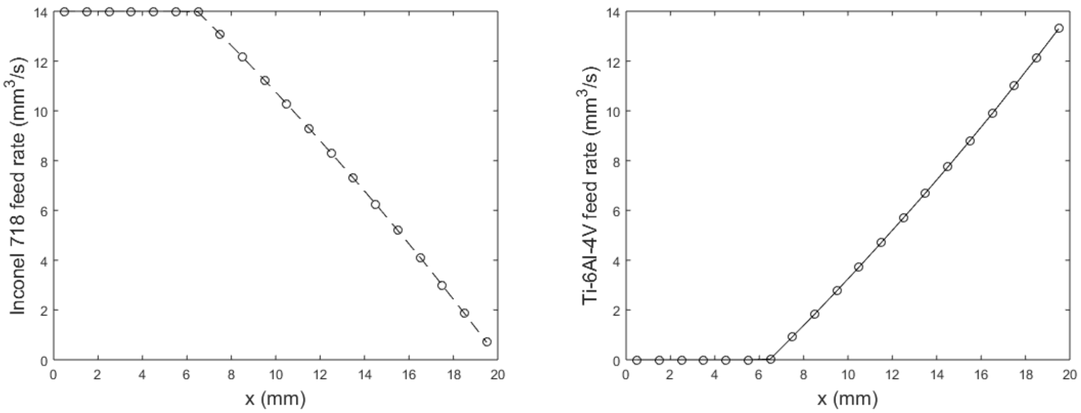

(a) (b)

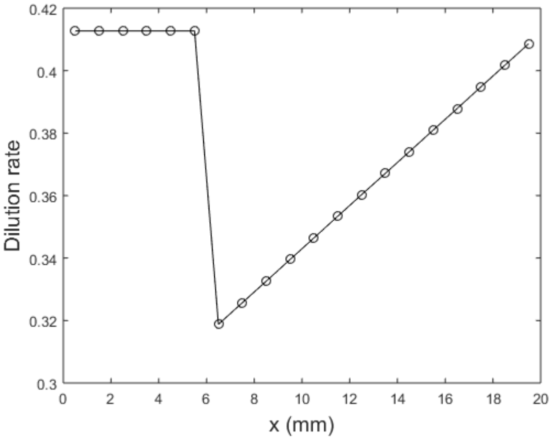

(c)

Fig. 5.7 First trial: (a) the volumetric feed rate of Inconel 718, (b) the volumetric feed rate of Ti-6Al-4V, and (c) the dilution rates at each location.

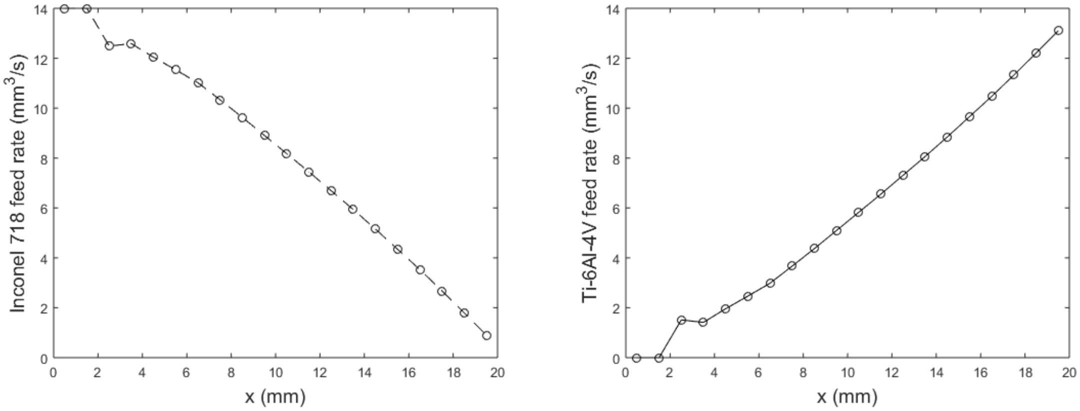

(a) (b)

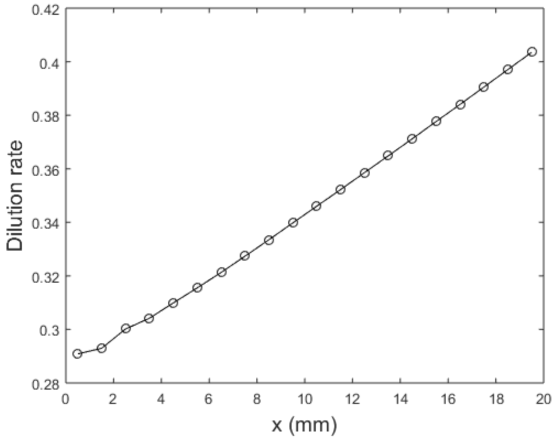

(c)

Fig. 5.8 Second trial: (a) the volumetric feed rate of Inconel 718, (b) the volumetric feed rate of Ti-6Al-4V, and (c) the dilution rates at each location.

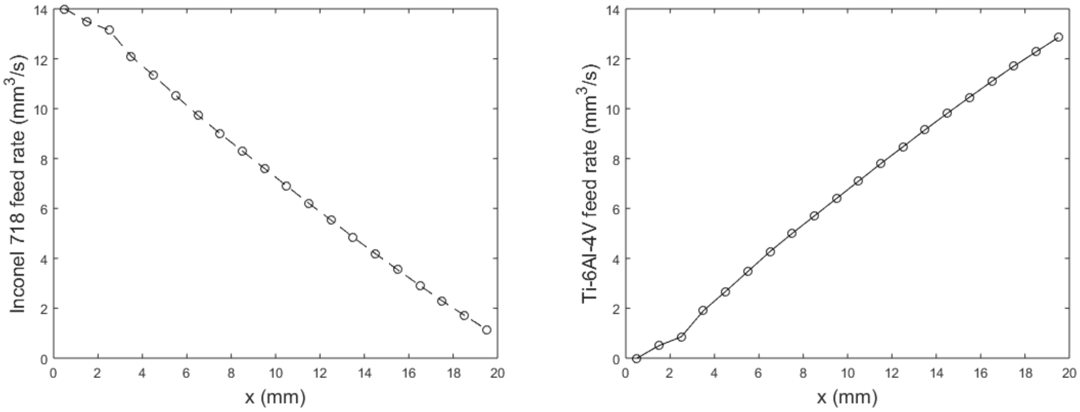

(a)

(b)

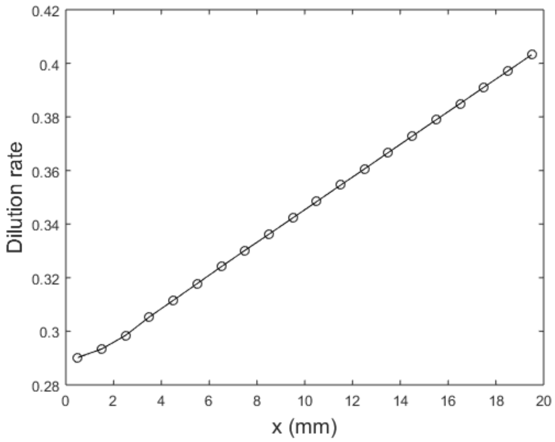

(c)

Fig. 5.9 Third trial: a) the volumetric feed rate of Inconel 718, (b) the volumetric feed rate of Ti-6Al-4V, and (c) the dilution rates at each location.

Fig. 5.10 shows the plots for the final powders feed rates and the dilution rates at each discrete fabrication location. Since in this case the composition varies in 1D, once the desired composition is achieved and stabilized at the first and second layers, there is no need to vary the powders composition any more among layers. The process becomes a layer by layer iteration after the second layer. It can be seen that the two curves in each of the sub-figures of Fig. 5.10 are very close. This is understood and explained by the fact that the more sacrificial layers to cut, the closer the two curves will be. The two curves will eventually be overlapped when the number of sacrificial layers are large enough.

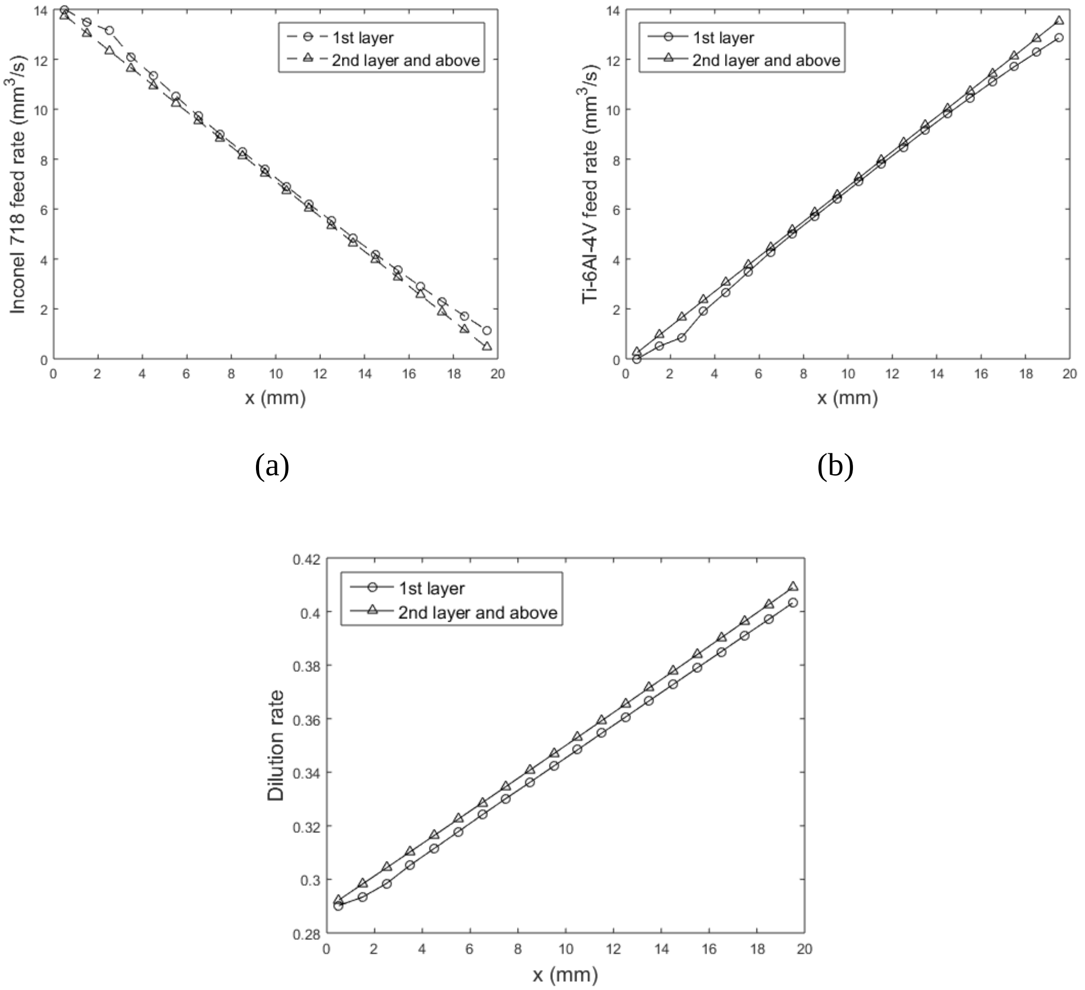

(a)

(b)

Fig. 5.10 Final results: (a) the volumetric feed rate of Inconel 718, (b) the volumetric feed rate of Ti-6Al-4V, and (c) the dilution rates at each location.

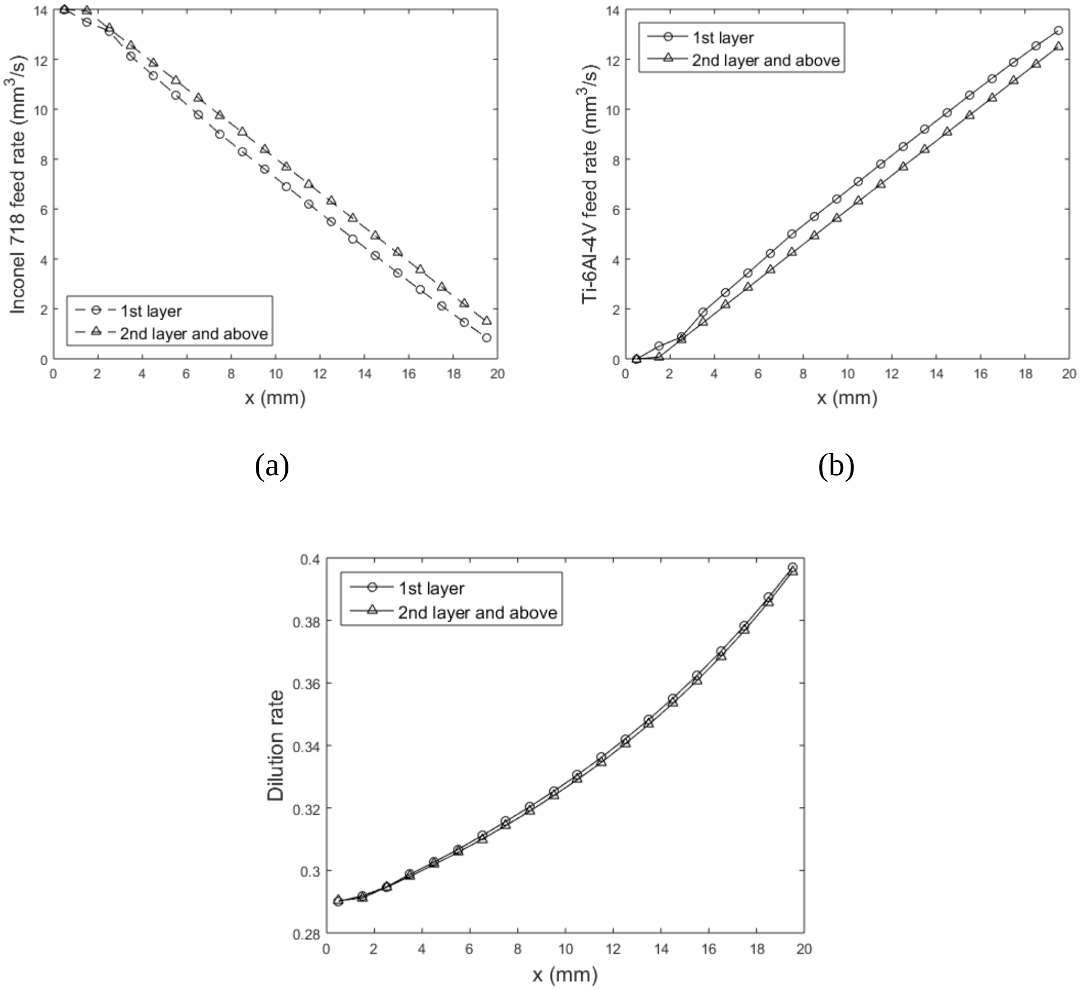

(a)

(b)

(c)

Fig. 5.11 Final results using an alternative mixture rule: (a) The volumetric feed rate of Inconel 718, (b) the volumetric feed rate of Ti-6Al-4V, and (c) the dilution rates at each location.

An alternative mixture rule is used and the new result (Fig. 5.11) is compared with the current result (Fig. 5.10). The equation used for the new mixture rule is expressed in Eq. (5.10), which is a mass ratio based approach. The trends for the powders feed rates using the two mixture rules are similar with a slight difference, while the difference of the dilution rates is apparent. It can be seen that the dilution rate plot for using the mass ratio based mixture rule shows an obvious curved trend, and this causes the differences of the powders feed rates.

In this case, the total laser power usage is about 25.4%, which is the combination of both the powder shadowing effect (84.7%) and the laser absorptivity by the substrate (30%). The actual laser power used is calculated as 510.9 W using Eq. (5.8). The laser power is calculated as a constant value, since the laser attenuation by powder depends on the powders' total volumetric flow rate instead of the concentration of any single powder. Finally, the initial two sacrificial layers (0.6 mm thickness) should be removed.

Case 1 (b):

The alternative building direction of the desired part is illustrated in Fig. 5.5 (b), where the composition in each layer is constant. For this approach, the concentration in each layer varies from 0 to 1 bottom to up. Inconel 718 is selected as the substrate material ($C_{i,sub} = 0$, $i = 1, 2, \ldots, 10$). Apparently, the building direction is not unique: a 1 to 0 sequence is completely equivalent, the only difference is that the substrate material will be Ti-6Al-4V. Similarly, the Case 1 (a) can be also implemented from right to left.

In this case, we assume that all the preset process parameters are the same as Case 1 (a), except the powder volumetric flow rate $\dot{V}_p$. If we still set $\dot{V}_p$ = 14 mm^3/s, resulting in a 0.3 mm layer height, then it will take 66.7 deposition loops (67 layers) to complete the fabrication. In order to make this number an integer and reduce the total number of layers, we set $\dot{V}_p$ = 18.7 mm^3/s to result in a 0.4 mm layer height. The total number of layers then becomes 50. Further reducing the layer number would require an even larger $\dot{V}_p$. Consequently, the deposition efficiency η_d would not simply remain the same, and the dilution rate would be too low to support deposition.

The cell width is fixed to 0.3 mm, and each layer contains 10 cells. Therefore, a 10 × 50 cells array is formulated. The desired concentrations for cells in different layers (n = 1, 2, 3, …, 50) are $C^n_{i,des}$ = 1%, 3%, 5%, …, 99%. The volumetric feed rates of the two powders and the dilution rate for each layer are shown in Fig. 5.12. Comparing with Case 1 (a), the results show a linear trend at the beginning of deposition. This is because the concentration gradually changes from 0 (the substrate) to 1, and there is no need to vary the powder concentration in each layer, so that sacrificial layers are not needed. For each layer, the resulted powder concentration is slightly higher than the desired concentration, since the layer below has a lower concentration. It can be seen from Fig. 5.12 (c) that the dilution rate is low comparing with Case 1 (a), due to the fact that the $\dot{V}_p$ is larger in this case. The design result for using the alternative mass ratio based mixture rule is similar as the current result (therefore not presented here). The corresponding dilution rate plot is shown in Fig. 5.12 (d), with a similar curved plot.

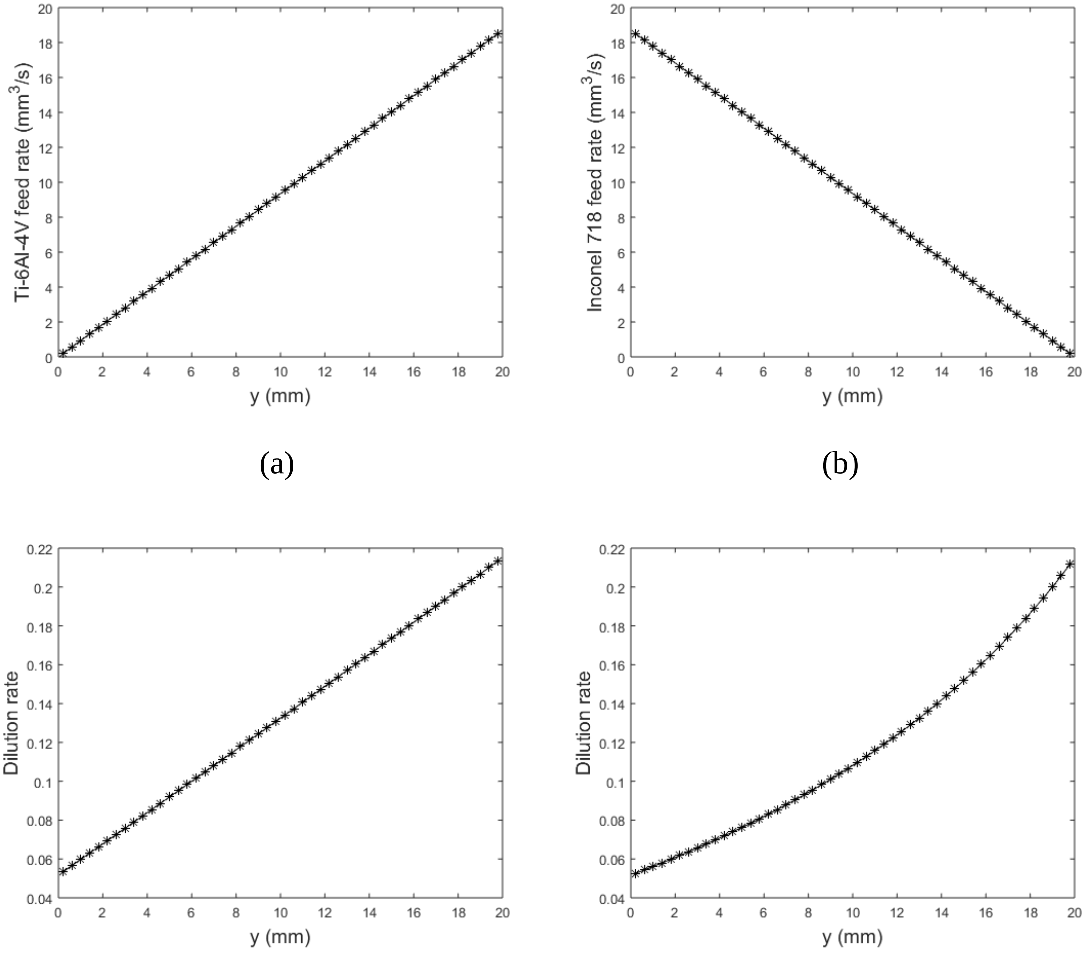

(a) (b)

(c) (d)

Fig. 5.12 The volumetric feed rate of (a) Ti-6Al-4V and (b) Inconel 718; (c) the dilution rate for each layer, and (d) the dilution rate plot using an alternative mixture rule.

Finally, the laser power needed is calculated as 540 W, which is slightly higher than Case 1 (a). In this case, the total laser power usage is 24.1%, considering the powder shadowing effect (80.2%) and the laser absorptivity by the substrate (30%). The reason for the lower laser power usage is also due to the higher total powder volumetric flow rate that results in a stronger shadowing effect.

Comparing the two fabrication approaches, the first approach varies the powder concentration within a layer and beyond the second layer the variation is repetitive, while the second approach varies the powder concentration among layers but the powder concentration remains the same within a layer. The dilution rate is a variable within a layer in the former case, while the dilution rate is constant within a layer but varies among layers in the latter case. The main disadvantages of the first approach include: (1) it takes more time for altering the mixing ratio during the fabrication, which lowers the manufacturing precision; (2) it may need a functionally graded substrate instead of a substrate made of pure material. The main disadvantages of the second approach are: (1) more layers are needed due to the incapability of forming a thick layer, which increases the fabrication time and accumulates deviation/error; (2) the dilution rate is low, which may reduce the connection strength among layers. In summary, the choice of fabrication direction can be different according to different situations.

5.2.2.2 Case 2: FGM Part Fabrication with 2D Composition Variation

In this case study, process parameters are to be planned to fabricate an FGM part with concentration variation in 2D. The part is of the same dimension as Case 1 (3 mm × 20 mm), and is composed of the same materials (Inconel 718 as material 1 and Ti-6Al-4V as material 2). In order to avoid the zero concentration at end points or edges and thus the appearance of sacrificial layers, the desired concentration is designed to be from 0.2 to 0.8, as shown in Fig. 5.13 (b). The minimum concentration (C = 0.2) is at the lower left corner, and the maximum concentration (C = 1) is at the upper right corner. The other two corners both have concentrations of 0.5. The transitions among these points are all smooth linear.

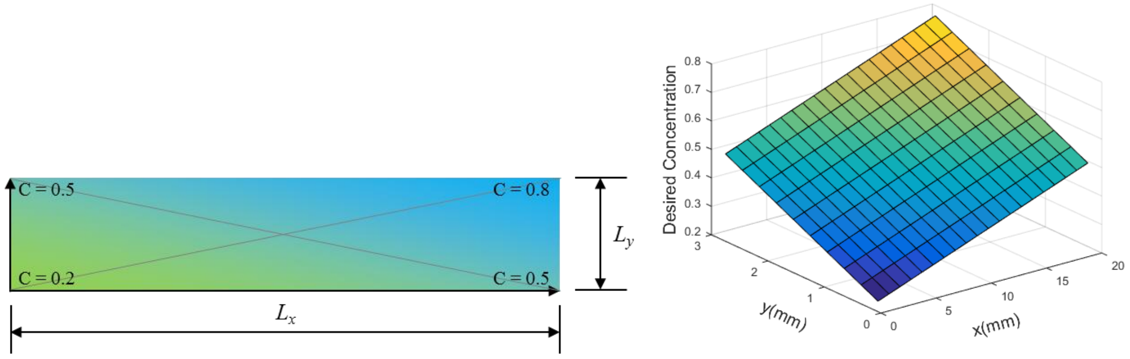

(a) (b)

Fig. 5.13 Illustration of the desired FGM part with 2D concentration variation.

The concentration distribution of the desired part follows the function below:

$$C = 0.2 + 0.3 \times \left(\frac{x}{L_x} + \frac{y}{L_y} \right) \tag{5.14}$$

Consequently, the concentration for Inconel 718 is $0.8 - 0.3 \times \left(\frac{x}{L_x} + \frac{y}{L_y} \right)$. For the 2D variation case, the concentration varies along both *x*-axis and *y*-axis, so there is no significant difference between adopting the two fabrication directions. However, the number of layers are fewer and the deposition precision is higher using the horizontal fabrication direction. Therefore, the horizontal fabrication is adopted in this study.

Assume that the preset parameters have the same values as Case 1 (a). The P value is still 130 W, and the initial laser power P_0 can be calculated from Eq. (5.8). Since the bottom layer of the part has a relatively low concentration of Ti-6Al-4V, Inconel 718 is used as the substrate material in this case.

Following the same calculation procedure, the volumetric flow rates of the two powders and the dilution rates are shown in Fig. 5.14. It can be seen that except for the first layer, the results for all the other layers are almost parallel with each other. This is understandable since the first layer is built on the substrate, and there is a gap between the substrate concentration and the desired concentration. After the second layer, since the previous layer already achieves the desired concentration, the powder concentration just needs to increase a certain amount to satisfy the gradient concentration variation. Finally, the actual laser power needed is 510.9 W, which is the same as Case 1 (a). In this case, using the alternative mass ratio based mixture rule, the design result is also similar to the current result (not presented). Although it is obvious that Fig. 5.14 (c) and (d) have detectable differences, their corresponding numbers differ by only around 2.5%. Therefore, using the mass ratio based mixture rule generally does not significantly affect the design result. However, as mentioned in earlier text, the results always need to be recalculated whenever a new mixture rule is applied. Although there may be only slightly differences, engineers need to determine the most appropriate mixture rule to use in order to best fit design to applications.

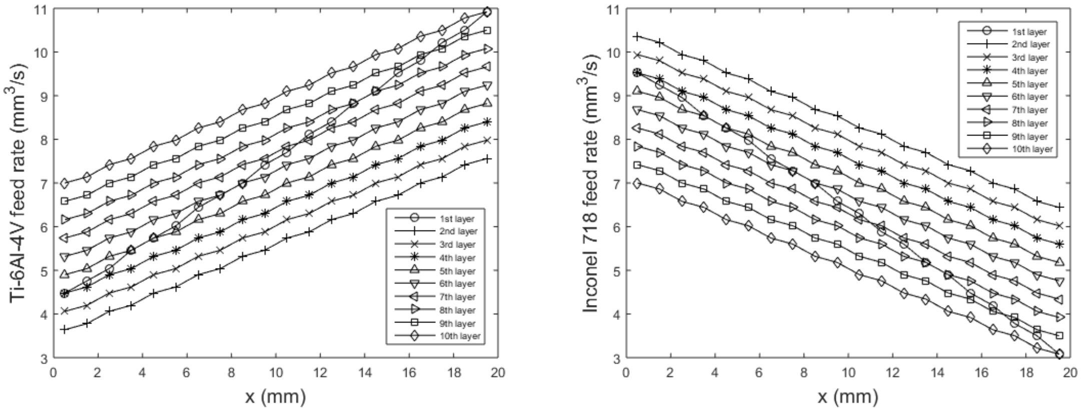

(a)

(b)

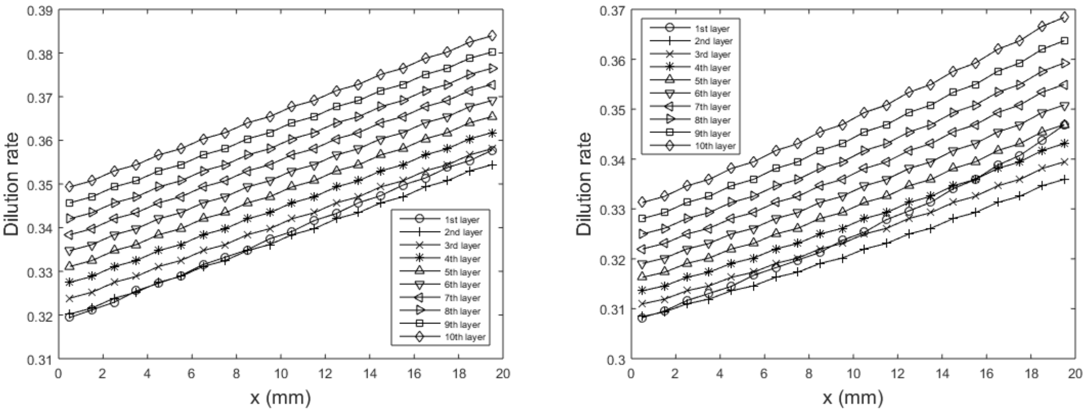

(c) (d)

Fig. 5.14 The volumetric feed rate of (a) Ti-6Al-4V and (b) Inconel 718; (c) the dilution rates for each location, and (d) the dilution rates plot using an alternative mixture rule.

5.3 3D FGM Part Fabrication

In this section, a design method is proposed for DMD fabrication of FGM part with 3D composition variation. The main difference between the 3D case and 1D/2D cases is that the overlapping effect is taken into account, which brings one more dimension of properties variation. The design methodology is presented in Section 5.3.1, followed by a case study in Section 5.3.2 to illustrate the design methodology.

5.3.1 Model Based Design Methodology

5.3.1.1 Overall Framework

The material distribution in an FGM part typically follows a continuous function, and the composition of each material gradually varies spatially. However, the response time of powder composition change has its limitation. Therefore, the distribution function should be discretized to meet the capability of equipment and process variables. For example, in order to obtain an accurate deposition, a faster traveling laser should match up with a shorter response time powder feeder. The composition accuracy also depends on parameters such as the stage control step size, the powder size, and the laser beam dimension. Such issues are to be explored through experiments for each specific equipment, which is not the focus of this research. In this study, the discretized unit cell of the target part is seen as sufficiently small as long as its dimension is less than the laser spot size.

As illustrated in Fig. 5.15, the 3D FGM part being fabricated can be discretized into unit cells, which are arranged by layers and tracks. The substrate is typically composed of a single material, and each layer consists of several tracks. It is assumed that the material composition remains the same within each cell. In this premise, the process parameters can only vary when the laser scans across cells. It can be seen in the cross-sectional view of Fig. 5.15 that dilution effect occurs among adjacent layers and overlapping effect occurs among adjacent tracks within a layer. The shaded areas framed by dotted rectangles represent the mixed/shared portion among layers and tracks. It should be noted that the schematic only shows the concepts of discretization, dilution, and overlapping. For modeling purpose, the cross section of each track is approximated as a circular segment due to the surface tension effect, and so does the cross section shape of the melt pool which is illustrated as dark area in Fig. 5.16 [Pinkerton2004] [Fathi2007] [Cheikh2012] [Urbanic2016].

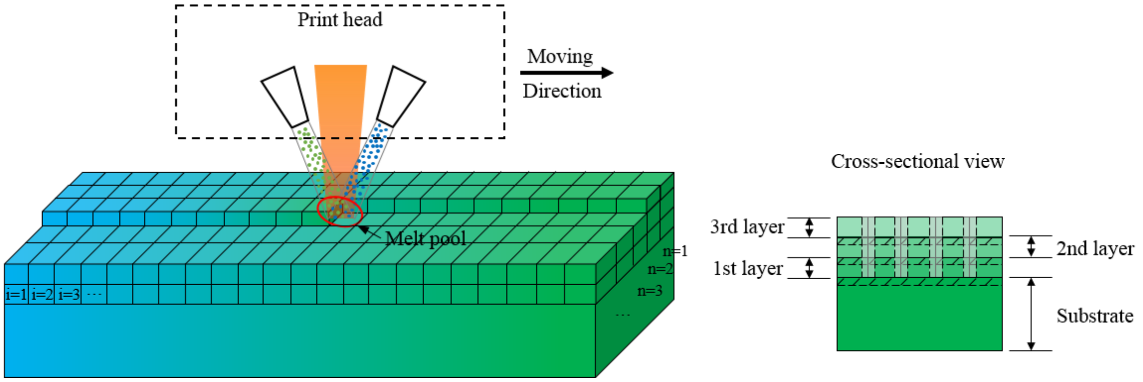

Fig. 5.15 Schematic illustration for part discretization and the dilution/overlapping effect on mixing.

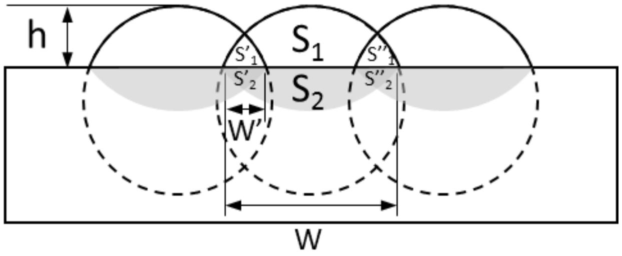

Fig. 5.16 Schematic of the cross section of adjacent tracks.

Taking into consideration the dilution and overlapping effects, the composition of a cell is the resultant of the mixing of the instant powder composition and the composition of the cells beneath it and next to it. As shown in Fig. 5.16, the dilution rate *D* is defined as the ratio of the cross-sectional area of the melted substrate to the total cross-sectional area of the melted substrate (S_2) and the deposited layer (S_1), and the overlapping ratio *O* is defined as the ratio of the overlapped cross-sectional area between two adjacent tracks and the total cross-sectional area of a track. It is assumed here that the mixing between two adjacent tracks only occurs above the substrate since S_2'or S_2'' is negligible comparing with S_2.

$$D = \frac{S_2}{S_1 + S_2} \tag{5.15}$$

$$O = \frac{S_1^{'}}{S_1} or \frac{S_1^{''}}{S_1} \tag{5.16}$$

When determining the composition of the part, the influence of dilution and overlapping should be considered as well as the instantaneous powder composition:

1st layer, 1st track:

$$C^{1,1}_{i,dep} = D \times C^{1,1}_{i,sub} + (1-D) \times C^{1,1}_{i} \tag{5.17}$$

1st layer, 2nd track:

$$C^{1,2}_{i,dep} = D \times C^{1,2}_{i,sub} + O \times (1-D) \times C^{1,1}_{i,dep} + \left[1 - D - O \times (1-D)\right] \times C^{1,2}_{i} \tag{5.18}$$

2nd layer, 1st track:

$$C^{2,1}_{i,dep} = D^{2,1}_i \times C^{1,1}_{i,dep} + \left(1 - D^{2,1}_i\right) \times C^{2,1}_{i,pow} \tag{5.19}$$

2nd layer, 2nd track:

$$C^{2,2}_{i,dep} = D^{2,2}_i \times C^{1,2}_{i,dep} + O \times \left(1 - D^{2,2}_i\right) \times C^{2,1}_{i,dep} + \left[1 - D^{2,2}_i - O \times \left(1 - D^{2,2}_i\right)\right] \times C^{2,2}_{i,pow} \tag{5.20}$$

where $C^{1,2}_{i,dep}$ and $C^{1,2}_{i,pow}$ represents the deposition composition and the instantaneous powder composition of element *i* in the first layer second track respectively; $C_{i,sub}$ is the concentration of element *i* in the substrate; $D^{2,1}_i$ represents the dilution rate between the element *i* in the second layer first track and the element below it. In general, the concentration of any element *i* in a certain layer *m* and track *n* is given by:

$$C^{m,n}_{i,dep} = D^{m,n}_i \times C^{m-1,n}_{i,dep} + O \times \left(1 - D^{m,n}_i\right) \times C^{m,n-1}_{i,dep} + \left[1 - D^{m,n}_i - O \times \left(1 - D^{m,n}_i\right)\right] \times C^{m,n}_{i,pow} \tag{5.21}$$

$$O = 0 \; if \; n = 1$$

In the above equations, the overlapping ratio *O* has no superscript or subscript since it is always controlled to a constant in this study. The width of the track *W* should be controlled to a constant value in order to obtain a uniform and better controlled deposition. As can be seen in Fig. 5.16, when a second track is deposited, a portion of it is mixed with the previous track. The overlapping distance between two adjacent tracks should also be maintained at a certain value *W'*, and the calculation procedure is discussed later in Section 5.3.1.2. The dilution ratio *D* is given by Eq. (5.4). For a 3D case, the melting efficiency is estimated by the following equation [Okada1977]:

$$\eta_m = \frac{e}{2}\left[1+\sqrt{1+\frac{2.6}{\left(\frac{VW}{2\alpha}\right)^2}}\right]^{-1} \tag{5.22}$$

where e represents the base of natural logarithm; V denotes the laser scanning speed; and α is the thermal diffusivity, which depends on the composition of the substrate. It can be seen from Eqs. (5.4) and (5.22) that the dilution rate varies spatially, since ΔH_s, ΔH_p, and α are all functions of the substrate composition. The substrate herein refers to any layer on top of which the new layer is being deposited.

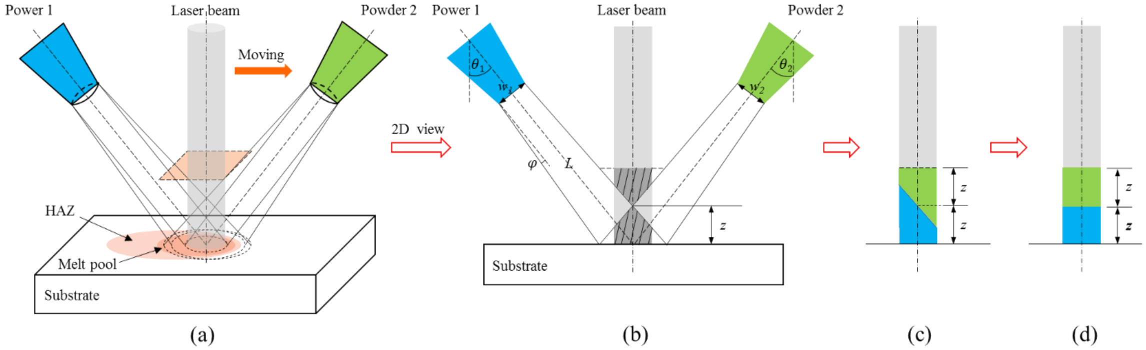

Fig. 5.17 Conversion process of the powder shadowing effect.

Same as the 2D parts fabrication, the laser attenuation can be calculated using Eq. (5.7). In this study, the laser attenuation due to powder shadowing effect can be calculated following the conversion process illustrated in Fig. 5.17. Given a laser beam with a square spot, the shadowing effect occurs within the laser-powder interaction space.

We assume that the powder injection angles are θ_1 and θ_2, the powder jet divergence angle is φ, and the diameters of the nozzles are w_1 and w_2, the laser intensity follows a Gaussian distribution with the radius r at waist:

$$I = \frac{P}{\pi r^2}\exp\left[-\frac{f\left(x - Vt\right)^2}{r^2} - \frac{f y^2}{r^2}\right] \tag{5.23}$$

where f is the shape factor which is set to 3 in this study. To simplify the analytical expression, the nozzles are made as having the same injection angles ($\theta_1 = \theta_2$), and the diameters of the nozzles are the same ($w_1 = w_2$). As shown in Fig. 5.17 (b) and (c), when flipping the lower shadowed region that only consists of powder 2, the laser-powder interaction space is converted within a cuboid space where the laser beam passes two trapezoidal regions of two powders respectively. Then, assuming the attenuation is constant at a specific time, Fig. 5.17 (c) can further be equated to Fig. 5.17 (d), where the laser beam passes two rectangular regions of two powders respectively. Eq. (5.21) can be rewritten as:

$$P = \eta_l \exp\left[-\frac{3\left(1-\eta_{l1}\right)}{2r_{p1}\rho_{p1}}\cdot\frac{\dot{V}_{p1}\rho_{p1}}{\pi\left(\frac{w}{2}+L\tan\varphi\right)^2 v_{p1}}\cdot z - \frac{3\left(1-\eta_{l2}\right)}{2r_{p2}\rho_{p2}}\cdot\frac{\dot{V}_{p2}\rho_{p2}}{\pi\left(\frac{w}{2}+L\tan\varphi\right)^2 v_{p2}}\cdot z\right]P_0$$

$$\text{and}\quad z = \frac{L\sin\varphi}{sin\left(\theta+\varphi\right)} + \frac{w}{2\sin\theta} \tag{5.24}$$

The above equation gives a relationship between the attenuated laser power and the laser power actually applied or the initial laser power (and so does the attenuated laser intensity and the initial laser intensity, e.g. $I = \eta_a I_0$). In the design process, the attenuated laser power should be known first based on the required melt pool width W, whose prediction process is discussed later in Section 5.3.1.3.

The last point to note about Eq. (5.4) and (5.22) is that the values for the properties ΔH_s, ΔH_p, and α are calculated following the mixture theory in Eq. (5.9) and (5.10).

5.3.1.2 Determining the Overlapping Width W'

The overlapping width is a critical parameter for 3D parts fabrication rather than single-tracked thin-walled parts fabrication. In order to obtain a flat surface for each layer, the amount of materials to fill up the "gap" between two adjacent tracks due to their circular-shaped cross sections need to be considered. Thus, according to mass conservation, the regions represent the overlapped materials above and below the substrate surface (S_1' and S_2') should compensate for the groove between two tracks (S_3), as illustrated in Fig. 5.18 (a). It is assumed here that S_2' is also negligible comparing with S_1', so the following equation should be satisfied instead:

$$S_1^{'} = S_3 \tag{5.25}$$

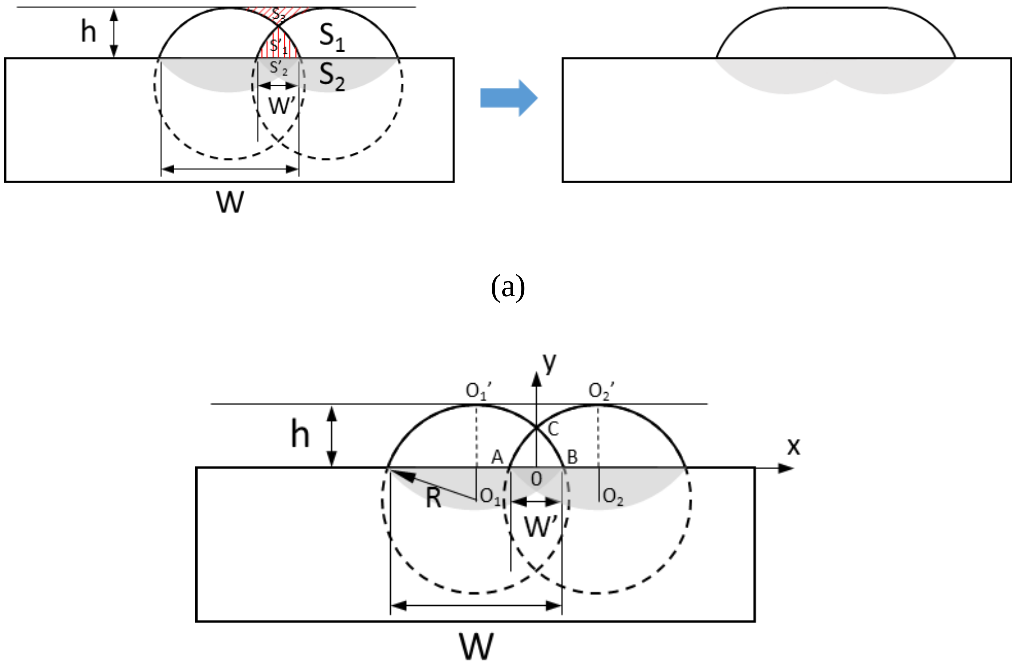

(a)

(b)

Fig. 5.18 Illustration for overlapping ratio determination.

The geometrical parameters for two adjacent deposition tracks are shown in Fig. 5.18 (b): O_1 and O_2 are the centers for the circular segments (with radius R) above the substrate surface; O_1' and O_2' are the highest points for the circular segments. The cross section area of the layer (S_1) is dependent on the powder volumetric feed rate $S_1 = \frac{\eta_d \dot{V}_p}{V}$, and R can be obtained by solving the equation [Cheikh2012]:

$$\frac{\eta_d \dot{V}_p}{V} = \frac{1}{6W} R \left[1 - \sqrt{1 - \left(\frac{W}{2R} \right)^2} \right] \left\{ 3R^2 \left[1 - \sqrt{1 - \left(\frac{W}{2R} \right)^2} \right]^2 + 4W^2 \right\} \tag{5.26}$$

Then, the layer height h can be obtained knowing R:

$$h = R\left(1 - \sqrt{1 - \left(\frac{W}{2R}\right)^2}\right) \tag{5.27}$$

Geometrical analysis gives the equation for circle O$_1$:

$$\left(x - \frac{W' - W}{2}\right)^2 + \left(y - h + R\right)^2 = R^2 \tag{5.28}$$

$$y = \sqrt{R^2 - \left(x - \frac{W' - W}{2}\right)^2} + h - R \tag{5.29}$$

Consequently, S$_1$' can be calculated using integration approach:

$$S_1^{'} = 2\int_0^{\frac{W'}{2}} \left[\sqrt{R^2 - \left(x - \frac{W' - W}{2}\right)^2} + h - R\right] dx \tag{5.30}$$

The geometrical relationship illustrated in Fig. 5.18 (b) provides a way to express S$_3$ with the aid of the rectangular area O$_1$O$_2$O$_2$'O$_1$', and combining Eq. (5.25):

$$S_1^{'} = S_3 = h\left(W - W'\right) - S_1 + S_1^{'} \tag{5.31}$$

where $S_1 = \frac{\eta_d \dot{V}_p}{V}$. Then Eq. (5.31) becomes:

$$h\left(W - W'\right) = \frac{\eta_d \dot{V}_p}{V} \tag{5.32}$$

where the overlapping length W' can be solved. Combining Eq. (2) and $S_1 = \frac{\eta_d \dot{V}_p}{V}$, the overlapping ratio is determinable.

The above calculation procedure for W' is under the premise that

$S_1 = \frac{\eta_d \dot{V}_p}{V} < \frac{\pi W^2}{8}$, meaning that the cross-sectional area of the layer is smaller than a half circle. This is preferred because it is more stabilized than a circular segment which has an area larger than a half circle when subject to disturbance during the fabrication process. Also, porous structures are less likely to form with this condition.

5.3.1.3 Determining the Melt Pool Width W

Both critical parameters, the dilution rate and the overlapping ratio, are dependent on the melt pool width W, which can be found in Eq. (5.22) and Eqs. (5.26) to (5.32). In order to get a desired melt pool width, the laser parameters need to be tailored in accordance with the substrate composition. The laser parameters include the power *P*, the spot radius *r*, and the scanning speed *V*.

To enable a high quality manufacturing, the width of each building track should be controlled to a constant value, and so does the melt pool width. The target melt pool width is predefined at a constant value. Therefore, the relationship between the melt pool width and the process parameters (including the operating conditions and the substrate composition) should be found. In the substrate heating model, the laser is modeled as a surface heat flux as heating the substrate:

$$\rho c_p \frac{\partial T}{\partial t} + \rho c_p V \cdot \nabla T = \nabla \cdot \left(k \nabla T \right) \tag{5.33}$$

where ρ, c_p, and k are the density (kg/m^3), specific heat (J/(kg·K)), and thermal conductivity (W/(m·K)) of the substrate material respectively; T is the substrate temperature (K), and t is time (s). The boundary conditions are:

$$T(x, y, z, 0) = {}_{\infty} \tag{5.34}$$

$$T(x, y, z, \infty) = {}_{\infty} \tag{5.35}$$

$$-k\left(\nabla T \cdot \vec{n}\right) = \begin{cases} \eta_a I_0, & \text{on laser spot region} \\ \eta_a I_0 - h_c\left(T - T_\infty\right) - \varepsilon\sigma\left(T^4 - T_\infty^4\right), & \text{on substrate lateral and top surfaces} \\ 0, & \text{on substrate bottom surface} \end{cases} \tag{5.36}$$

where T_∞ is the ambient temperature which is 293 K; $\vec{n}$ is the normal vector of the substrate; ε denotes the emissivity of the substrate; σ denotes the Stefan-Boltzmann constant (5.67×10^{-8} W/(m^2·K^4)); and h_c represents the heat transfer coefficient. In order to reduce the computation time, a combined heat transfer coefficient is used to incorporate both convective and radiative boundary conditions based on the equation given by [Goldak1984]:

$$h_c = 2.4 * 10^{-3} \varepsilon T^{1.} \tag{5.37}$$

and h_c is seen as a constant which is calculated using a temperature at around the middle point of the temperature range in the system. The equivalent latent specific heat is:

$$C_p^* = C_p + L_f \frac{\partial \alpha_m}{\partial T}$$

$$\text{and} \quad \alpha_m = \frac{1}{2} \frac{(1-\gamma)\rho_{liq} - \gamma\rho_{sol}}{\gamma\rho_{sol} + (1-\gamma)\rho_{liq}} \tag{5.38}$$

where L_f is the latent heat of fusion, γ is the fraction of solid phase, and ρ_{sol} and ρ_{liq} represent the density of solid and liquid phases respectively. In this simulation, the following main assumptions are made: (1) the effects of fluid motion due to forces such as Darcy force, capillary force and Marangoni force are not considered here; (2) the material properties of the substrate are constants, and the values of thermal conductivity and specific heat are chosen at around half of the melting/liquidus temperature of each material to increase the modeling accuracy; (3) the phase change from liquid to gas is not included since the appearance of vaporization is not preferred during the process, and this can be examined by the maximum temperature on the substrate; (4) the melt pool boundary is defined by the liquidus isothermal line on the substrate when the size of the melt pool is stabilized.

During the fabrication of an FGM part, the process parameters should be tailored over time since the composition is changing spatially. To enable a high quality manufacturing, the width of each building track should be controlled to a constant value, and so does the melt pool width. The laser spot size is fixed to a constant value, and the melt pool width is a function of a group of independent variables: the laser scanning speed, the laser power (or laser intensity), the density, thermal conductivity, thermal diffusivity, latent heat of fusion, solidus and liquidus temperatures of the substrate. However, most of these parameters are correlated since the properties of the substrate are computed following rule of mixture (Eq. 5.9).

In this study, a prediction method using the artificial neural network (ANN) is adopted. Due to the correlation of the independent variables, we can reduce the number and select only the laser power (*P*), the laser scanning speed (*V*), and the substrate concentration (*C*) as independent variables for determining the melt pool width (*W*). To find a relationship among the four variables, multiple simulations are run on the FEA software COMSOL Multiphysics® by alternating the process parameters. Then, an ANN is developed using the simulation results to predict any one of the variables using the other three. In the design study, the melt pool width is fixed. To reduce the degrees of freedom of the problem, either the laser power or the laser scanning speed should be fixed, and only one of them is allowed to be changeable during the fabrication process.

5.3.1.4 Design Flowchart

A general flowchart for the design process is shown in Fig. 5.19 to summarize the design method described above. The flowchart shows the case in which the laser power is required to be fixed. In this flowchart, the variables circled in solid frames are prescribed by designers, and the variables in dark frames are the main target variables. The conditions at the starting point of an arrow represent the known variables, while the conditions at the ending point of an arrow represent the deduced variables. The variable

P_test represents the test laser power, while the variable *P_fix* represents the fixed laser power. This is based on the case that we fix the laser power while vary the scanning speed during the fabrication, similarly for the case when the scanning speed is fixed while varying the laser power. To reduce the redundancy of the flowchart, each variable dos not appear more than once. Any deduced variable is not necessarily only obtained from the known variables that are most close to it, but also the known variables above it. For example, the powder feed rate $\dot{V}_{pi}^{m,n}$ is calculated by knowing the scanning speed $V_i^{m,n}$, the layer height h, the deposition efficiency η_d, as well as the melt pool width W. Here, the fixed laser power *P_fix* is not used while the melt pool width W is used. The local loop exists in the flowchart represents a checking process, which will be discussed in later sections. Following the flowchart, the operating parameters can be planned as a function of space, according to the design requirements.

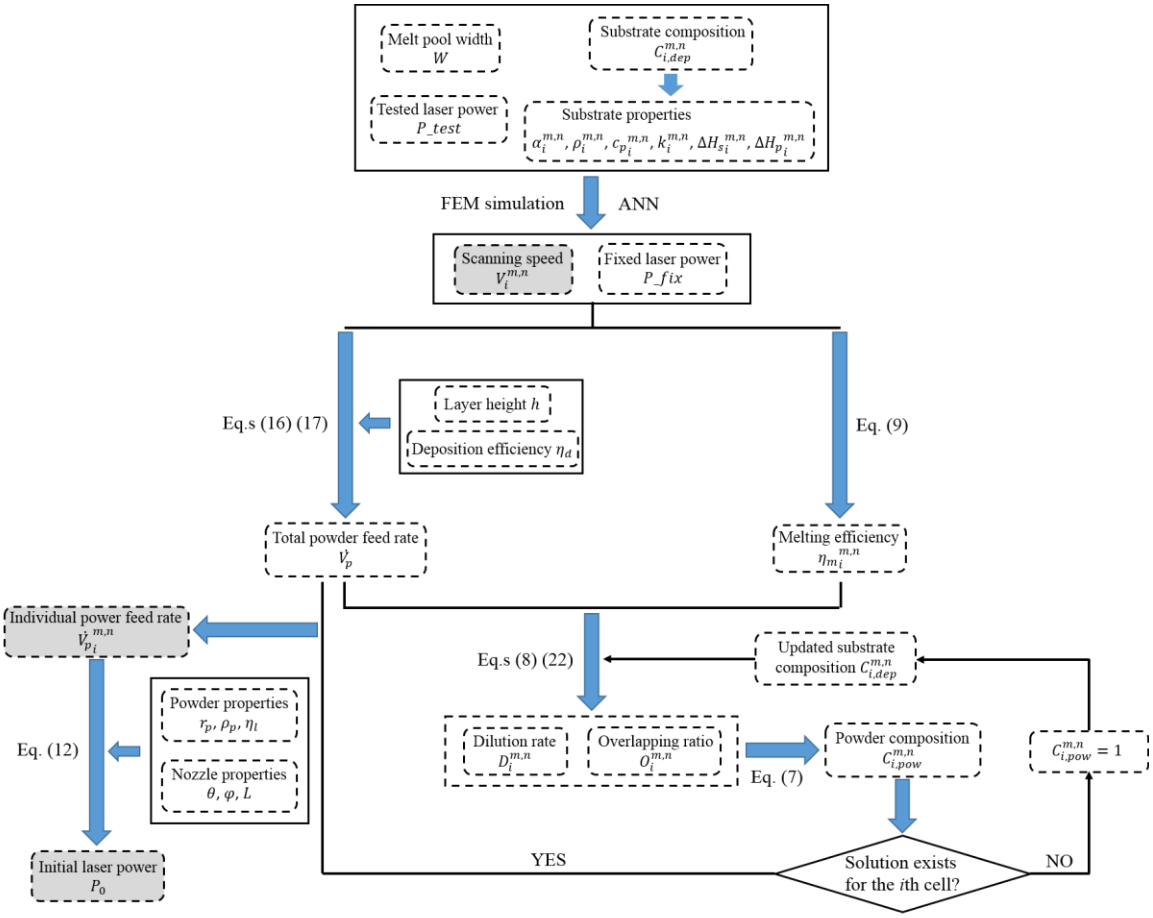

Fig. 5.19 Design flowchart for 3D FGM parts.

5.3.2 Case Study

In this section, the design methodology and calculation procedure is presented in a case study to help better understand the process and physics of the DMD fabrication of FGM parts. It should be mentioned in advance that the proposed design methodology is applicable to any FGM system consists of multiple metals or alloys if known their phase diagrams. For this case, Iron and Nickel are selected as building materials.

5.3.2.1 Problem Description

The objective of this case study is to fabricate an FGM part with dimension 20 mm × 10 mm × 6 mm, as shown in Fig. 5.20. The component materials are Fe and Ni. For convenience, the concentration in this study is always specified to Ni. The concentration distribution function of the desired part is:

$$C = 0.2 + 0.2 \times \left(\frac{x}{L_x} + \frac{y}{L_y} + \frac{z}{L_z}\right) \tag{5.39}$$

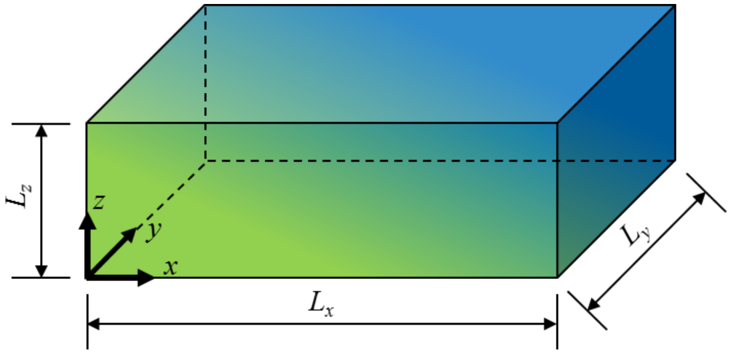

Fig. 5.20 The objective FGM part with 3D concentration variation.

Consequently, the concentration for Fe is (1-*C*). It can be seen that the part composition varies in three directions, with the origin has the lowest (Nickel) concentration of 0.2 and the diagonal corner has the highest (Nickel) concentration of 0.8. To fabricate the part, an initial substrate should be selected on which the first layer start to build. Practically, a block/plate of pure material (either Fe or Ni) is used as the initial substrate. In this case, a Ni substrate is used since Ni is easier to melt than Fe. It should be noted that it is not necessary to fabricate the part following the direction shown in Fig. 5.20, with *x*-*y* plane parallel to the initial substrate. However, fabricating the part with *y*-*z* plane parallel to the initial substrate may employ more number of layers, increasing the manufacturing time. Yet, the dependence of manufacturing direction on part quality is beyond the scope of this study, and future work may include this aspect. In the design process, the manufacturing direction is chosen as in Fig. 5.20.

To fabricate such an FGM part, the in situ powder injection approach is used so that Ni and Fe powders can be mixed in the melt pool with certain mixing ratio. The flow rate of the two powders is controlled by the system. The problem requires either a constant laser power or a constant laser scanning speed during the fabrication process. Both requirements are discussed and design variables are calculated respectively. The main design objectives include the scanning speed (or the laser power), and the feed rates of the two types of powders.

5.3.2.2 Set the Constant Parameters

The physical and thermal properties of the substrate mixed by two materials are calculated following the rule of mixture, using the individual properties of Fe and Ni listed in Table 5.2. As an exception, the solidus and liquidus temperatures of the mixture does not follow the rule of mixture, since the two metals form a eutectic system, lowering the liquidus temperature. It can be seen from the Fe-Ni phase diagram in Fig 5.21 that the eutectic temperature is 1436 ºC at 68% (Ni, at. %). The melting point of the mixture is described by the liquidus temperature of the system, which is approximated using a three point second degree polynomial fit. It can be seen from Fig. 5.21 that the solidus and liquidus lines are almost coincide in a large range, and the distance of the two lines is estimated as always 5 ºC.

$$T_{melt} = 0.0228 \times C^2 - 3.11 \times C + 1811 \left(K \right) \tag{5.40}$$

Table 5.2 Individual properties of Fe and Ni.

Property	Fe	Ni
Laser absorptivity, η_l	0.3	0.3
Emissivity, ε	0.4	0.4
Density, ρ (kg/m^3)	7870	8908
Specific heat, c_p (J/kg/K)	450	440
Thermal conductivity, k (W/m/K)	76.2	49.5
Thermal diffusivity, α (m^2/s)	2.15×10^{-5}	1.26×10^{-5}
Melting point, T_{melt} (K)	1811	1728
Melting enthalpy, ΔH (J/mm^3)	2.125	2.646
Latent heat of fusion, L_f (kJ/kg)	270	297

The melt pool width W and the layer height h are the critical parameters that determine the deposition resolution/accuracy. In this case, the melt pool width W is preset at 0.4 mm, and the layer height h is preset at 0.15 mm. As discussed before, the layer height h should have a value less than or equal to W/2, since the cross-sectional area of a layer should be smaller than a half circle. Some other parameters that need to be preset or predetermined according to equipment/experiment condition. In this case, these parameters are preset and are selected according to commonly used values (Table 5.3). The range for the laser power is chosen between 500 W and 1500 W, and the range for the laser scanning speed is between 10 mm/s and 50 mm/s. These parameters are determined by considering also the manufacturing requirements. For example, the laser spot radius is set at 0.3 mm accounting for the melt pool width 0.4 mm. A larger spot size would be selected if a lower resolution (larger melt pool width) is required. The operating parameters for both materials are set as equal, but they can be different when considering situations such as particles in-flight heating, as discussed in our previous work [Yan2016]. It should be noted that these parameters are preset for the initial design calculation process, and are adjustable in the design process. Final proper values of these parameters may be obtained through iteration or trial and error process.

Table 5.3 Preset process parameters.

Preset process parameter	Value
Laser absorptivity, η_l	0.3
Powder radius, r_p (μm)	10
Powder injection speed, v_p (m/s)	10
Injection angle, θ (º)	30
Injection nozzle diameter, w (mm)	2
Powder beam divergence angle, φ (º)	5
Distance between the nozzle center and the laser spot center, L (mm)	10
Laser spot radius, b (mm)	0.3

5.3.2.3 Determine the Laser Scanning Speed and Laser Power by ANN

The first step of the calculation procedure is to determine the laser scanning speed and the laser power. The ANN has been demonstrated to be a powerful tool to model, predict, and control manufacturing processes, such as the laser cladding or DMD process [Guo2013] [Nenadl2014] [Saqib2014]. Using a trained ANN, one of these two variables can be predicted as a function of space or the desired part composition, while fixing the other variable. To develop a proper neural network, a set of testing samples (Table 5.4) by varying the three critical process parameters are run on the FEM software COMSOL Multiphysics® to generate the melt pool width data.

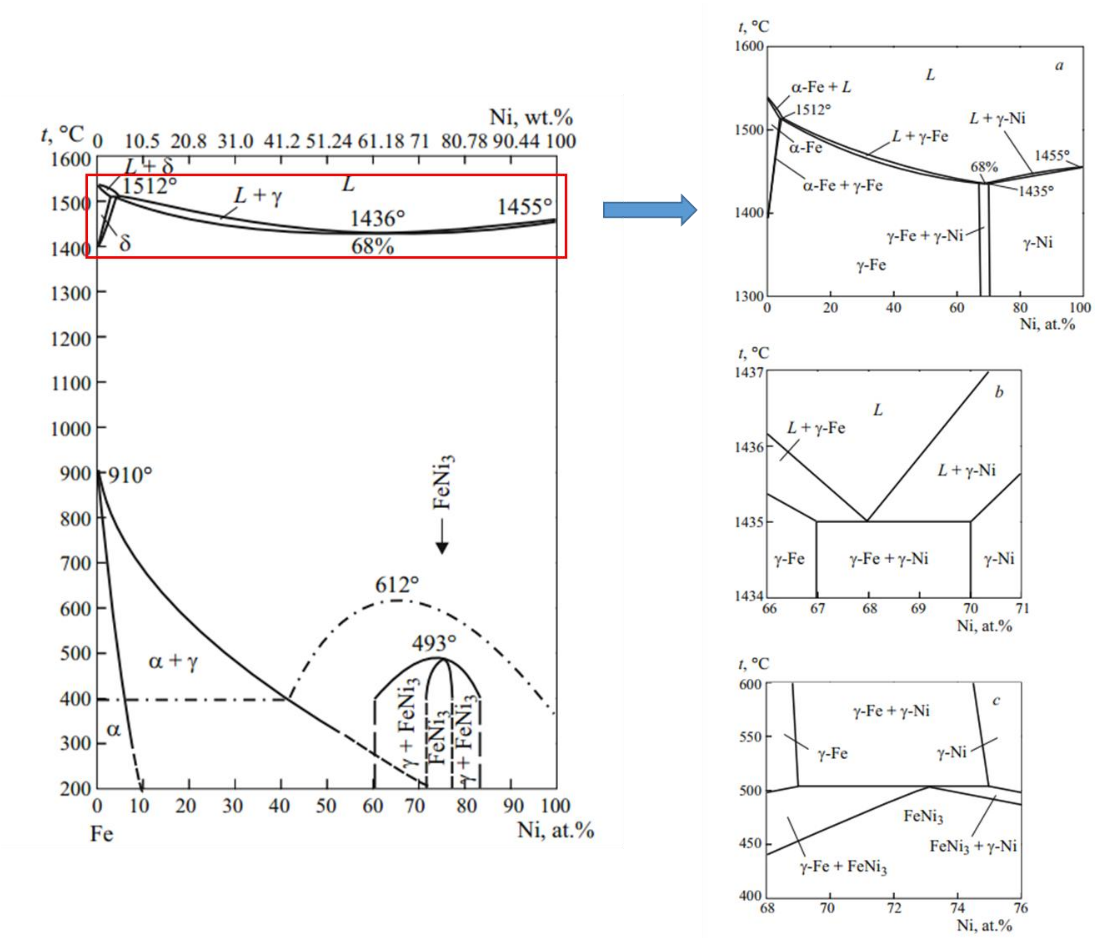

Fig. 5.21 Phase diagram of Fe-Ni system [Silman2012].

Table 5.4 Testing values of the critical process parameters.

Variable for ANN test	Range	Step	No. of values
Laser power, *P* (W)	500 - 1500	100	11
Scanning speed, *V* (mm/s)	10 - 50	10	5
Substrate composition, *C*	0 - 1	0.2	6

The calculation domain for the simulation has a dimension of 20 mm × 4 mm × 1 mm, and Fig 5.22 (a) shows the half space due to symmetry. The convection heat transfer coefficient h_c is approximated as a constant 65 W/(m·K) using Eq. (5.37). Free tetrahedral mesh is used and the maximum element size is set at 0.05 mm to 0.1 mm. The time dependent calculation is performed with laser beam scanning on top of the substrate for 18 mm to minimize the boundary effect. The time step for each simulation is set at 0.02 second. The melt pool width is calculated by taking the average of the melt pool width at three equal-spaced points on the surface of the calculation domain. The three points are selected when the maximum temperature on the substrate is stabilized, as shown in Fig. 5.22 (b). The total number of the testing samples is 330 (11×5×6), and within these data sets 179 are reserved for training, validating, and testing of the neural network. The eliminated data are those that represent the cases of substrate boiling (maximum temperature exceeds the boiling temperature) and no melt pool formation (maximum temperature lower than the melting temperature).

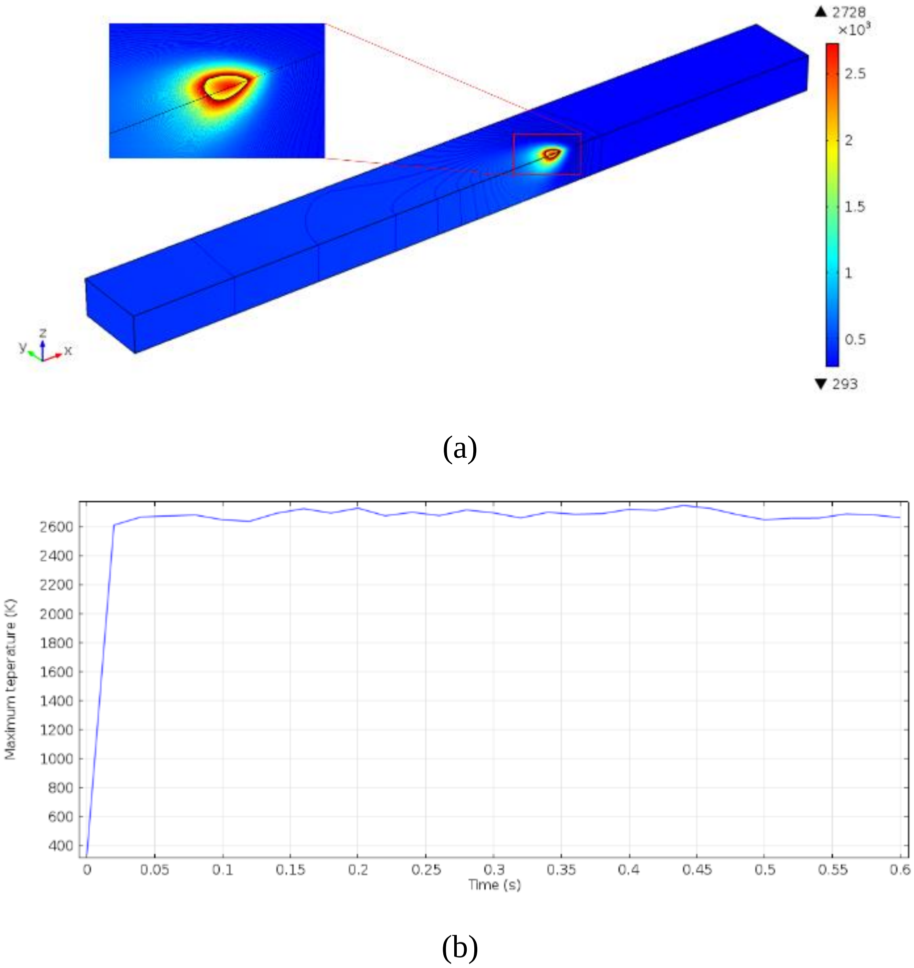

Fig. 5.22 (a) Example calculation result (*C* = 1, *P* = 800W, *V* = 30mm/s at *t* = 0.4 s) illustrating the temperature distribution on half calculation domain, and (b) the evolution of the maximum temperature.

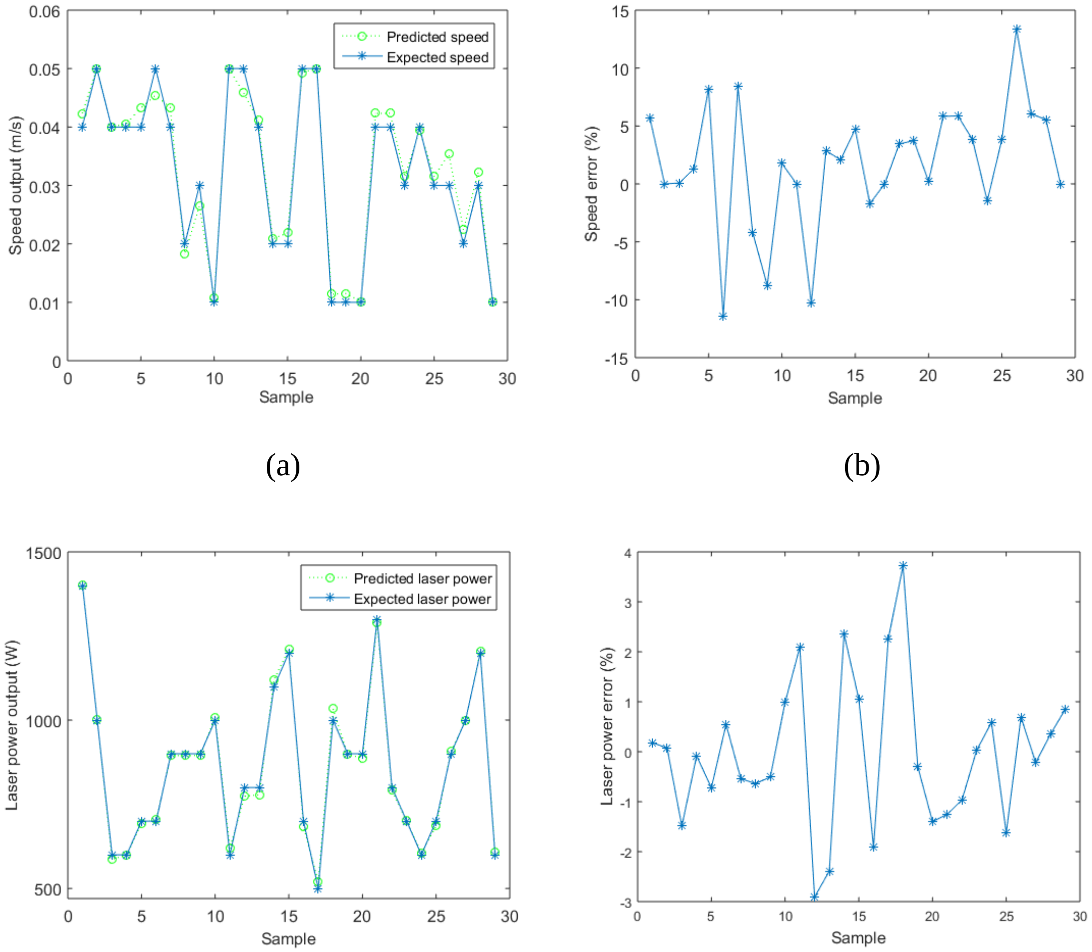

(a) (b)

(c) (d)

Fig. 5.23 Typical ANN testing results for prediction: (a) expected and predicted laser scanning speed, (b) laser scanning speed prediction error, (c) expected and predicted laser power, and (d) laser power prediction error.

To understand the relationship among the four variables (*P*, *V*, *C*, and *W*), a backpropagation (BP) neural network is created, which has three inputs and one outputs.

Therefore, the number of hidden layer is set to one. The number of nodes in the hidden layer is selected as 5 by trial and error approach, i.e., varying the number from 1 to 10 and select the one with the best prediction. The data set is normalized before entering the ANN in order to render the scale of the data uniform and to increase the accuracy of the network. The transfer function used is the hyperbolic tangent function ‘tansig’. The Levenberg-Marquart backpropagation is used as training algorithm. The learning rate is set at 0.05; the minimum error is 0.001; the maximum validation failure is 6; the minimum performance gradient is 10^{-6}. The neural network is used to predict any one of the four variables by considering the other three as input/known variables. Among the 179 data sets, about 85% (150 samples) are randomly selected to train and validate the neural network, while the rest about 15% (29 samples) serve to test the trained network. To increase the accuracy and speed of the network, the data sets are normalized before training and validating phase. The errors of the output is defined as follows:

$$error = \frac{BP\,output - true\,value}{max\left(true\,value\right) - min\left(true\,value\right)} \times 100\% \tag{5.41}$$

The difference of the maximum and minimum among the true target values is used as the numerator to eliminate the influence of the target value’s magnitude.

The ANN prediction results for both cases are shown in Fig. 5.23. First, the laser scanning speed is predicted using the laser power, the substrate composition and the melt pool width. The typical error can be controlled within 15%. Then, the laser power is seen as output variable while the laser scanning speed, the substrate composition and the melt pool width are input variables. The prediction error is typically below 5%, which is better than the former case. However, which parameter is changeable during the fabrication process depends on experimental conditions.

The performances of the developed ANN are shown in Fig. 11 and Fig. 12. It can be seen that the R values (coefficient of correlation) for both cases are above 0.97, demonstrating a good prediction using the network. For the case when using the ANN to predict the laser power, the R value is typically around 0.99 or even better. Same kind of trend is also obtained for the case of predicting the laser power, where the R value is typically around 0.99 or even better, as shown in Fig. 5.24 (b). The error plots for the predicted laser scanning speed and laser power are shown in Fig. 12. The MSE (Mean Squared Error) values for both cases are below 0.1, however, the MSE value is even lower for the case when using the ANN to predict the laser power. Same kind of trend is also obtained for the case of predicting the laser power, where the best MSE value can be smaller than 0.01. Same kind of trend is also obtained for the case of predicting the laser power, where the best MSE value can be smaller than 0.01, as shown in Fig. 5.25 (b).

As mentioned before, either the laser power or the scanning speed is to be fixed before the main calculation procedure, in order to reduce the number of changing variables during the fabrication process. Both parameters can be fixed to any value within their ranges shown in Table 5.4 practically. However, a decent value for one parameter would not require the other parameter to be set near its limits. For example, fixing the laser power at extremely low (500 W) or high (1500 W) value would limit the selection freedom of the scanning speed. Therefore, after examining the simulation data set, 900 W is chosen as the fixed laser power and 20 mm/s is chosen as the fixed scanning speed. It should be noted that there are a variety of other couples of feasible selections such as 1000 W at 40 mm/s, and 1100 W at 50 mm/s.

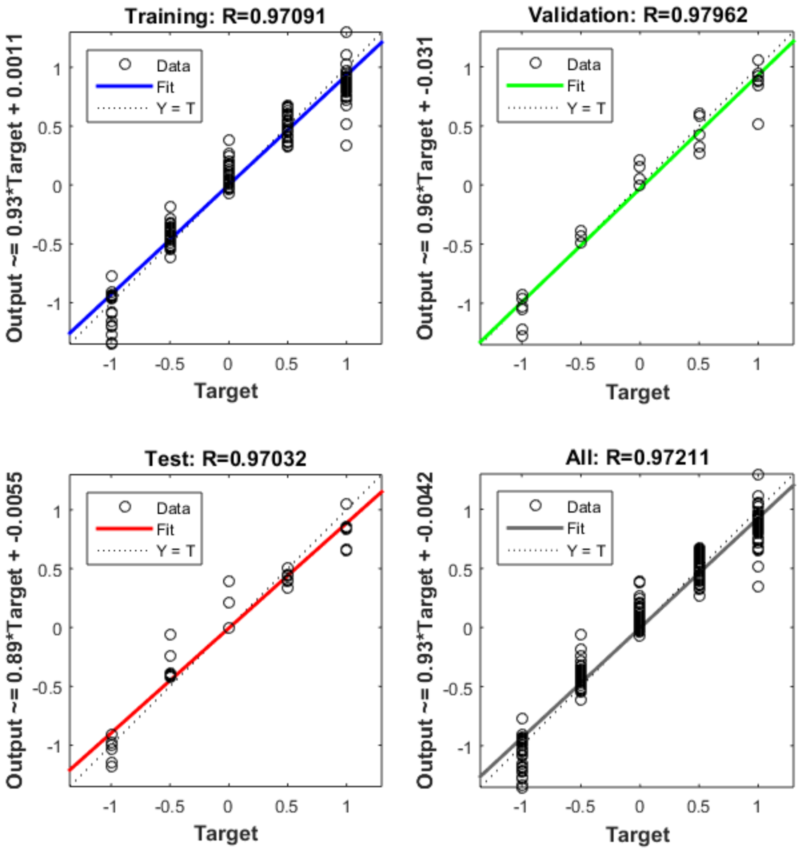

(a)

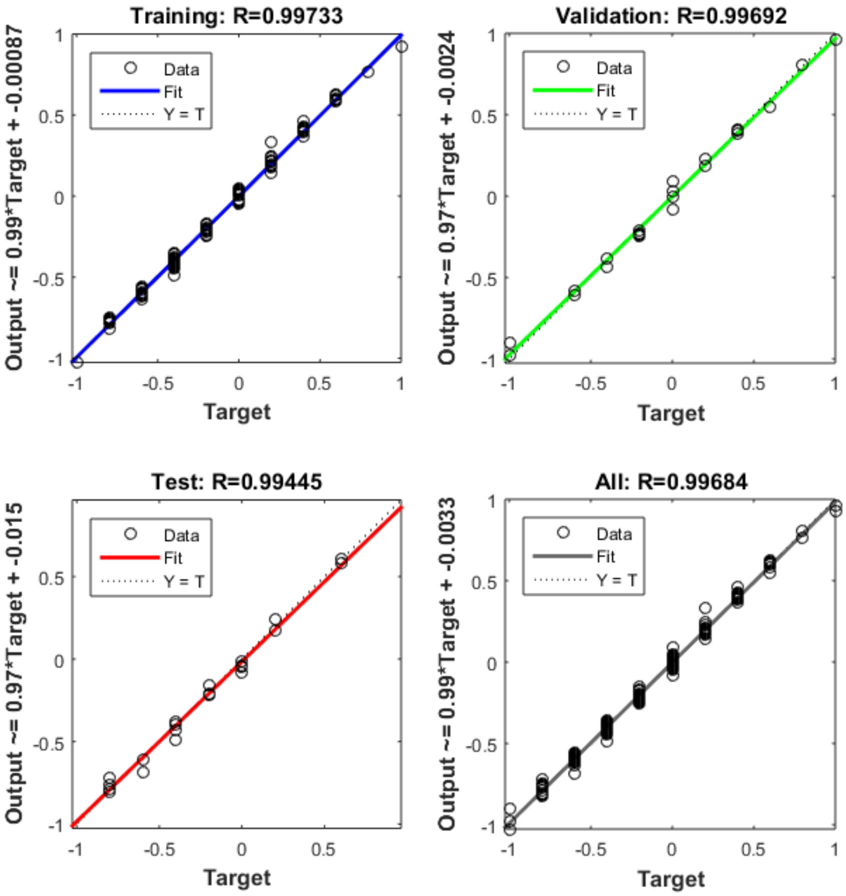

(b)

Fig. 5.24 Regression analysis for ANN performance.

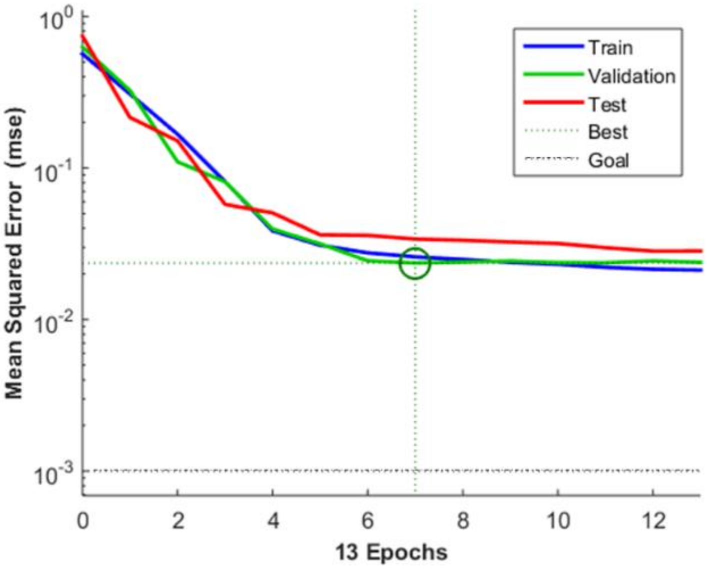

(a)

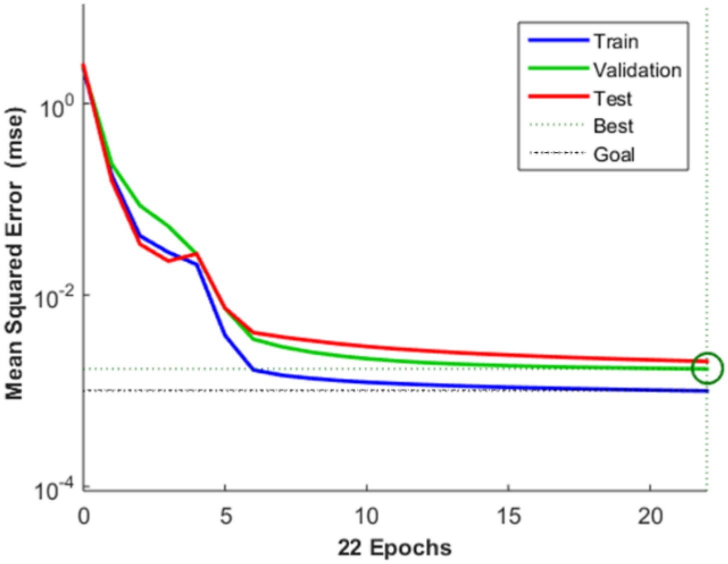

(b)

Fig. 5.25 Variation of total error with number of epochs when using ANN to predict the (a) laser scanning speed, and (b) laser power.

5.3.2.4 Determine the Changing Parameters

The changing parameters that vary spatially include the feed rate of each powder, and the scanning speed or the laser power, depending on which one is fixed. The calculation process basically follows the flowchart shown in Fig. 5.19. However, some details need to be explained here, and the results and discussions for the two cases are presented respectively.

Among the preset parameters, the deposition efficiency η_d is estimated as no higher than $\frac{w}{2r}\left(=0.3\right)$. This estimation is based on the assumption that the particles are evenly distributed in the powder jets. Practically, this number can be a bit higher, since the distribution of powder is basically Gaussian or other center-concentrated shapes. The deposition efficiency also depends on other factors, such as the feed gas speed, the geometry design or the distribution of the injection nozzles, which has been studied and discussed in our previous work [Yan2016b]. Although the goal is to fabricate an FGM part with smooth transition of materials, spatial discretization is needed when comes to the real manufacturing process. The changing parameters are tuned according to the design requirements in a discrete or step-by-step manner due to the nature of the digital control of machines. The actual manufacturing resolution depends on parameters such as the control step size, the melt pool size, the powder particle size, and the laser scanning speed. The discretized cell volume should be sufficiently small compared to the target

FGM part. In this case study, the dimension of a cell in the *x* direction is set at 1 mm, and the dimensions in the *y* and *z* directions are equal to the melt pool width multiply the overlapping ratio (W×O) and the layer height (h) respectively. Hence, the material composition remains the same within each cell, and the process parameters only change when the laser scans past a cell.

When determining the number of tracks in one layer, the following equation should meet:

$$W+\left(j-1\right)\left(W-W'\right)\geq L_y \tag{5.42}$$

where *j* is the number of tracks in one layer. The solution for *j* is taken as the minimum integer that satisfies Eq. (5.42). The results based on the proposed design method are shown in three different scenarios:

Setting the laser power as constant

In this situation, the laser power is set at constant 900 W throughout the fabrication process, allowing only the scanning speed to change. According to Eq. (5.32), the overlapping ratio is a function of the laser scanning speed. Moreover, the scanning speed is a function of the melt pool width, the laser power, and the substrate composition using ANN prediction. Since the initial substrate is pure Ni (C = 1), the scanning speed for the first layer is always a constant. Consequently, the dilution rate is also a constant for the first layer deposition. In this premise, problem may raise that the initial couple of layers cannot be at accurate composition as desired. Suppose the situation that the desired concentration of the cell at the very beginning is 0.2, but the dilution rate is always 0.3 at the first layer. This means that the desired composition can never be reached even the injected powder consists of only Fe. In other words, the lowest concentration that can be reached at the first layer is equal to the dilution rate value. Therefore, the composition of a newly deposited track should be examined after the calculation of one track. If the desired composition is not met at a specific layer, then a new layer should be added above, following the same composition requirement. This iterative calculation process keeps going. The key issue is that the initial substrate concentration is high, once the desired composition is met at all points within an entire layer, there is no need for further examination since the composition is smoothly graded. Finally, the initial couple of layers that do not meet the desired composition should be cut off at the end of the whole process.

When calculating the dilution rate, the equivalent laser power is used instead of the preset 900 W laser power. The equivalent laser power is defined as a uniform laser which has the equal total energy throughout the beam as the given Gaussian laser, and the equivalent laser power P_{equal} is calculated as 285.1 W following Eq. (5.43):

$$\pi r^2 P_{equal} = 4\int_0^r \int_0^{\sqrt{r^2-x^2}} P\cdot exp\left[-\frac{f\left(x-Vt\right)^2}{r^2}-\frac{fy^2}{r^2}\right]dzdx \tag{5.43}$$

The calculation resolution for material concentration is first set at 0.001. The Matlab program runs for about 3 hours. The predicted scanning speed for the first layer is 32.8 mm/s using the developed ANN. The start layer is 58, which means that the initial 57 sacrificial layers (8.55 mm) should be removed after deposition. The calculated results are saved into a 20×34×40 matrix, containing the information for the scanning speed at different location, as well as the varying initial laser power, powder concentration, and dilution rate. The powder concentration (comparing with the desired concentration) and the required laser scanning speed at the 20th layer, 15th track is shown in Fig. 5.26. The powder concentration is always larger than the required concentration, which is understandable since the part's concentration is increasing in all the three directions (Eq. (5.39)) and the desired concentration at a certain point is the result of the mixing among the concentration of the powder, the sub-track, and the adjacent track. To build this track, the scanning speed increases from about 12.5 mm/s to 15 mm/s, since Ni concentration increases along the track and the substrate becomes easier to melt. In order to maintain a constant melt pool width, the scanning speed should also increase.

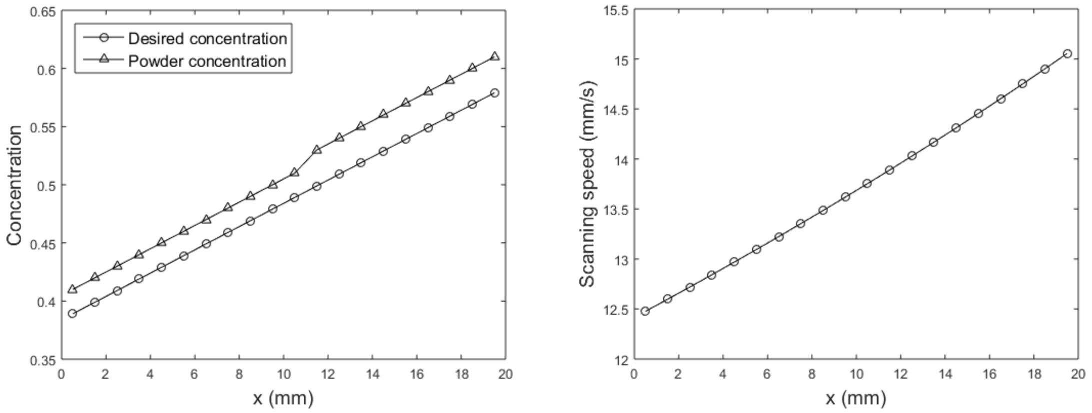

(a) (b)

Fig. 5.26 The operating parameters at the 20th layer, 15th track when setting the laser power as constant (calculation resolution 0.001): (a) the required powder concentration comparing with the desired concentration; and (b) the required laser scanning speed.

When setting the calculation resolution at 0.005, the calculation time decreases to about 2 hours. The trade-off is that the fabricated part may not have that accurate composition. For this case, the start layer is 13, and 1.8 mm of sacrificial layers should be removed. Since the calculation resolution is relatively low, the required powder concentration is almost the same as the desired composition, which can be seen in Fig. 5.27 (a). The mixing and overlapping have little effect here. However, if the part requires a higher accuracy, a higher calculation resolution should be applied.

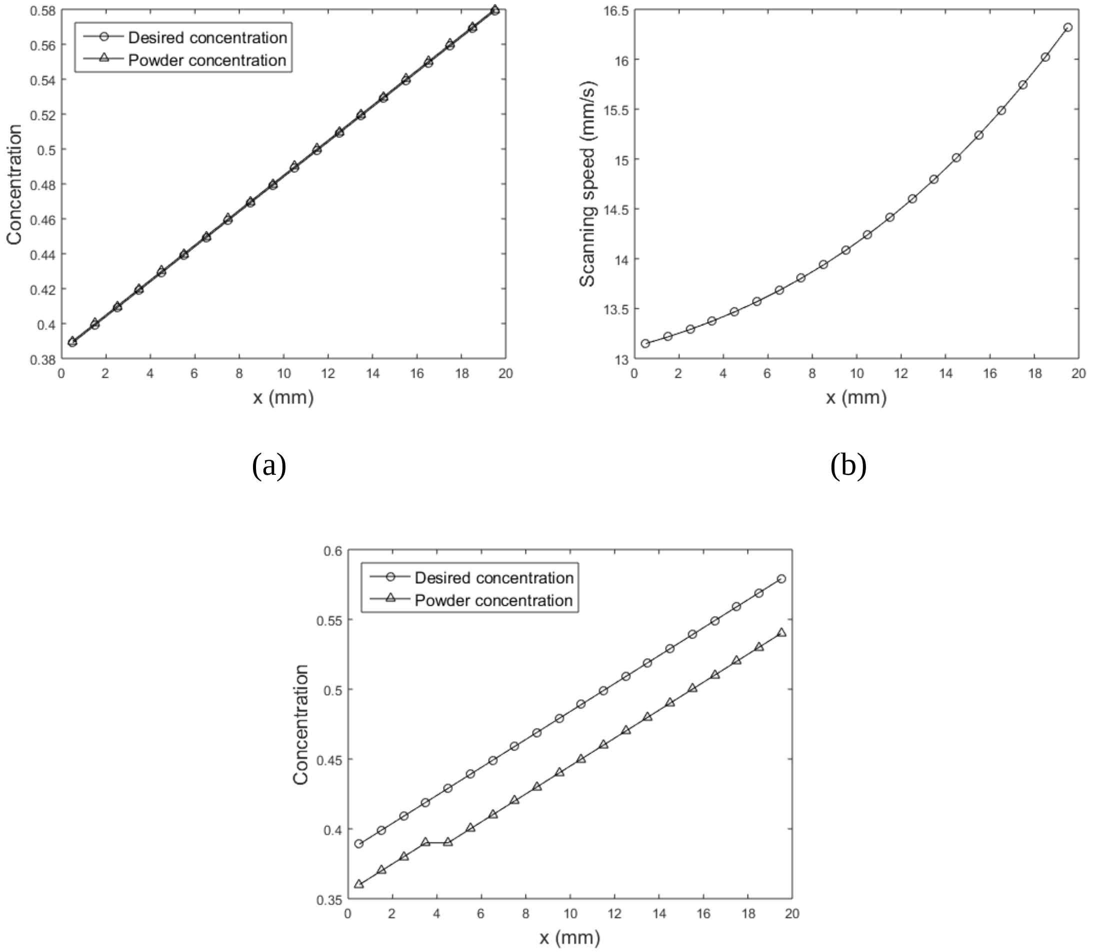

(a)

(b)

(c)

Fig. 5.27 The operating parameters at the 20th layer, 15th track when setting the laser power as constant: (a) the required powder concentration comparing with the desired concentration (resolution 0.005); (b) the required laser scanning speed (resolution 0.005); and (c) the required powder concentration comparing with the desired concentration (resolution 0.01).

It should be noted that the calculation resolution should not be set too low. For example, Fig. 27 (c) shows the calculated result for the required powder concentration comparing with the desired concentration when setting the calculation resolution at 0.01. It can be seen that the powder concentration is always lower than the desired concentration, which would result in an FGM part with very inaccurate composition.

Although the laser power is set as constant, the initial laser power should be calculated considering the powder shadowing effect. According to Eq. (5.22), the initial laser power is always 3049 W at calculation resolution 0.001 and 3054 W at calculation resolution 0.005. It can be seen that the powder composition has little effect on the attenuation, and the calculated initial laser power is always the same as long as the total powder feed rate remains constant.

Setting the scanning speed as constant

This situation works the similar way as the previous one. The laser scanning speed is set at constant 20 mm/s. The laser power is always a constant value when fabricating the first layer. The main difference is that for this case, one parameter (scanning speed) is truly fixed, while both the scanning speed and the laser power are varied in the former case. In this respect, the latter approach is favored since it adds the process stability by varying less parameters. However, it takes about 1 day to run the program, since the equivalent laser power needs to be calculated for each location following Eq. (5.43) whenever an output (laser power) from the ANN is generated.

The calculation resolution for material concentration is also set at 0.001. The start layer is 22, and a total of 21 layers (3.15 mm) should be removed after deposition. This is thus another benefit of this situation: a fewer numbers of sacrificial layers and a reduced material waste. The calculated operating parameters are shown in Fig. 5.28. Similar to the former case, the required powder concentration is always higher than the desired composition. The different between the two lines in Fig. 5.28 (a), however, is larger than that in Fig. 5.26 (a). This can be seen as due to the difference of the dilution rate values in the two cases. The dilution rate for the latter case is generally higher than the former case, thus it needs a higher concentration of Ni to mix with the substrate materials. It can also be seen from Fig. 5.28 (b) and (c) that the required laser power decreases along the track. Comparing with Fig. 5.26 (b), it is clear that the effect of decreasing the laser power is the same as increasing the laser scanning speed. The effect of calculation resolution is similar to the previous case, and therefore not discussed here.

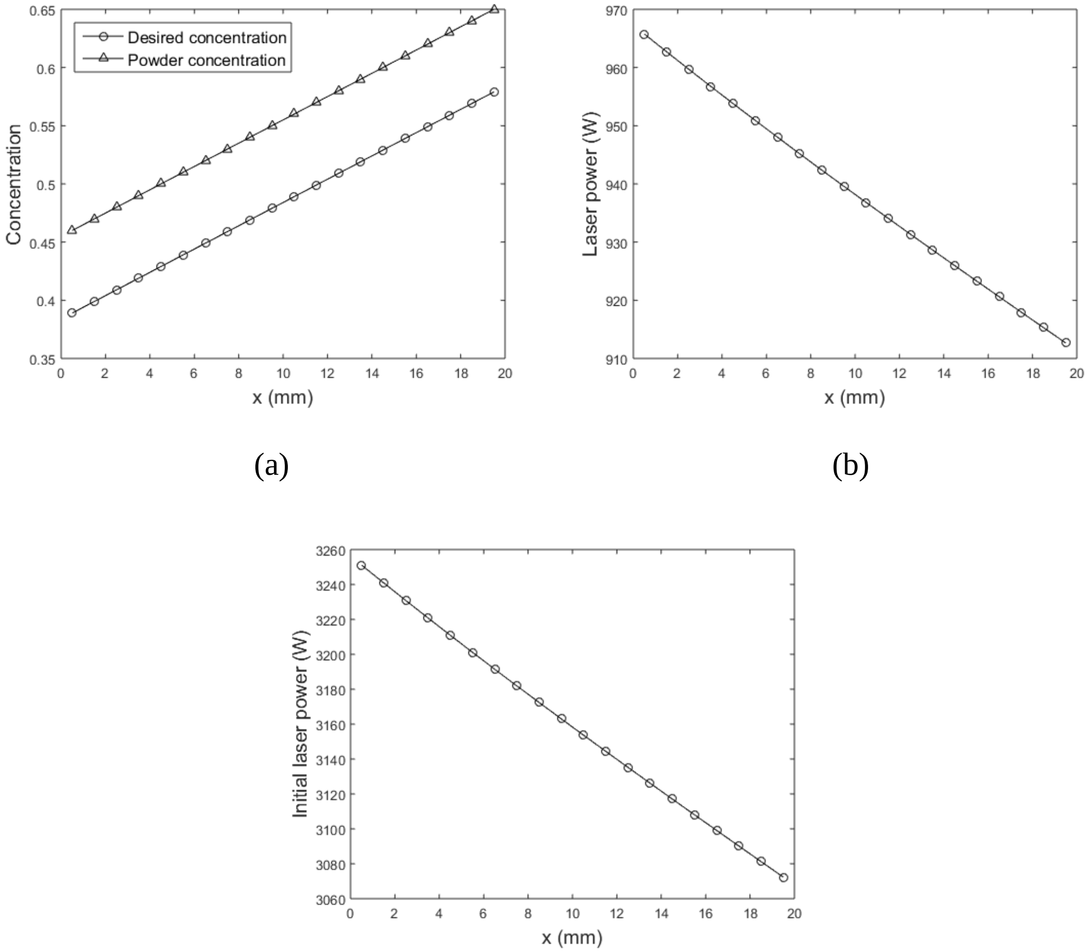

(a) (b)

(c)

Fig. 5.28 The operating parameters at the 20th layer, 15th track when setting the laser scanning speed as constant (calculation resolution 0.001): (a) the required powder concentration comparing with the desired concentration; (b) the required attenuated laser power; and (c) the required initial laser power.

It can be seen from Fig. 5.28 (c) that for this situation, the laser attenuation is about 70%, meaning that 30% of the initial laser power reaches the substrate. The required initial laser power is generally above 3000 W.

Building a locally graded part

This section briefly discusses the situation when building an FGM part which is locally graded. An example can be found from our previous work where a heterogeneous flywheel was represented and roughly fabricated by DMD [Morvan2001]. As shown in Fig. 1.1, the flywheel has homogeneous regions at the center and the edge, and a smoothly graded region is located in between. To build such a locally graded part, the process parameters should be planned as discussed before. The variation of the operating parameters are illustrated in this section when building the transition zone from the heterogeneous section to the homogeneous section.

A simple example is used here to just illustrate the concept. The new part is modified based on the part shown in Fig. 5.20. The new part has the same x and y dimensions as the previous part, but the height is 7.5 mm. The new part's composition is exactly the same as the previous part in the region below 6 mm height, and the region above 6 mm height is homogeneous, which has the same composition as the last layer of the previous part. Following the same design procedure, the required powder concentration for a random track and random element along z direction is shown in Fig.

5.29, for two situations respectively. The results are as expected: the required powder concentration is always higher than the desired composition, and after the 40th layer, the powder concentration directly drops to close to the desired concentration, becoming a horizontal line. The slight different between the required powder concentration and the desired concentration after the 40th layer is due to the calculation resolution. For the required laser power, the results are imaginable and are the same as the results in Sections 3.4.1 and 3.4.2 before the 40th layer, the required laser power directly turns into a horizontal line after the 40th layer.

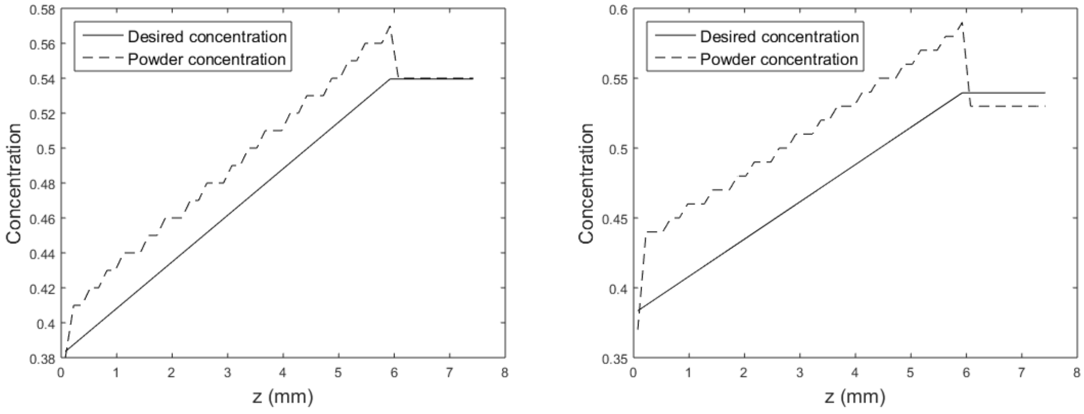

(a) (b)

Fig. 5.29 The required powder concentration comparing with the desired concentration for the 15th track, 10th element, bottom to top. (a) The laser power is set as constant, and (b) the scanning speed is set as constant.

5.4 Conclusions and Future Work

In this chapter, a design method is proposed to determine the process parameters during DMD fabrication of FGM parts. The proposed method incorporates the effects of dilution and overlapping among different layers and tracks for 3D parts. The varying material properties due to the FGM part composition are considered in the model. The design procedure is applicable to parts made of any materials and with any composition. Three case studies are given to illustrate the design method. Two case studies are shown for building a thin-walled structure where the composition (Inconel 718 and Ti-6Al-4V) varies in 1D and 2D respectively. A third case study is given as fabricating a 3D copper-nickel FGM part with composition varies in 3D. Using the proposed method, the operating parameters can be determined prior to the manufacturing process, which include the required powder concentration, laser power, and laser scanning speed. Decide whether to fix the laser power or the scanning speed depends on situations and preferences: fixing the laser power can reduce the computation time but finally requires the variation of both parameters (except for the always changing powder concentration during the fabrication process); fixing the scanning seed increases the computation time but only one parameter needs to be varied. The results also show that the calculation resolution plays a role in the final results. The fabricated part’s composition is more accuracy with a higher calculation resolution, but the number of sacrificial layers increases with the calculation resolution.

For better application of the proposed method, future work should include the following aspects: (1) considering more complicated FGM parts and investigate the relationship between the process parameters and the part composition; (2) Investigating the effects of the variation of different preset parameters on the final decision to help better understand the process; (3) taking into account the material properties variation due to the temperature change during fabrication; (4) the effect of laser spot size should be taken into account. A larger spot size would result in a larger melt pool, and therefore a higher layer thickness is allowed. In this case, although the manufacturing resolution is reduced, the dilution rate will be smaller and thus it is possible that less number of sacrificial layers are needed; (5) The dependence of building directions on the part composition accuracy, number of sacrificial layers, and part quality should be investigated; (6) Experimental validations of the proposed design method are necessary. The validation includes comparing the mechanical/thermal properties of the fabricated part with the theoretically predicted mechanical/thermal properties.

CHAPTER SIX

CONCLUSIONS AND FUTURE WORK

6.1 Conclusions

This dissertation studies the laser Direct Metal Deposition (DMD) of multi-material parts. The process mechanism is studied and the optimal process parameters are designed based on physical and mathematical models. Using the proposed design methodology, the process parameters can be designed/planned prior to the manufacturing process, achieving a better powder usage, laser energy usage, and a more accurate deposition compared to the desired composition. The major conclusions of this dissertation are discussed as follows.

6.1.1 Design of Injection Nozzle

In this research, a finite element model based injection nozzles geometric design is developed to optimize the laser energy efficiency and powder catchment efficiency in the DMD additive manufacturing process of Ti-6Al-4V. A neural network was developed to confront the problems of having a great amount of alternative designs and a considerable amount of calculation time. The suitable process parameters are applied based on simulations, and the synergetic effects of the nozzle geometric parameters on the two design objectives are investigated and analyzed. It is found that the bottom section of the nozzle has little effect on the laser energy efficiency, and a large slope angle is preferred. It is also found that the powder catchment efficiency decreases with the bottom section of the nozzle, and a small slope angle is preferred. In order to combine the two objectives, we define the process efficiency as the product of the two objective function outputs. Using this definition, the final designs are obtained, having a maximum laser energy efficiency and a powder catchment efficiency higher than 90%. The final design is driven by both design objectives: the objective function for laser energy efficiency has the dominant effect on L_2, while the objective function for powder catchment efficiency has the dominant effect on d, and D is driven by both objective functions. A couple of feasible designs exist. If other manufacturing constraints are not considered, one of the designs can be: L_1 = 0 mm, L_2 = 6 mm, d = 1.5 mm, and D = 4.5 mm. Some prescribed constants include: a 10 mm gap distance from nozzle tip to the substrate, a 20 mm length for the top section (L_3) of the injection nozzle, a 1 m/s inlet gas mean velocity, and a powder feed rate of 1.5 g/min.

6.1.2 Optimization of the Process Parameters in DMD of Multi-Materials

The fabrication of heterogeneous objects requires the mixing of a variable ratio of multiple powders. The powders feed rates are thus a changing variable during the fabrication process according to the material-embedded design model. The real-time optimization is difficult to achieve due to the time-consuming calculation (5 hours approximately). Therefore, this approach is more suitable as a pre-processing stage to analyze the design model and generate an operation file, which connects the model to a processing language that can be recognized by the DMD system. The proposed pre-process optimization approach has its merits in improving the print quality, and the DMD system should be able to memorize and/or even learn from the previous calculation results, which would greatly reduce the calculation time and be useful for potential real-time control.

This study provides an approach to optimize the process parameters in the pre-processing stage of multi-materials DMD. A calculation example is presented for prescribed powder feed rates. This approach can be easily generalized to any materials other than Inconel 718 and Ti-6Al-4V. Additional parameters other than the 8 design variables in this study may have to be considered in the future, e.g., laser spot size/shape would alter the approach and results.

6.1.3 Process Parameters Planning in DMD of FGM Parts

In this chapter, a design method is proposed to determine the process parameters during DMD fabrication of FGM parts. The proposed method incorporates the effects of dilution and overlapping among different layers and tracks for 3D parts. The varying material properties due to the FGM part composition are considered in the model. The design procedure is applicable to parts made of any materials and with any composition. Three case studies are given to illustrate the design method. Two case studies are shown for building a thin-walled structure where the composition (Inconel 718 and Ti-6Al-4V) varies in 1D and 2D respectively. A third case study is given as fabricating a 3D copper-nickel FGM part with composition varies in 3D. Using the proposed method, the operating parameters can be determined prior to the manufacturing process, which include the required powder concentration, laser power, and laser scanning speed. Decide whether to fix the laser power or the scanning speed depends on situations and preferences: fixing the laser power can reduce the computation time but finally requires the variation of both parameters (except for the always changing powder concentration during the fabrication process); fixing the scanning seed increases the computation time but only one parameter needs to be varied. The results also show that the calculation resolution plays a role in the final results. The fabricated part's composition is more accurate with a higher calculation resolution, but the number of sacrificial layers increases with the calculation resolution.

6.2 Future Work

Though the DMD process has been demonstrated to be able to fabricate heterogeneous objects with any composition, some technical issues still exist. The present work deals with the aspect of designing the process parameters in order to obtain a more efficient and more accurate manufacturing process. Much work should be done in order to excavate this technique's potential.

6.2.1 Design of Injection Nozzle

Future work should involve the printing of multiple layers, modeling the melt pool shape considering mass addition and driving forces for melt pool convection. Multiple injection nozzles should be implemented to calculate the coaxial nozzle or non-coaxial based powder catchment efficiency, the laser attenuation level and thus the laser energy efficiency. Last but most significant, experimental results should be shown in the future to validate and assess the results from modeling, and further improve the DMD process.

6.2.2 Optimization of the Process Parameters in DMD of Multi-Materials

In the future, the models in this study will be modified into a coaxial four-nozzle design, and the same material will be injected from two opposite nozzles. The four-nozzle configuration can also be applied to three or four materials mixing. Also, more physical-based realistic models should be applied, considering the gas-particle two phase flow and the free surface evolution when using dissimilar materials. In addition, fully numerical solutions will be used instead of analytical ones to account for more complex configurations in the fabrication process, e.g. fabrication of multiple layers, fabrication of a thin wall, and fabrication including mixing in the melt pool. In this case, more effects should be considered when choosing the suitable designs. For example, the side effect of a high particle injection velocity might be considered: the splatter of the liquid in the melt pool, and its influence on surface finish/resolution. This type of analysis also needs a practical test based on the optimized process parameters on the real DMD system to further substantiate the model predictions before advancing to real applications.

6.2.3 Process Parameters Planning during DMD of FGM Parts

For better application of the proposed method, future work should include the following aspects: (1) considering more complicated FGM parts and investigate the relationship between the process parameters and the part composition; (2) Investigating the effects of the variation of different preset parameters on the final decision to help better understand the process; (3) taking into account the material properties variation due to the temperature change during fabrication; (4) the effect of laser spot size should be taken into account. A larger spot size would result in a larger melt pool, and therefore a higher layer thickness is allowed. In this case, although the manufacturing resolution is reduced, the dilution rate will be smaller and thus it is possible that less number of sacrificial layers are needed; (5) The dependence of building directions on the part composition accuracy, number of sacrificial layers, and part quality should be investigated;

Also, experimental validations of the proposed design method are necessary. The validation includes comparing the mechanical/thermal properties of the fabricated part with the theoretically predicted mechanical/thermal properties. In the future, the printed part’s quality should be studied in respect of material science by looking at the dendrite growth and grain size using microscope and/or SEM. The grain size is reversely proportional to the cooling rate of the melt pool as shown in Chapter 2, and therefore the factors that affect the cooling rate should be considered. For example, the convective heat transfer coefficient, the material properties that may affect the conductive heat transfer, the heat that is brought into or brought away from the melt pool by the particles, the laser power, the laser scanning speed, and the laser spot size, etc.. This should be investigated by both experimental test and modeling. Another aspect is that the design typically expect to achieve some functionality by mixing several materials. However, the mixture rules do not necessarily apply to physical properties, and the issue of alloying needs to be fully understood to be able to reverse engineer the material composition needed to achieve some goal property.

REFERENCES

[Akbari2011] Akbari, M., Sinton, D., and Bahrami, M., 2011, "Geometrical Effects on the Temperature Distribution in a Half-Space Due to a Moving Heat Source," *Journal of Heat Transfer*, Vol. **133**(6), pp. 064502(1-10).

[Amine2014] Amine, T., Newkirk, J. W., and Liou, F., 2014, "An Investigation of the Effect of Direct Metal Deposition Parameters on the Characteristics of the Deposited Layers," *Case Studies in Thermal Engineering*, Vol. **3**, pp. 21-34.

[Anca2011] Anca, A., Cardona, Al., Risso, J., and Fachinotti, V.D., 2011, "Finite Element Modeling of Welding Processes," Applied Mathematical Modeling, Vol. 35(2), pp. 688-707.

[Antipas2015] Antipas, G. S. E., 2015, "Experimental and First Principles Assessment of Plasma Attenuation during Laser Treatment of an Al Alloy," *Transactions of the IMF*, Vol. **93**(1), pp. 53-56.

[Balu2012] Balu, P., Leggett, P., and Kovacevic, R., 2012, "Parametric Study on a Coaxial Multi-Material Powder Flow in Laser-based Powder Deposition Process," *Journal of Material Processing Technology*, Vol. **212**(7), pp. 1598-1610.

[Binnard1999] Binnard, M., 1999, "Design by Composition for Rapid Prototyping," *Ph. D. thesis*, Stanford University.

[Boivineau2006] Boivineau, M., Cagran, C., Doytier, D., Eyraud, V., Nadal, M.H., Wilthan, B., and Pottlacher, G., 2006, "Thermophysical Properties of Solid and Liquid Ti-6Al-4V (TA6V) Alloy," *International Journal of Thermophysics*, Vol. **27**(2), pp. 507-529.

[Bos1995] Bos, J., and Moes, H., 1995, "Frictional Heating of Tribological Contacts," *Journal of Tribology*, Vol. **117**(1), pp. 171-177.

[Buongiorno1994] Buongiorno, A., "United States Patent: 5477026 - Laser/Powdered Metal Cladding Nozzle," Jan 27, 1994.

[Cao2007] Cao, Y., and Choi, J., 2007, "Solidification Microstructure Evolution Model for Laser Cladding Process," *Transactions of the ASME*, Vol. **129**(7), pp. 852-863.

[Chakraborty2004] Chakraborty, N., Chakraborty, S., and Dutta, P., 2004, "Three-Dimensional Modeling of Turbulent Weld Pool Convection in GTAW Processes," *Numerical Heat Transfer, Part A: Applications: an International Journal of Computation and Methodology*, Vol. **45**(4), pp. 391-413.

[Chande1985] Chande, T., and Mazumder, J., 1985, "Two-Dimensional, Transient Model for Mass Transport in Laser Surface Alloying," *Journal of Applied Physics,* Vol. **57**(6), pp. 2226-2232.

[Cheikh2012] Cheikh, H. E., Courant, B., Branchu, S., Hascoët, J., and Guillén, R., 2012, "Analysis and Prediction of Single Laser Tracks Geometrical Characteristics in Coaxial Laser Cladding Process," *Optics and Lasers in Engineering,* Vol. **50**(3), pp. 413-422.

[Chen2011] Chen, H., Pinkerton, A.J., and Li, L., 2011, "Fibre Laser Welding of Dissimilar Alloys of Ti-6Al-4V and Inconel 718 for Aerospace Applications," *International Journal of Advanced Manufacturing Technology,* Vol. **52**(9), pp. 977-987.

[Choo1994] Choo, R.T.C., and Szekely, J., 1994, "The Possible Role of Turbulence in GTA Weld Pool Behavior," *Welding Research,* Feb 1994, pp. 26s-30s.

[Christensen1965] Christensen, N., Davies, V. L., and Gjermundsen, K., 1965, "Distribution of Temperature in Arc Welding," *British Welding Journal*, pp. 54-75.

[Collins2003] Collins, P.C., Banerjee, R., and Fraser, H.L., 2003, "The Influence of the Enthalpy of Mixing During the Laser Deposition of Complex Titanium Alloys Using Elemental Blends," *Scripta Materialia,* Vol. **48**(10), pp. 1445-1450.

[Damborenea1994] Damborenea, J., Vázquez, A.J., and Fernández, B., 1994, "Laser-Clad 316 Stainless Steel with Ni-Cr Powder Mixtures," Materials & Design, Vol. **15**(1), pp. 41-44.

[David2008] David, S. A., DebRoy, T., DuPont, J.N., Koseki, T., and Smartt, H.B., 2008, "Trends in Welding Research," Pine Mountain, Georgia, USA.

[DebRoy1995] DebRoy, T., 1995, "Physical Processes in Fusion Welding," *Review of Modern Physics,* Vol. **67**(1), pp. 85-112.

[Domack2005] Domack, M.S., and Baughman, J.M., 2005, "Development of Nickel-Titanium Graded Composition Components," *Rapid Prototyping Journal,* Vol. **11**(1), pp. 41-51.

[DuPont1995] DuPont, J.N., and Marder, A.R., 1995, "Thermal Efficiency of Arc Welding Processes," *Welding Journal,* Vol. **74**, pp. 406s-416s.

[Easton2011] Easton, M., Davidson, C., and StJohn, D., 2011, "Grain Morphology of As-Cast Wrought Aluminum Alloys," *Materials Transactions,* Vol. **52**(5), pp. 842-847.

[Emamian2010] Emamian, A., Corbin, S. F., and Khajepour A., 2010, "Effect of Laser Cladding Process Parameters on Clad Quality and in-situ Formed Microstructure of Fe-TiC Composite Coatings," *Surface Coating Technology*, Vol. **205**(7), pp. 2007-2015.

[Ensz2002] Ensz, M., Griffith, M., and Reckaway, D., 2002, "Critical Issues for Functionally Graded Material Deposition by Laser Engineered Net Shaping (LENS)," *Proceedings of the 2002 MPIF Laser Metal Deposition Conference*, San Antonio, TX.

[Ermurat2013] Ermurat, M., Arslan, M. A., Erzincanli, F., and Uzman, I., 2013, "Process Parameters Investigation of a Laser-Generated Single Clad for Minimum Size Using Design of Experiments," *Rapid Prototyping Journal*, Vol. **19**(6), pp. 452-462.

[Everett1993] Everett, M. A., and Blankshain, A. R., "United States Patent: 5453329 A - Method for Laser Cladding Thermally Insulated Abrasive Particles to a Substrate, and Clad Substrate Formed Thereby," Apr 30, 1993.

[Fadel2002] Fadel, G., and Morvan, S., 2002, "Multi-material Representation and Design issues," Chapter 6, in Software Solution for Rapid Prototyping, Wiley, London, UK.

[Fathi2006] Fathi, A., Toyserkani, E., Khajepour, A., and Durali, M., 2006, "Prediction of Melt Pool Depth and Dilution in Laser Powder Deposition," *Journal of Physics D: Applied Physics*, Vol. **39**(12), pp. 2613-2623.

[Fathi2007] Fathi, A., Khajepour, A., Toyserkani, E., and Durali, M., 2007, "Clad Height Control in Laser Solid Freeform Fabrication Using a Feedforward PID Controller," *the International Journal of Advanced Manufacturing Technology*, Vol. **35**(3), pp. 280-292.

[Fazelpour2014] Fazelpour, M., and Summers, J.D., 2014, "Evolution of Meso-Structures for Non-Pneumatic Tire Development: A Case Study," *Proceedings of the ASME 2016 International Design Engineering technical Conferences & Computers and Information in Engineering Conference (IDETC/CIE)*, Baffalo, New York, August 2014.

[Fazelpour2016] Fazelpour, M., Shankar, P., and Summers, J.D., 2016, "Developing Design Guidelines for Meso-scaled Periodic Cellular Material Structures under Shear Loading," *Proceedings of the ASME 2016 International Design Engineering technical Conferences & Computers and Information in Engineering Conference (IDETC/CIE)*, Charlotte, North Carolina, August 2016.

[Fessler1997] Fessler, J., Nickel, A., Link, G., and Prinz, F., 1997, "Functional Gradient Metallic Prototypes through Shape Deposition Manufacturing," *Proceedings of*

Symposium on Solid Freeform Fabrication, University of Texas at Austin, Austin, Texas, August 1997, pp. 521-528.

[Franke2010] Franke, M. M., Hilbinger, R. M., Konrad, C. H., Glatzel, U., and Singer, R. F., 2010, "Numerical Determination of Secondary Dendrite Arm Spacing," *Metallurgical and Materials Transactions A*, Vol. **42A**, pp. 1847-1853.

[Frenk1993] Frenk, A., and Kurz, W., 1993, "High Speed Laser Cladding: Solidification Conditions and Microstructure of a Cobalt-Based Alloy," *Materials Science and Engineering*, Vol. **173**(1-2), pp. 339-342.

[Fu2002] Fu, Y., Loredo, A., Martin, B., and Vannes, A. B., 2002, "A Theoretical Model for Laser and Powder Particles Interaction during Laser Cladding," *Journal of Materials Processing Technology*, Vol. **128**(1-3), pp. 106-112.

[Garland2015] Garland, A., and Fadel, G.M., 2015, "Design and Manufacturing Functionally Grade Material Objects with an off the Shelf Three-Dimensional Printer", *Journal of Mechanical Design*, Vol. **137**(11), pp. 111407(1-11).

[Giuliani2009] Giuliani, V., Hugo, R. F., and Gu, P., 2009, "Powder Particle Temperature Distribution in Laser Deposition Technologies," *Rapid Prototyping Journal*, Vol. **15**(4), pp. 244-254.

[Goldak1984] Goldak, J., Chakravarti, A., and Bibby, M., 1984, "A New Finite Element Model for Welding Heat Sources," *Metallurgical Transactions B*, Vol. **15B**(2), pp. 299-305.

[Goodarzi2005] Goodarzi, D.M., 2005, "Effect of Process Parameters in Laesr Cladding on Substrate Melted Areas and the Substrate Melted Shape," Journal of Laser Applications, Vol. **27**(S2), pp. S29201(1-9).

[Griffith1997] Griffith M.L, Harwell L.D, Romero J.A, Schlienger E, Atwood C.L, and Smugeresky J.E., 1997, "Multi-Material Processing by LENS^{TM}," *Proceedings of the Solid Freeform Fabrication Symposium*, Austin, TX.

[Grigoryants2015] Grigoryants, A. G., Tretyakov, R. S., Shiganov, I. N., and Stavertiy, A. Ya. 2015, "Optimization of the Shape of Nozzles for Coaxial Laser Cladding," *Welding International*, Vol. **29**(8), pp. 639-642.

[Grujicic2001] Grujicic, M., Hu, Y., Fadel, G.M., and Keicher, D.M., 2001, "Optimization of the LENS Rapid Fabrication Process for In-Flight Melting of Feed Powder," *Journal of Materials Synthesis and Processing*, Vol. **9**(5), pp. 223-233.

[Gu2004] Gu, S., McCartney, D.G., Eastwick, C.N., and Simmons, K., 2004, "Numerical

Modeling of In-Flight Characteristic of Inconel 625 Particle during High-Velocity Oxy-Fuel Thermal Spraying," *Journal of Thermal Spray Technology,* Vol. **13**(2), pp. 200-213.

[Gu2012] Gu, D.D., Meiners, W., Wissenbach, K., and Poprawe, R., 2012, "Laser Additive Manufacturing of Metallic Components: Materials, Processes and Mechanisms," *International Materials Review,* Vol. **57**(3), pp. 133-164.

[Guo2004] Guo, W., "United States Patent: 7259353 - Compact Coaxial Nozzle for Laser Cladding," Sep 30, 2004.

[Guo2013] Guo, Si., Chen, Z., Cai, D., Zhang, Q., Kovalenko, V., and Yao, J., 2013, "Prediction of Simulating and Experiments for Co-Based Alloy Laser Cladding by HPDL," *Physics Procedia,* Vol. **50**, pp. 375-382.

[Han2004] Han, L., Liou, F.W., and Phatak, K.M., 2004, "Modeling of Laser Cladding with Powder Injection," *Metallurgical and Materials Transactions B,* Vol. **35**(6), pp. 1139-1150.

[He2003] He, X., Fuerschbach, P.W., and DebRoy, T., 2003, "Heat Transfer and Fluid Flow During Laser Spot Welding of 304 Stainless Steel," *Journal of Physics D: Applied Physics,* Vol. **36**(12), pp. 1388-1398.

[He2007] He, X., and Mazumder, J., 2007, "Transport Phenomena during Direct Metal Deposition," Journal of Applied Physics, Vol. **101**(5), pp. 053113(1-9).

[Heigel2015] Heigel, J. C., Michaleris, P., and Palmer, T. A., 2015, "In situ Monitoring and Characterization of Distortion during Laser Cladding of Inconel 625," *Journal of Materials Processing technology,* Vol. **220**, pp. 135-145.

[Hofmann2014] Hofmann, D.C., Roberts, S., Otis, R., Kolodziejska, J., Dillon, R.P., Suh, J., Shapiro, A.A., Liu, Z., and Borgonia, J., 2014, "Developing Gradient Metal Alloys through Radial Deposition Additive Manufacturing," *Nature Scientific Reports,* July 19.

[Hou2000] Hou, Z. B., and Komanduri, R., 2000, "General Solutions for Stationary/Moving Plane Heat Source Problems in Manufacturing and Tribology," *International Journal of Heat and Mass Transfer,* Vol. **43**(10), pp. 1679-1698.

[Hu2006] Hu, Y., Fadel, G.M., Blouin, V., and White, D. 2006, "Optimal Design for Additive Manufacturing of Heterogeneous Objects Using Ultrasonic Consolidation," Invited paper, *Journal of virtual and physical prototyping,* Vol. **1**(1), pp. 53-62.

[Hu2008] Hu, Y., Blouin, V. and Fadel, G.M., 2008, "Design for Manufacturing of 3D

Heterogeneous Objects with Processing Time Considerations", *Journal of Mechanical Design,* Vol. **130**(3), pp. 031701(1-9).

[Huang2000a] Huang, J., 2000, "Heterogeneous Component Modeling and Optimal Design for Manufacturing," *Ph. D. thesis*, Clemson University.

[Huang2000b] Huang, J., and Fadel, G., 2000, "Heterogeneous Flywheel Modeling and Optimization," *Materials and Design,* Vol. **21**(2), pp. 111-125.

[Huang2001] Huang, J., and Fadel, G., 2001, "Bi-Objective Optimization Design of Heterogeneous Injection Mold Cooling Systems," *Journal of Mechanical Design,* Vol. **123**(2), pp. 226-239.

[Huang2002] Huang, J., 2002, "Heterogeneous Component Modeling and Optimal Design for Manufacturing," *Ph. D. thesis,* Clemson University.

[Huang2005] Huang, Y., Liang, G., Su, J., and Li, J., 2005, "Interaction between Laser Beam and Powder Stream in the Process of Laser Cladding with Powder Feeding," *Modeling and Simulation in Materials Science and Engineering,* Vol. **13**(1), pp. 47-56.

[Ibarra-Medina2011] Ibarra-Medina, J., and Pinkerton, A. J., 2011, "Numerical Investigation of Powder Heating in Coaxial Laser Metal Deposition," *Surface Engineering,* Vol. **27**(10), pp. 754-761.

[Jaeger1942] Jaeger, J., 1942, "Moving Sources of Heat and the Temperature at Sliding Contacts," *J. Proc. Soc. N.S.W.,* **Vol.** 74, pp. 203-224.

[Jiang2002] Jiang, W., and Molian, P., 2002, "Laser Based Flexible Fabrication of Functionally Graded Mould Inserts," *The International Journal of Advanced Manufacturing Technology,* Vol. **19**(9), pp. 646-654.

[Jouvard1997] Jouvard, J.M., Grevey, D.F., Lemoine, F., and Vannes, A.B., 1997, "Continuous Wave Nd: YAG Laser Cladding Modeling: a Physical Study of Track Creation during Lower Power Processing," *Journal of Laser Applications,* Vol. **9**(1), pp. 43-50.

[Kamara2011] Kamara, A.M., Wang, W., Marimuthu, S., and Li, L., 2011, "Modeling of the melt pool geometry in the laser deposition of nickel alloys using the anisotropic enhanced thermal conductivity approach," *Proceedings of the Institution of Mechanical Engineers, Part B: Journal Engineering Manufacture,* Vol. **225**(1), pp. 87-99.

[Ki2002] Ki, H., Mohanty, P.S., and Mazumder, J., 2002, "Modeling of Laser Keyhole

Welding: Part II. Simulation of Keyhole Evolution, Velocity, Temperature Profile, and Experimental Verification," *Metallurgical and Materials Transactions, A*, Vol. **33A**(6), pp. 1831-1842.

[Kieback2003] Kieback, B., Neubrand, A., and Riedel, H., 2003, "Processing Techniques for Functionally Graded Materials," *Materials Science and Engineering A*, Vol. **362**(1-2), pp. 81-105.

[Kim2000a] Kim, J., and Peng, Y., 2000, "Melt Pool Shape and Dilution of Laser Cladding with Wire Feeding," *Journal of Materials Processing Technology*, Vol. **104**(3), pp. 284-293.

[Kim2000b] Kim, J., and Peng, Y., 2000, "Plunging Method for Nd: YAG Laser Cladding with Wire Feeding," *Optics and Lasers in Engineering*, Vol. **33**(4), pp. 299-309.

[Kong2010] Kong, F., and Kovacevic, 2010, "Modeling of Heat Transfer and Fluid Flow in the Laser Multilayered Cladding Process," *Metallurgical and Materials Transactions B*, Vol. **41B**(6), pp. 1310-1320.

[Koseki2003] Koseki, T., Inoue, H., Fukuda, Y., and Nogami, A., 2003, "Numerical Simulation of Equiaxed Grain Formation in Weld Solidification," *Science and Technology of Advanced Materials*, Vol. **4**(2), pp. 183-195.

[Kou2007] Kou, X.Y., and Tan, S.T., 2007, "Heterogeneous Object Modeling: a Review," *Computer- Aided Design*, Vol. **39**(4), pp. 284-301.

[Krishna2008] Krishna, B. V., Bose, Su., and Bandyopadhyay, A., 2008, "Fabrication of Porous NiTi Shape Memory Alloy Structures Using Laser Engineered Net Shaping," *Journal of Biomedical Materials Research Part B: Applied Biomaterials*, Vol. **89**(2), pp. 481-490.

[Kumar1997] Kumar, V., and Dutta, D., 1997, "An Approach to Modeling Multi-Material Objects," presented a Third Symposium on Solid Modeling and Applications, Atlanta, GA, 1997.

[Kumar1999] Kumar, V., 1999, "Solid Modeling and Algorithms for Heterogeneous Objects," *Ph. D. thesis,* The University of Michigan, 1999.

[Lahoz2004] Lahoz, R., and Puértolas, J.A., 2004, "Training and Two-Way Shape Memory in NiTi Alloys: Influence on Thermal Parameters," *Journal of Alloys and Compounds*, Vol. **381**(1-2), pp. 130-136.

[Lamikiz2011] Lamikiz, A., Tabernero, I., Ukar, E., Martinez, S., and Lacalle, L.N.L., 2011, "Current Designs of Coaxial Nozzles for Laser Cladding," *Recent Patents on*

Mechanical Engineering, Vol. **4**(1), 29-36.

[Lewis1995] Lewis, G. K., and Less, R. M., “United States Patent: 5961862 - Deposition Head for Laser,” Nov 30, 1995.

[Lewis2000] Lewis, G.K., and Schlienger, E., 2000, “Practical Considerations and Capabilities for Laser Assisted Direct Metal Deposition,” *Materials and Design*, Vol. **21**(4), pp. 417-423.

[Li2000] Li, X., Stampfl, J., and Prinz, F.B., 2000, “Mechanical and Thermal Expansion Behavior of Laser Deposited Metal Matrix Composites of Invar and TiC,” *Materials Science and Engineering*, Vol. **282A**(1-2), pp. 86-90.

[Li2016] Li, Q., Lin, X., Wang, X., Yang, H., Song, M., and Huang, W., 2016, “Research on the Grain Boundary Liquation Mechanism in Heat Affected Zones of Laser Forming Repaired K465 Nickel-Based Superalloy,” *Metals*, Vol. **6**(3), pp. 1-10.

[Lin1997] Lin, J., and Steen, W. M., 1997, “Powder Flow and Catchment during Coaxial Laser Cladding,” *Proceedings of SPIE Lasers in Material Processing*, Vol. **3097**, pp. 517-528.

[Lin1999a] Lin, J., 1999, “Concentration Model of the Powder Stream in Coaxial Laser Cladding,” *Optics & Laser Technology*, Vol. **31**(3), pp. 251-257.

[Lin1999b] Lin, J., 1999, “Temperature Analysis of the Powder Streams in Coaxial Laser Cladding,” *Optics & Laser Technology*, Vol. **31**(8), pp. 565-570.

[Lin2000a] Lin, J., 2000, “Numerical Simulation of the Focused Powder Streams in Coaxial Laser Cladding,” *Journal of Materials Processing Technology*, Vol. **105**(1-2), pp. 17-23.

[Lin2000b] Lin, J., 2000, “Laser Attenuation of the Focused Powder Streams in Coaxial Laser Cladding,” *Journal of Laser Applications*, Vol. **12**(1), pp. 28-33.

[Lin2005] Lin, X., Yue, T.M., Yang, H.O., and Huang, W.D., 2005, “Laser Rapid Forming of SS316L/Rene88DT Graded Material,” *Materials Science and Engineering A*, Vol. **391**(1-2), pp. 325-336.

[Lin2007] Lin, X., Yue, T.M., Yang, H.O., and Huang, W.D., 2007, “Solidification Behavior and the Evolution of Phase in Laser Rapid Forming of Graded Ti6Al4V-Rene88DE Alloy,” Metallurgical and Materials Transactions A., Vol. **38A**(1), pp. 128-137.

[Liu2003] Liu, C., and Liu, J., 2003, “Thermal Process of a Powder Particle in Coaxial Laser Cladding,” *Optics and Laser Technology*, Vol. **35**(2), pp. 81-86.

[Liu2005a] Liu, J., Li, L., Zhang, Y., and Xie, X., 2005, "Attenuation of Laser Power of a Focused Gaussian Beam during Interaction between a Laser and Powder in Coaxial Laser Cladding," *Journal of Physics D: Applied Physics,* Vol. **38**(10), pp. 1546-1550.

[Liu2005b] Liu, J., and Li, L., 2005, "Study on Cross-Section Clad Profile in Coaxial Single-Pass Cladding with a Low-Power Laser," *Optics & Technology,* Vol. **37**(6), pp. 478-482.

[Liu2005c] Liu, J., and Li, L., 2005, "Effects of Powder Concentration Distribution on Fabrication of Thin-Wall Parts in Coaxial Laser Cladding," *Optics & Laesr Technology,* Vol. 37(4), pp. 287-292.

[Liu2006] Liu, X., and Wang, H., 2006, "Modification of Tribology and High-Temperature Behaviro of Ti-48Al-2Cr-2Nb Intermetallic Alloy by Laser Cladding," *Applied Surface Science,* Vol. **252**(16), pp. 5735-5744.

[Liu2014] Liu, S., and Kovacevic, R., 2014, "Statistical Analysis and Optimization of Processing Parameters in High-Power Direct Diode Laser Cladding," *the International Journal of Advanced Manufacturing Technology,* Vol. **74**(5), pp.867-878.

[Lowney2000] Lowney, M.T.J., "United State Patent: 6534745 B1 – Nozzle Particularly Suited to Direct Metal Deposition," Sep 27, 2000.

[Luo2015] Luo, Y., Tang, X., Lu, F., Chen, Q., and Cui, H., 2015, "Spatial Distribution Characteristics of Plasma Plume on Attenuation of Laser Radiation under Subatmospheric Pressure," *Applied Optics,* Vol. **54**(5), pp. 1090-1096.

[Mackwood2005] Mackwood, A. P., and Crafer, R. C., 2005, "Thermal Modeling of Laser Welding and Related Processes: a Literature Review," *Optics & Laser Technology,* Vol. **37**(2), pp. 99-115.

[Mahamood2015] Mahamood, R.M., and Akinlabi, E.T., 2015, "Laser Metal Deposition of Functionally Graded Ti6Al4V/TiC," *Materials and Design,* Vol. **84**(5), pp. 402-410.

[Majumdar2005] Majumdar, J. D., Pinkerton, A., Liu, Z., Manna, I., and Li, L., 2005, "Microstructure Characterization and Process Optimization of Laser Assisted Rapid Fabrication of 316L Stainless Steel," *Applied Surface Science,* Vol. **247**(1-4), pp. 320-327.

[Marimuthu2013] Marimuthu, S., Eghlio, R.M., and Pinkerton, A.J., 2013, "Coupled Computational Fluid Dynamic and Finite Element Multiphase Modeling of Laser Weld Bead Geometry Formation and Joint Strengths," Journal of Manufacturing

Science and Engineering, Vol. **135**(1), pp. 011004(1-10).

[Mazumder1999] Mazumder, J., Schifferer, A., and Choid, J., 1999, “Direct Materials Deposition: Designed Macro and Microstructure,” *Materials Research Innovations*, Vol. **3**(3), pp. 118-131.

[Mazumder2000] Mazumder, J., Dutta, D., Kikuchi, N., and Ghosh, A., 2000, “Closed Loop Direct Metal Deposition: Art to Part,” Optics and Lasers in Engineering, Vol. **34**(4-6), pp. 397-414.

[Miyagi2010] Miyagi, M., Tsukamoto, T., and Kawanaka, H., “United Stated Patent: 8735769 B2 – Laser Processing Head and Laser Cladding Method,” Oct 19, 2010.

[Morville2012a] Morville, S., Carin, M., Carron, D., Masson, P. L., Gharbi, M., Peyre, P., and Fabbro, R., 2012, “Numerical Modeling of Powder Flow during Coaxial Laser Direct Metal Deposition – Comparison between Ti-6Al-4V Alloy and Stainless Steel 316L,” Proceedings of the 2012 COMSOL Conference, Milan.

[Morville2012b] Morville, S., Carin, M., Peyre, P., Gharbi, M., Carron, D., Masson, P. L., and Fabbro, R., 2012, “2D Longitudinal Modeling of Heat Transfer and Fluid Flow during Multilayered DLMD Process,” *Journal of Laser Applications*, Vol. **24**(3), pp. 032008(1-9).

[Morvan2001] Morvan, S., 2001, “MMa-Rep, a Representation for Multimaterial Solids,” *Ph. D. thesis*, Clemson University.

[Müller2003] Müller, E., Drašar, Č., Schilz, J., and Kaysser, W. A., 2003, “Functionally Graded Materials for Sensor and Energy Applications,” *Material Science and Engineering*, Vol. **A362**(1-2), pp. 17-39.

[Müller2013] Müller, P., Mognol, P., and Hascoet, J., 2013, “Modeling and Control of a Direct Laser Powder Deposition for Functionally Graded Materials (FGM) Parts Manufacturing,” *Journal of Materials Processing Technology*, Vol. **213**(5), pp. 685-692.

[Nemat-Alla2011] Nemat-Alla, M.M., Ata, M.H., Bayoumi, M.R., and Khair-Eldeen, W., 2011, “Powder Metallurgical Fabrication and Microstructural Investigations of Aluminum/Steel Functionally Graded Material,” *Materials Sciences and Applications*, Vol. **2**(12), pp. 1708-1718.

[Nenadl2014] Nenadl, O., Ocelík, V., Palavra A., and Hosson, J., 2014, “The Prediction of Coating Geometry from Main Processing Parameters in Laser Cladding,” *Physics Procedia*, Vol. **56**, pp. 220-227.

[Nowotny2000] Nowotny, S., and Scharek, S., "United State Patent: 6316744 B1 – Machining Head and Process for the Surface Machining of Workpieces by Means of a Laser Beam," Mar 3, 2000.

[Ocylok2010] Ocyloc, S., Weisheit, A., and Kelbassa, I., 2010, "Functionally Graded Multi-Layers by Laser Cladding for Increased Wear and Corrosion Protection," *Physics Procedia*, Vol. **5A**, pp. 359-367.

[Oliveira2005] Oliveira, U., Ocelík, V., and Hosson, J. Th. M., 2005, "Analysis of Coaxial Laser Cladding Processing Conditions," *Surface and Coatings Technology*, Vol. **197**(2-3), pp. 127-136.

[Okada1977] Okadam A., 1977, "Application of Melting Efficiency and Its Problems," *Journal of Japan Welding Society*, Vol. **46**(2), pp. 53-61.

[Osman2009] Osman, T., and Boucheffa, A., 2009, "Analytical Solution for the 3D Steady State Condition in a Solid Subjected to a Moving Rectangular Heat Source and Surface Cooling," *Comptes Rendus Mécanique*, Vol.**337**(2), pp. 107-111.

[Otterloo1997] Otterloo, J.L., and Hosson, J.T., 1997, "Microstructural Features and Mechanical Properties of a Cobalt-Based Laser Coating," *Acta Materialia*, Vol. **45**(3), pp. 1225-1236.

[Pan2006] Pan, H., Sparks, T., Thakar, Y. D., and Liou F., 2006, "Grvity-Driven Metal Powder Flow in Coaxial Nozzle for Laser-Aided Direct Metal Deposition Process," *Journal of Manufacturing Science and Engineering*, Vol. **128**(2), pp. 541-553.

[Patel2001] Patel, A. D., and Murty, Y. V., 2001, "Effect of Cooling Rate on Microstructural Development in Alloy 718," *The Minerals, Metals & Materials Society*, pp. 123-132.

[Pavlyk2004] Pavlyk, V., and Dilthey, U., 2004, "Simulation of Weld Solidification Microstructure and Its Coupling to the Macroscopic Heat and Fluid Flow Modeling," *Modeling and Simulation in Materials Science and Engineering*, Vol. **12**(1), pp. S33-S45.

[Peng2006] Peng, Z., Azer, M., Li, Y., Chen, X., and Huang, X., "United States Patent: 20070193981 - Nozzle for Laser Net Shape Manufacturing," Fab 22, 2006.

[Peyre2008] Peyre, P., Aubry, P., Fabbro, R., Neveu, R., and Longuet, A., 2008, "Analytical and Numerical Modeling of the Direct Metal Deposition Laser Process," *Journal of Physical D: Applied Physics*, Vol. **41**(2), pp. 025403(1-10).

[Picasso1994a] Picasso, M., Marsden, C. F., Wagnière, J. D., Frenk, A., and Rappaz, M., 1994, “A Simple but Realistic Model for Laser Cladding,” *Metallurgical and Materials Transactions B*, Vol. **25B**(2), pp. 281-291.

[Pinkerton2004] Pinkerton, A. J., Li, L., 2004, “Modeling Powder Concentration Distribution from a Coaxial Deposition Nozzle for Laser-Baser Rapid Tooling,” *Journal of Manufacturing Science and Engineering*, Vol. **126**(1), pp. 33-41.

[Pinkerton2007] Pinkerton, A. J., 2007, “An Analytical Model of Beam Attenuation and Powder Heating during Coaxial Laser Direct Metal Deposition,” *Journal of Physics D: Applied Physics*, Vol. **40**(23), pp. 7323-7334.

[Pintsuk2003] Pintsuk, G., Brünings, S.E., Döring, J.-E., Linke, J., Smid, I., and Xue, L., 2003, “Development of W/Cu – Functionally Graded Materials,” *Fusion Engineering and Design*, Vol. **66-68**, pp. 237-240.

[Pottlacher2002] Pottlacher, G., Hosaeus, H., Kaschnitz, E., and Seifter, A., 2002, “Thermophysical Properties of Solid and Liquid Inconel 718 Alloy,” *Scandinavian Journal of Metallurgy*, Vol. **31**(3), pp. 161-168.

[Pulugurtha2014] Pulugurtha, S.R., 2014, “Functionally Grade Ti6S4V and Inconel 625 by Laser Metal Deposition,” *Ph.D. thesis*, Missouri University of Science and Technology.

[Punch1995] Punch, W. F., Averill, R. C., Goodman, E. D., Lin, S., and Ding, Y., “Design Using Genetic Algorithms – Some Results for Laminated Composite Structures,” *IEEE Expert*, Vol. **10**(1), pp. 42-49.

[Pyritz2002] Pyritz, C. L., Arcella, F. G., and House, M. A., “United States Patent: 6696664 B2 - Powder Feed Nozzle for Laser Welding,” Apr 1, 2002.

[Qi2006a] Qi, H., and Mazumder, J., 2006, “Laser Cladding Based Solid Freeform Fabrication and Direct Metal Deposition,” *Proceedings of MSEC 2006 International Conference on Manufacturing Science and Engineering*, Ypsilanti, Michigan, October 2006.

[Qi2006b] Qi, H., and Mazumber, J., 2006, “Numerical Simulation of Heat Transfer and Fluid Flow in Coaxial Laser Cladding Process for Direct Metal Deposition,” *Journal of Applied Physics*, Vol. **100**(2), pp. 024903.

[Ranalli1996] Ranalli, R.J., “United State Patent: 5607730 A – Method and Apparatus for Laser Coating,” Jun 13, 1996.

[Ranz1952] Ranz, W. E., and Marshall, W. R., 1952, “Evaporation from Drops,” *Chemical Engineering Progress*, Vol. **48**(3), pp. 141-146 (Part I); **48**(4), pp. 173-180 (Part II).

[Rosenthal1946] Rosenthal, D., and Mass, C., November 1946, "The Theory of Moving Sources of Heat and Its Application to Metal Treatments," *Transactions of the ASME*, pp. 849-866.

[Ross1992] Ross, R. B., 1992, "Metallic Materials Specification Handbook," Springer Science + Business Media, B.V., Netherland.

[Saedodin2010] Saedodin, S., Akbari, M., Raisi, A., and Torabi, M., 2010, "Calculation and Investigation of Temperature Distribution and Melt Pool Size Due to a Moving Laser Heat Source Using the Solution of Hyperbolic Heat Transfer Equation," *World Applied Science Journal*, Vol. **11**(10), pp. 1273-1281.

[Salehi2006] Salehi, D., and Brandt, M., 2006, "Melt Pool Temperature Control Using LabVIEW in Nd:YAG Laser Blown Powder," *International Journal of Advanced Manufacturing Technology*, Vol. **29**(3-4), pp. 273-278.

[Saqib2014] Saqib, S., Urbanic, R.J., and Aggarwal, K., 2014, "Analysis of Laser Cladding Bead Morphology for Developing Additive Manufacturing Travel Paths," *Procedia CIRP*, Vol. 17, pp. 824-829.

[Sato2005] Sato, A., Ishikawa, Y., Nowotny, S., and Scharek, S., "United States Patent: 7626136 - Powder Metal Cladding Nozzle," Jan 4, 2005.

[Schneider1968] Schneider, M., 1968, "Laser Cladding with Powder," *Ph. D. thesis*, University of Twente.

[Schwendner2001] Schwendner, K. I., Banerjee, R., Collins, P. C., Brice, C. A., and Fraser, H. L., 2001, "Direct Laser Deposition of Alloys from Elemental Powder Blends," *Scripta Materialia*, Vol. **45**(10), pp. 1123-1129.

[Sexton2002] Sexton, L., Lavin, S., Byrne, G., and Kennedy, A., 2002, "Laser Cladding of Aerospace Materials," Journal of Materials Processing Technology, Vol. **122**(1), pp. 63-68.

[Shah2008] Shah, K., Pinkerton, A., Moat, R., Li, L., and Preuss, M., 2008, "Direct Diode Laser Deposition of Functionally Graded Ti-6Al-4V and Inconel 718 Components," *Proceedings of the 3rd Pacific International Conference on Application of Lasers and Optics*, Beijing, China, April 2008.

[Shah2014] Shah, K., Haq, I., Khan, A., Shah, S.A., Khan, M., and Pinkerton, A.J., 2014, "Parametric Study of Development of Inconel-Steel Functionally Graded Materials by Laser Direct Metal Deposition," *Materials & Design*, Vol. **54**, pp. 531-538.

[Shankar2015] Shankar, P., Fazelpour, M., and Summers, J.D., 2015, "Comparative

Study of Optimization Techniques in Sizing Mesostructures for Use in NonPneumatic Tires," *Journal of Computing and Information Science in Engineering*, Vol. 15(4), pp. 041009(1-6).

[Shepeleva2000] Shepeleva, L., Medres, B., Kaplan, W.D., Bamberger, M., and Weisheit, A., 2000, "Laser Cladding of Turbine Blades," *Surface and Coatings Technology*, Vol. **125**(1-3), pp. 45-48.

[Shin2003] Shin, K., Natu, H., Dutta, D., 2003, "A Method for the Design and Fabrication of Heterogeneous Objects," Materials & Design, Vol. **24**(5) pp. 339-353.

[Shishkovsky2012] Shishkovsky, I., Missemer, F., and Smurov, I., 2012, "Direct Metal Deposition of Functional Graded Structures in Ti-Al System," *Physics Procedia*, Vol. **39**, pp. 382-391.

[Shuja2010] Shuja, S. Z., Yilbas, B. S., and Momin, O., 2010, "Laser Heating of Moving Solid: Influence of Workpiece Speed on Melt Size," AIChE Journal, Vol. 56(11), pp. 2997-3004.

[Silman2012] Silman, G.I., 2012, "Compilative Fe-Ni Phase Diagram with Author's Correction," *Material Science and Heat Treatment*, Vol. **54**(3-4), pp. 105-112.

[Siu2002] Siu, Y., and Tan, S., 2002, "Modeling the Material Grading and Structures of Heterogeneous Objects for Layered Manufacturing," *Computer-Aided Design*, Vol. **34**(10), pp. 705-716.

[Soodi2014] Soodi, M., and Masood, S.H., 2014, "Tensile Strength of Functionally Graded and Wafer Layered Structures Produced by Direct Metal Deposition," *Rapid Prototyping Journal*, Vol. **20**(5), pp. 360-368.

[Sun2004] Sun, S., Durandet, Y., and Brandt, M., 2004, "Parametric Investigation of Pulsed Nd:YAG Laser Cladding of Stellite 6 on Stainless Steel," *Surface & Coatings Technology*, Vol. **194**(2-3), pp. 225-231.

[Syed2006a] Syed, W.U.H., Pinkerton, A.J., and Li, L., 2006, "Simultaneous Wire- and Powder- Feed Direct Metal Deposition: an Investigation of the Process Characteristics and Comparison with Single-Feed Methods," Journal of Laser Applications, Vol. **18**(1), pp. 65-72.

[Syed2006b] Syed, W.U.H., Pinkerton, A.J., and Li, L., 2006, "Combining Wire and Coaxial Powder Feeding in Laser Direct Metal Deposition for Rapid Prototyping," *Applied Surface Science*, Vol. **252**(13), pp. 4803-4808.

[Tabernero2010] Tabernero, I., Lamikiz, A., Ukar, E., Lacalle, L. N., Angulo, C., and

Urbikain, G., 2010, "Numerical Simulation and Experimental Validation of Powder Flux Distribution in Coaxial Laser Cladding," *Journal of Materials Processing Technology*, Vol. **210**(15), pp. 2125-2134.

[Tabernero2012] Tabernero, I., Lamikiz, A., Martínez, S., Ukar, E., and Lacalle, L. N., 2012, "Modeling of Energy Attenuation due to Powder Flow – Laser Beam Interaction during Laser Cladding Process," *J. Mater. Process. Tech.*, Vol. **212**(2), pp. 516-522.

[Tabernero2013] Tabernero, I., Calleja, A., Lamikiz, A., and Lacalle, L. N. L. de, 2013, "Optimal Parameters for 5-Axis Laser Cladding," *Procedia Engineering*, Vol. **63**, pp. 45-52.

[Tan2011b] Tan, W., Bailey, N. S., and Shin, Y. C., 2011, "A Novel Integrated Model Combining Cellular Automata and Phase Field Methods for Microstructure Evolution during Solidification of Multi-Component and Multi-Phase Alloys," *Computational Materials Science*, Vol. **50**(9), pp. 2573-2585.

[Tan2011a] Tan, W., Wen, S., Bailey, N., and Shin, Y. C., 2011, "Multiscale Modeling of Transport Phenomena and Dendritic Growth in Laser Cladding Processes," *Metallurgical and Materials Transactions B*, Vol. **42B**(6), pp. 1306-1318.

[Tang2011] Tang, L., and Landers, R.G., 2011, "Layer-to-Layer Height Control for Laser Metal Deposition Process," 2011, *Journal of Manufacturing Science and Engineering*, Vol. **133**(2), pp. 021009(1-9).

[Thivillon2009] Thivillon, L., Bertrand, Ph. Laget, B., and Smurov, I., 2009, "Potential of Direct Metal Deposition Technology for Manufacturing Thick Functionally Graded Coatings and Parts for Reactors Components," *Journal of Nuclear Materials*, Vol. **385**(2), pp. 236-241.

[Tian1994] Tian, X., and Kennedy, F. E. Jr. 1994, "Maximum and Average Flash Temperatures in Sliding Contacts," *Journal of Tribology*, Vol. **116**(1), pp. 167-174.

[Toyserkani2003] Toyserkani E., 2003, "Modeling and Control of Laser Cladding by Powder Injection," *Ph.D. thesis*, University of Waterloo, Ontario, Canada.

[Toyserkani2004] Toyserkani, E., Khajepour, A., and Corbin, S., 2004, "3-D Finite Element Modeling of Laser Cladding by Powder Injection: Effects of Laser Pulse Shaping on the Process," *Optics and Lasers in Engineering*, Vol. **41**(6), pp. 849-867.

[Toyserkani2005] Toyserkani, E., "Laser Cladding," CRC Press LLC, 2005. Print.

[Traini2008] Traini, T., Mangano, C., Sammons, R.L., Mangano, F., Macchi, A., and

Piattelli, A., 2008, “Direct Laser Metal Sintering as a New Approach to Fabrication of an Isoelastic Functionally Graded Material for Manufacture of Dental Implants,” *Dental Materials,* Vol. **24**(11), pp. 1525-1533.

[Unocic2003] Unocic, R.R., and DuPont, J.N., 2003, “Composition Control in the Direct Laser-Deposition Process,” *Metallurgical and Materials Transactions B,* Vol. **34B**(4), pp. 439-445.

[Urbanic2016] Urbanic, R.J., Saqib, S.M., and Aggarwal, K., 2016, “Using Predictive Modeling and Classification Methods for Single and Overlapping Bead Laser Cladding to Understand Bead Geometry to Process Parameter Relationships,” *Journal of Manufacturing Science and Engineering*, Vol. **138**(5), pp. 051012(1-13).

[Valsecchi2012] Valsecchi, B., Previtali, B., and Gariboldi, E., 2012, “Fibre Laser Cladding of Turbine Blade Leading Edges: the Effect of Specific Energy on Clad Dilution,” *International Journal of Structural Integrity,* Vol. **3**(4), pp. 377-395.

[Vetter1993] Vetter, P. A., Fontaine, J., Engel, T., Lagrange, L., and Marchione, T., 1993, “Characterization of Laser-Material Interaction during Laser Cladding Process,” *Transactions on Engineering Sciences,* Vol. **2**, pp. 185-194.

[Wang2009] Wang, S., Chen, N., Chen, C., and Zhu, X., 2009, “Finite Element-Based Approach to Modeling Heterogeneous Objects,” *Finite Elements in Analysis and Design*, Vol. **45**(8-9), pp. 592-596.

[Watari2004] Watari, F., Yokoyama, A., Omori, M., Hirai, T., Kondo, H., Uo, M., and Kawasaki, T., 2004, “Biocompatibility of Materials and Development to Functionally Graded Implant for Bio-Medical Application,” *Composites Science and Technology,* Vol. **64**(6), pp. 893-908.

[Wells1952] Wells, A.A., 1952, “Heat Flow in Welding,” *Welding Journal,* Vol. **315**(5), pp. 263s-267s.

[Wen2009] Wen, S., Shin, Y., Murthy, J., and Sojka, P., 2009, “Modeling of Coaxial Powder Flow for the Laser Direct Deposition Process,” *International Journal of Heat and Mass Transfer,* Vol. **52**(25-26), pp. 5867-5877.

[Wen2010] Wen, S., and Shin, Y. C., 2010, “Modeling of Transport Phenomena during the Coaxial Laser Direct Deposition Process,” *Journal of Applied Physics,* Vol. **108**(4), pp. 044908(1-9).

[Wen2011] Wen, S., and Shin, Y. C., 2011, “Modeling of the Off-Axis High Power Diode Laser Cladding Process,” *Journal of Heat Transfer,* Vol. **133**(3), pp. 031007(1-10).

[Whitfield2008] Whitfield, R.P., "United State Patent: 8117985 B2 – Laser Cladding Device with an Improved Nozzle," Feb 21, 2008.

[Xing1998] Xing, A., Zhao, J., Huang, C., and Zhang, J., 1998, "Development of an Advanced Ceramic Tool Material-Functionally Gradient Cutting Ceramics," *Materials Science and Engineering*, Vol. **A248**(1-2), pp. 125-131.

[Xu2009] Xu, X., Lin, X., Yang, M., Chen, J., and Huang, W., 2009, "Microstructure Evolution in Laser Solid Forming of TI-50 wt% Ni Alloy," *Journal of Alloys and Compounds,* Vol. **480**(2), pp. 782-787.

[Yakovlev2005] Yakovlev, A., Trunova, E., Grevey, D., Pilloz, M., and Smurov, I., 2005, "Laser-Assisted Direct Manufacturing of Functionally Graded 3D Objects," *Surface and Coatings Technology*, Vol. **190**(1), pp. 15-24.

[Yan2014] Yan, J., Battiato, I., and Fadel, G. M., 2014, "Optimization of Multi-Materials In-Flight Melting in Laser Engineered Net Shaping (LENS) Process," *Proceedings of Symposium on Solid Freeform Fabrication*, University of Texas at Austin, Austin, Texas, August 2014.

[Yan2015] Yan, J., Masoudi, N., Battiato, I., and Fadel, G., 2015, "Optimization of Process Parameters in Laser Engineered Net Shaping (LENS) Deposition of Multi-Materials," *Proceedings of the ASME 2015 International Design Engineering technical Conferences & Computers and Information in Engineering Conference (IDETC/CIE)*, Boston, Massachusetts, August 2015.

[Yan2016] Yan, J., Battiato, I., and Fadel, G., 2016, "Design of Injection Nozzle in Direct Metal Deposition (DMD) Manufacturing of Thin-Walled Structures Based on 3D Models," *Proceedings of the ASME 2016 International Design Engineering technical Conferences & Computers and Information in Engineering Conference (IDETC/CIE)*, Charlotte, North Carolina, August 2016.

[Yang2000a] Yang, Z., Sista, S., Elmer, J. W., and Debroy, T., 2000, "Three Dimensional Monte Carlo Simulation of Grain Growth during GTA Welding of Titanium," *Acta Materialia*, Vol. **48**(20), pp. 4813-4825.

[Yang2000b] Yang, Z., Sista, S., Elmer, J.W., and Debroy, T., 2000, "Three Dimensional Monte Carlo Simulation of Grain Growth During GTA Welding of Titanium," *Acta Materialia*, Vol. **48**(20), pp. 4813-4825.

[Yang2000c] Yang, Z., 2000, "Modeling Weldment Macro and Microstructure from Fundamentals of Transport Phenomena and Phase Transformation Theory," *Ph.D. thesis*, the Pennsylvania State University.

[Yilbas2013] Yilbas, B. S., and Akhtar, S., 2013, “Laser Welding of AISI 316 Steel: Microstructural and Stress Analysis,” *Journal of Manufacturing Science and Engineering*, Vol. **135**(3), pp. 031018(1-10).

[Yin2010] Yin, H., and Felicelli, S. D., 2010, “Dendrite Growth Simulation during Solidification in the LENS Process,” *Acta Materialia*, Vol. **58**(4), pp. 1455-1465.

[Yue2008] Yue, T.M., and Li, T., 2008, “Laser Cladding of Ni/Cu/Al functionally graded coating on magnesium substrate,” *Surface and Coatings Technology*, Vol. **202**(23), pp. 3043-3049.

[Zekovic2007] Zekovic, S., Dwivedi, R., and Kovacevic, R., 2007, “Numerical Simulation and Experimental Investigation of Gas-Powder Flow from Radially Symmetrical Nozzles in Laser-Based Direct Metal Deposition,” *International Journal of Machine Tools & Manufacture*, Vol. **47**(1), pp. 112-123.

[Zhan2009] Zhan, X., Dong, Z., Wei, Y., and Ma, R., 2009, “Simulation of Grain Morphologies and Competitive Growth in Weld Pool of Ni-Cr Alloy,” *Journal of Crystal Growth*, Vol. **311**(23-24), pp. 4778-4783.

[Zhang2006] Zhang, H., Kong, F., Wang, G., and Zeng, L., 2006, “Numerical Simulation of Multiphase Transient Field during Plasma Deposition Manufacturing,” *Journal of Applied Physics*, Vol. **100**(12), pp. 123522(1-9).

[Zhang2008] Zhang, Y., Wei, Z., Shi, L., and Xi, M., 2008, “Characterization of Laser Powder Deposited Ti-TiC Composites and Functional Gradient Materials,” *Journal of Materials Processing Technology*, Vol. **206**(1-3), pp. 438-444.

[Zhang2009] Zhang, W., Liu, L., Zhao, X., Huang, T., Yu, Z., Qu, M., and Fu, H., 2009, “Effect of Cooling Rates on Dendrite Spacing of Directionally Solidified DZ215 Alloy under High Thermal Gradient,” *Rare Metals*, Vol. **28**(6), pp. 633-638.

[Zhao2009] Zhao, X., Lin, X., Chen, J., Xue, L., and Huang, W., 2009, “The Effect of Hot Isostatic Pressing on Crack Healing, Microstructure, Mechanical Properties of Rene88DT Superalloy Prepared by Laser Solid Forming,” *Materials Science and Engineering A.*, Vol. **504**(1-2), pp. 129-134.

[Zhong2006] Zhong, M., Liu, W., Zhang, Y., and Zhu, X., 2006, “Formation of WC/Ni Hard Alloy Coating by Laser Cladding of W/C/Ni Pure Element Powder Blend,” *International Journal of Refractory Metals and Hard Materials*, Vol. **24**(6), pp. 453-460.

[Zhou2009] Zhou, J., and Liu, H., “Laser Rapid Manufacturing Technology and Application,” Beijing: Chemical Industry Press, 2009. Print.

[Zhou2011] Zhou, S., Dai, X., and Zheng, H., 2011, "Analytical Modeling and Experimental Investigation of Laser Induction Hybrid Rapid Cladding for Ni-Based WC Composite Coatings," *Optics & Laser Technology*, Vol. **43**(3), pp. 613-621.

[Zhu2011] Zhu, G., Li, D., Zhang, A., and Tang, Y., 2011, "Numerical Simulation of Metallic Powder Flow in a Coaxial Nozzle in Laser Direct Metal Deposition," *Optics and Laser Technology*, Vol. **43**(1), pp. 106-113.